HARNESSING THE POWER OF -OMICS TO UNCOVER NOVEL TARGETS OF INVESTIGATION IN MITOCHONDRIAL DISORDERS

by
Arianna Lee Franca Anzmann

A dissertation submitted to Johns Hopkins University in conformity with the requirements for the degree of Doctor of Philosophy

Baltimore, Maryland
May 2021

Abstract

Methylmalonic acidemia (MMA), propionic acidemia (PA), and Barth syndrome (BTHS) are three inborn errors of intermediary mitochondrial metabolism where the primary metabolic defects are well defined, but there is limited knowledge of the downstream cellular effects thus limiting development of novel therapeutics. Using hypothesis-generating untargeted proteomics and metabolomics in cellular models of these disorders, we identified and functionally confirmed novel areas of cellular pathogenicity.

In patient and CRISPR/Cas9-edited cells modeling MMA and PA, we demonstrated increased abundance of proteins and metabolites involved in serine synthesis and thiol metabolism. We functionally confirmed these findings with flux metabolomics and identified an increase in *de novo* serine biosynthesis, serine transport, and abnormal downstream tricarboxylic acid (TCA) cycle utilization. Together, we identified serine metabolism as a novel target of cellular pathogenesis in MMA and PA, and a potential new target for therapeutic investigation.

In patient and CRISPR/Cas9-edited cells that we validated as a new model of BTHS, we identified abnormal regulation of proteins associated with two distinct pathways: mitochondrial respiratory chain complex I (CI), mitochondrial quality control. We confirmed reduced expression, abundance, and activity of CI, as well as increased abundance and activity of PARL, a rhomboid protein involved in the regulation of mitophagy and apoptosis. By modulating cardiolipin (CL), the phospholipid affected in BTHS, via phospholipase inhibitor bromoenol lactone and the CL targeted SS-peptide, SS-

31, we showed that each is able to remediate abnormalities in CI abundance as well as PARL activity. Together, we further delineated a previously described pathway, mitochondrial respiratory chain CI, and identified a novel pathway for further investigation, mitochondrial quality control.

We conclude that untargeted studies harnessing the power of -omics has the ability to uncover novel pathways of investigation in IEMs providing alternative targets for therapeutic interventions.

Primary Reader and Advisor: Hilary J. Vernon

Secondary Reader: Steven M. Claypool

Acknowledgements

To my mentor and thesis advisor, Hilary Vernon, thank you, from the bottom of my heart, for your endless support over these past 6 years. When I joined the program, I knew I wanted to join your lab, not only because I found your research fascinating, but because I just had a feeling you were going to be the perfect mentor for me, and you did not disappoint. You gave me the independence and confidence to grow as a responsible scientist and always had a smile and words of encouragement when I needed it most. I am truly honored to be your first doctoral student, and look forward to keeping in touch as you continue to grow the Vernon Lab.

To my bonus mentor, Steve Claypool, thank you for perfectly balancing the line between being my harshest critic and most ardent supporter. I don't always know when you are being sarcastic, but I do know I am a better scientist because of you.

To the Human Genetics program, thank you for taking a chance on me and providing the supportive environment to train, learn, and grow. This work would not be possible without Dr. Valle and Sandy Muscelli. Sandy, your door was always open, whether I needed candy, advice, or just a friendly chat. Don't even doubt your value to the program.

To Professor Moore, your passion for science, and specifically genetics, ignited a fire in me that would be fueled by mentors yet to come, and I thank you. To Professor Blair, your genetics course was the first of many, but it was your high expectations and attention to detail that really pushed me to become a better student and scientist, and I

thank you. To Roger Reeves, I will always remember the time your taught me to dissect a mouse brain, as it highlights the patience and support you have continued to provide me throughout my career, and I thank you. To Garry Cutting, my time in your lab cemented my desire to pursue a career in genetics, and I thank you.

To all my friends in and out of Hopkins, thank you for always being the necessary distraction I needed. Karen, Laura, Jeenah, Briana, Melissa, Kristin, Sarah, Alyssa, Olivia, Cassandra, Marah, Kyra, Ally, Nikki, Heather, Kyle, Kent, Andrew, Will, Laura, you are all amazing people.

Thank you to my family, I would not be where I am today were it not for your support and sacrifices. Mark, Vicki, Trevor, thank you for welcoming me into your family. To my parents, Mom, Tom and Dad, thank you for never pushing me and letting me find my own path.

And finally, thank you to my husband, Tyler. For the past 14 years you have been by my side and I am forever grateful for your unwavering love and support. You're my lobster.

Dedication

"And to all the little girls watching right now, never doubt that you are valuable and powerful and deserving of every chance and opportunity in the world."

-Hillary Clinton, 2016

Contents

Abstract ii

Acknowledgements iii

List of Tables vi

List of Figures vii

1 Introduction 1

1.1 Inborn errors of metabolism 1

1.1.1 Methylmalonic acidemia 3

1.1.2 Propionic acidemia 5

1.1.3 References 6

1.2 Mitochondrial dysfunction and Barth syndrome. 7

1.2.1 Abstract. 7

1.2.2 Barth Syndrome. 8

1.2.3 Tafazzin. 10

1.2.4 Cardiolipin. 12

1.2.5 Barth Syndrome Models. 27

1.2.6 Barth Syndrome Therapies. 31

1.2.7 Conclusion. 34

1.2.8 References. 34

1.3 Identifying novel pathways of interest in inborn errors of metabolism . . 41

1.3.1 References. 43

2 Multi-omics studies in cellular models of methylmalonic acidemia and propionic acidemia reveal dysregulation of serine metabolism 44

2.1 Abstract. 44

2.2 Introduction. 45

2.3 Methods. 47

2.4 Results. 57
2.5 Discussion. 68
2.6 References. 72
2.7 Supplementary Information. 76

3 Barth syndrome cellular models have dysregulated respiratory complex I and mitochondrial quality control due to abnormal cardiolipin 83

3.1 Abstract. 83
3.2 Introduction. 84
3.3 Methods. 86
3.4 Results. 95
3.5 Discussion. 111
3.6 Conclusions. 114
3.7 Acknowledgements. 115
3.8 Conflict of Interest. 115
3.9 References. 116
3.10 Supplementary Information. 119

4 Conclusions 149

4.1 Future Directions. 152
4.2 References. 153

5 Curriculum Vitae 154

List of Tables

Chapter 1

Table 1. Barth Syndrome model systems. 29

Chapter 2

Supplemental Table 1. sgRNA sequences for *MUT and PCCA* 78
Supplemental Table 2. Primer sequences for Surveyor Assay screening and sequencing of edited clones 78
Supplemental Table 3. qRT-PCR Primer sequences for mRNA expression in HEK293 cells 78
Supplemental Table 4A. Significantly enriched GO terms and KEGG pathways identified by DAVID analysis of proteins with reduced abundance in fibroblast cells from individuals with methylmalonic acidemia (MMA) 79
Supplemental Table 4B. Significantly enriched GO terms and KEGG pathways identified by DAVID analysis of proteins with increased abundance in fibroblast cells from individuals with methylmalonic acidemia (MMA) 80
Supplemental Table 4C. Significantly enriched GO terms and KEGG pathways identified by DAVID analysis of proteins with reduced abundance in fibroblast cells from individuals with propionic acidemia (PA) 80
Supplemental Table 4D. Significantly enriched GO terms and KEGG pathways identified by DAVID analysis of proteins with increased abundance in fibroblast cells from individuals with propionic acidemia (PA) 82

Chapter 3

Table S1. CRISPR/Cas9 sgRNA guide sequences and predicted off-target sites. 121
Table S2A. Significant KEGG & GO terms determined by functional annotation analysis of the proteins with a FC ≤ 0.80 (n=215) 122

Table S2B. Significant KEGG & GO terms determined by functional annotation analysis of the proteins with a FC ≥ 1.20 (n=621) 125
Table S3. Proteomics quantification of all complex I (CI) associated proteins 130
Table S4. Abundance of PARL with CCCP treatment (20uM) at serial time points (Figure 3E) 139
Table S5. Percent of PGAM5 cleavage with CCCP treatment (20uM) at serial time points (Figure 3D) 140
Table S6. Relative abundance of NDUFAF1 and relevant statistics of HEK293 WT and *TAZ*$^{\Delta 45}$ cells treated with BEL and SS-31 (Figure 4A). 141
Table S7. Relative mRNA expression and relevant statistics of HEK293 WT and *TAZ*$^{\Delta 45}$ cells treated with BEL and SS-31. 142
Table S8. CI holoenzyme abundance and relevant statistics of HEK293 WT and *TAZ*$^{\Delta 45}$ cells treated with BEL and SS-31. 144
Table S9. Percentage of cleaved PGAM5 and relevant statistics of HEK293 WT and *TAZ*$^{\Delta 45}$ cells treated with BEL and SS-31 (Figure 4D) 145
Table S10. Relative abundance of cleaved PARL and relevant statistics of HEK293 WT and *TAZ*$^{\Delta 45}$ cells treated with BEL and SS-31 (Figure 4E) 146
Table S11. Cell lines. 147
Table S12. Primers used for qRT-PCR. 148

List of Figures

Chapter 1

Figure 1. Barth syndrome. 9
Figure 2. Cardiolipin biosynthesis and remodeling. 14
Figure 3. Biological roles of cardiolipin. 21
Figure 4. Barth syndrome therapeutic strategies. 32

Chapter 2

Figure 1. Workflow for proteomics analysis. 58
Figure 2. OPLS-DA score plots show clustering of cohorts. 60
Figure 3. Metabolites with increased abundance in propionic acidemia (PA) and methylmalonic acidemia (MMA) plasma samples. 61
Figure 4. Generation of MUT-null and PCCA-null HEK293 cells. 62
Figure. 5. Metabolites in spent media from in *PCCA*$^{E12\Delta13}$, *MUT*$^{E5\Delta22}$ cells and WT cells. 63
Figure 6. mRNA expression in *PCCA*$^{E12\Delta13}$ and *MUT*$^{E5\Delta22}$ cells at 4 and 8 days of growth. 65
Figure 7. Serine biosynthesis and transport in *MUT*$^{E5\Delta22}$ and *PCCA*$^{E12\Delta13}$ cells 66
Figure 8. ^{13}C-labeled TCA intermediates *MUT*$^{E5\Delta22}$ and *PCCA*$^{E12\Delta13}$ cells. 67
Supplemental Figure 1. Histogram of the protein expression fold change across 3,449 proteins measured via shotgun proteomics in (A) Propionic acidemia fibroblasts compared to controls (PA) and (B) Methylmalonic acidemia (MMA) fibroblasts compared to controls. 76
Supplementary Figure 2. mRNA expression in *PCCA*$^{E12\Delta13}$ and *MUT*$^{E5\Delta22}$ cells at 1, 2, 4 and 8 days of growth. 77

Chapter 3

Figure 1. *TAZ*$^{\Delta 45}$ HEK293 genetic characterization, CL profiling and proteomics analysis. 97

Figure 2. Reduced complex I (CI) holoenzyme abundance and activity in HEK293 *TAZ*$^{\Delta 45}$ cells and BTHS patient-derived lymphoblastoid cells. 101

Figure 3. Increased cleavage of PGAM5 by PARL in HEK293*TAZ*$^{\Delta 45}$ cells. 106

Figure 4. Targeting CL or CL metabolism with bromoenol lactone and SS-31 modifies mitochondrial dysfunction. 110

Figure S1. CRISPR/Cas9 genome editing with two single guide RNAs (sgRNAs) targeting exon 2 of *TAZ* results in a 45 bp deletion. 119

Figure S2. Comparable abundance of cytosolic and mitochondrial proteins in the absence of TAZ. 120

Figure S3. The oxidative phosphorylation (OXPHOS) KEGG pathway is the most significant KEGG pathway enriched for proteins with a FC ≤ 0.80 that references mitochondria and or OXPHOS. 129

Figure S4. Relative mRNA expression of complex I (CI) subunits. 132

Figure S5. Relative mRNA expression of complex I (CI) subunits varies across different LCL lines. 133

Figure S6. Immunoblotting of isolated mitochondria for CI and CIII subunits. 134

Figure S7. Difference in complex II (CII) activity between and within cell types. 135

Figure S8. Overexpression of CI assembly factor NDUFAF1 does not normalize CI activity. 136

Figure S9. Validation and classification of PARL antibodies. 137

Figure S10. PARL abundance and activity in control and BTHS LCL lines. 138

Figure S11. Relative mRNA expression of (A) *NDUFB2* (B) *NDUFAB1* (C) *NDUFB4* and (D) *NDUFB6* after treatment with BEL and SS-31. 143

Chapter 1

Introduction

1.1 Inborn errors of metabolism

In 1902, Sir Archibald Edward Garrod described alkaptonuria, a condition with urine that has “the power of staining fabrics deeply”, or more simply, black urine, in an article titled “The Incidence of Alkpatonuria: A Study in Chemical Individuality”. [1] At that point, alkaptonuria was not thought to be a disorder but an alternative, slightly less efficient pathway in metabolism. However, Garrod’s observations, especially the observation of the high incidence of alkaptonuria in children of first cousins, led him to later coin the term “inborn errors of metabolism”. [2] In 1908, during the Croonian Lectures delivered by Garrod before the Royal College of Physicians of London, Garrod hypothesized that four metabolic disorders, alkaptonuria, pentosuira, cystinuria, and albinism, were congenital and inborn reflecting Mendelian inheritance. [2] In 1909, the Croonian Lectures were published as the first edition of Inborn Errors of Metabolism. [3] Fourteen years later in 1923, the second edition was published with two additional inborn disorders, and now in 2021, over 100 years since the first edition, its modern successor “The Online Metabolic & Molecular Bases of Inherited Disease” (OMMBID) describes over 500 inborn errors of metabolism. [4, 5]

Inborn errors of metabolism (IEM) are a heterogenous group of disorders in which a single gene defect results in the absence or abnormality of an enzyme or its cofactor. IEMs can be classified in many ways, but three major categories include small molecule disorders, disorders of energy deficiency, and complex molecule disorders. [6–8] Small molecule disorders result in intoxication from the accumulation of compounds proximal to the metabolic block, such as in methylmalonic acidemia (MMA, MIM#251000) and propionic acidemia (PA, MIM#606054). [6, 7] Disorders of energy deficiency are due to deficiencies in energy production or use, such as in Leber hereditary optic neuropathy (LHON, MIM# 308905). Lastly, complex molecular disorders encompass disorders that affect the synthesis, processing, quality control, and catabolism of complex molecules, such as in Barth syndrome (BTHS, MIM#302060).

Individually, IEMs are rare, however, as a group IEMs are estimated to occur 1 out of 2,500 live births. [7] Clinically, IEMs will present either in one functional system or organ, or systemically affecting multiple processes and organs. [9] Presenting symptoms are diverse and can include; developmental delay, seizures, intoxication, hypogylcemia, lactic acidemia, hypotonia, myopathy, cardiomyopathy, failure to thrive, cardiac failure, circulatory collapse, sudden infant death syndrome, and congenital malformations. [6, 9]

Treatment approaches for the IEMs include restoration of the biochemical imbalance between substrate and product due to a metabolic defect. This can be achieved through dietary restriction, substrate reduction therapy, and toxin removal. [10] Alternatively, enzyme replacement therapy, gene therapy, cell/organ transplantation, cofactor supplementation, and chaperone therapy are all treatments that aim to replace or enhance the absent or dysfunctional enzyme or cofactor. [10]

From four disorders to hundreds, the breadth and scope of the diagnosis and treatment of IEMs has exponentially expanded since Garrod first coined the term over a 100 years ago. Unfortunately, even with the vast expansion of knowledge, IEMs result in substantial mortality or long-term morbidity, representing 0.4% of all child deaths worldwide. [11] Continued research of IEMs will improve diagnosis, monitoring, and treatment, as well as ultimately reducing the global burden of IEMs.

1.1.1 Methylmalonic acidemia

Methylmalonic acidemia (MMA, MIM#251000) is a rare autosomal recessive IEM caused by pathogenic variants in the gene methylmalonyl-CoA mutase (*MMUT*, type: *mut*-MMA) or the biosynthesis of its vitamin B12 cofactor. [12–14] *MMUT* encodes a mitochondrial enzyme, MUT, that catalyzes the isomerization of L-methylmalonyl-CoA to succinyl-CoA, a key step in propionate metabolism that funnels metabolites from the breakdown of propionic acid, amino acids, odd-chain fatty acids, and cholesterol esters, into the tricarboxylic acid cycle (TCA cycle). [12–14] MUT deficiencies are subdivided into two subgroups, mut^{o}, with no MUT activity, and mut^{-}, with low to moderate MUT activity in the presence of high concentrations of adenosylcobalamin (AdoCbl). [12, 13]

MUT requires the adenosylcobalamin (AdoCbl) form of vitamin B_{12} for enzymatic function. As such, MMA can also be caused by deficiency of proteins involved in the generation of AdoCbl; methylmalonic aciduria type A protein (MMAA, type: *clbA*-MMA), methylmalonic aciduria type B protein (MMAB, type: *cblB*-MMA), or the methylmalonic aciduria and homocystinuria type D protein (MMADHC, type: *cblD*-MMA). [12] MMA can also be cause by the deficiency of methylmalonyl-CoA epimerase (MCE) an enzyme

that converts D-methylmalonyl-CoA epimer to L-methylmalonyl-CoA epimer, which is the substrate of MUT, though this form is very rare with less than 10 cases described in the literature. [12, 14] Overall, approximately 97% of MMA cases are caused by pathogenic variants in the genes *MMUT* (type: *mut*-MMA), *MMAA* (type: *clbA*-MMA), *MMAB* (type: *cblB*-MMA). [14]

Due to the metabolic block, MMA is biochemically characterized and diagnosed by high levels of methylmalonic acid and propionylcarnitine in the blood and urine. [12] Normal mitochondrial function requires sufficient energy production through the TCA cycle and oxidative phosphorylation, therefore, MMA results in systemic chronic disease, particularly in organs with high energy needs such as the brain, heart, kidney, and eye. [15] Early-onset symptoms, which can present in the first days of life, may include lethargy, vomiting, hypotonia, hypothermia, respiratory distress, severe ketoacidosis, hyperammonemia, neutropenia, and thrombocytopenia. [12, 15, 16] In older infants and children, symptoms may include failure to thrive, kidney disease, hypotonia, developmental delay, and other acute and chronic neurologic symptoms. [12, 15, 16] Irreversible organ injury may eventually occur due to the accumulation of abnormal metabolites caused by MUT deficiency. [15] Treatment includes acute stabilization of symptoms at onset and during period of metabolic crisis, supplementation of vitamin B_{12} in those cases that are vitamin responsive, and lifelong management with dietary protein restriction and carnitine supplementation.

Despite aggressive management, patients with MMA typically experience severe morbidity and mortality. [15–19]

1.1.2 Propionic acidemia

Propionic acidemia (PA, MIM#606054) is a rare autosomal recessive IEM caused by pathogenic variants in the genes encoding the mitochondrial enzyme propionyl-CoA carboxylase (PCC), *PCCA* or *PCCB*. [20, 21] PCC catalyzes the carboxylation of propionyl-CoA to D-methylmalonyl-CoA, another key step in propionate metabolism, and the metabolic step upstream of MUT. [20, 21]

PA is biochemically diagnosed by elevated propionylcarnitine in the blood and urine, and elevated methylcitrate (a byproduct of abnormal TCA metabolism) in the urine. [15, 16, 20] There is significant clinical overlap between MMA and PA, where PA also results in systemic chronic disease, particularly in organs with high energetic needs. [15] Early-onset symptoms include poor feeding, vomiting, progressive encephalopathy, lethargy, seizures, and coma. [15, 16, 20] Most individuals with PA become symptomatic with the first weeks of life, however, residual PCC function may delay the onset of symptoms to beyond the neonatal period. [20] Later-onset symptoms, that may occur due to a metabolic crisis, may include protein intolerance, failure to thrive, hypotonia, developmental regression, progressive encephalopathy, lethargy, seizures, and coma. [15, 16, 20] In contrast to MMA, kidney disease is less severe and occurs later in the course of the disease, and in PA cardiomyopathy may be more severe and present at a younger age compared to MMA. [15]

The treatment and management of PA is very similar to the treatment and management of MMA with the acute stabilization of presenting symptoms and lifelong management with dietary protein restriction and carnitine supplementation. [15, 16]

Patients with PA experience severe morbidity and mortality, with long term outcomes dependent on the age of onset, age of diagnosis, severity of disease, and treatment.

1.1.3 References

1. A. E. Garrod, The incidence of alkaptonuria. A study in chemical individuality. Lancet 160, 1617–1620 (1902).
2. A. E. Garrod, The Croonian Lectures on Inborn Errors of Metabolism. Delivered before the Royal College of Physicians of London on June 18th, 23rd, 25th, and 30th, 1908. Lancet 172, 1–7 (1908).
3. A. E. Garrod, Inborn Errors of Metabolism (Oxford University Press, 1909).
4. A. E. Garrod, Inborn Errors of Metabolism (Henry Frowde, Hodder and Stoughton, 1923).
5. C. R. Scriver, Garrod's croonian lectures (1908) and the charter "inborn errors of metabolism": Albinism, alkaptonuria, cystinuria, and pentosuria at age 100 in 2008. J. Inherit. Metab. Dis. 31, 580–598 (2008).
6. J. M. Saudubray, À. Garcia-Cazorla, Inborn Errors of Metabolism Overview: Pathophysiology, Manifestations, Evaluation, and Management. Pediatr. Clin. North Am. 65, 179–208 (2018).
7. C. R. Ferreira, C. D. M. van Karnebeek, "Inborn errors of metabolism" in Handbook of Clinical Neurology, (2019), pp. 449–481.
8. G. L. Arnold, Inborn errors of metabolism in the 21st century: past to present. Ann. Transl. Med. 6, 467 (2018).
9. J. M. Saudubray, C. Charpentier, "Clinical Phenotypes: Diagnosis/Algorithms." in The Online Metabolic and Molecular Bases of Inherited Disease., D. Valle, S. Antonarakis, A. Ballabio, A. Beaudet, G. Mitchell, Eds. (McGraw-Hill, 2021).
10. M. J. Gambello, H. Li, Current strategies for the treatment of inborn errors of metabolism. J. Genet. Genomics 45, 61–70 (2018).
11. D. Waters, et al., Global birth prevalence and mortality from inborn errors of metabolism: A systematic analysis of the evidence. J. Glob. Health 8, 021102 (2018).
12. I. Manoli, J. L. Sloan, C. P. Venditti, "Isolated Methylmalonic Acidemia" in GeneReviews®[Internet], 1993rd–2020th Ed., M. P. Adam, H. H. Ardinger, R. A. Pagon, S. E. Wallace, Eds. (University of Washington, 2005).
13. P. Forny, et al., Molecular Genetic Characterization of 151 Mut-Type Methylmalonic Aciduria Patients and Identification of 41 Novel Mutations in MUT. Hum. Mutat. 37, 745–754 (2016).
14. C. Zhang, et al., Mutation analysis, treatment and prenatal diagnosis of Chinese cases of methylmalonic acidemia. Sci. Rep. 10 (2020).
15. J. L. Fraser, C. P. Venditti, Methylmalonic and propionic acidemias: Clinical management update. Curr. Opin. Pediatr. 28, 682–693 (2016).
16. M. R. Baumgartner, et al., Proposed guidelines for the diagnosis and management of methylmalonic and propionic acidemia. Orphanet J. Rare Dis. 9 (2014).
17. M. A. Cosson, et al., Long-term outcome in methylmalonic aciduria: A series of 30 French patients. Mol. Genet. Metab. 97, 172–178 (2009).
18. R. Zhou, A. S. Yazdi, P. Menu, J. Tschopp, A role for mitochondria in NLRP3 inflammasome activation. Nature 469, 221–226 (2011).
19. F. Hörster, et al., Long-term outcome in methylmalonic acidurias is influenced by the underlying defect (mut0, mut-, cblA, cblB). Pediatr. Res. 62, 225–230 (2007).
20. O. A. Shchelochkov, N. Carrillo, C. P. Venditti, "Propionic Acidemia" in GeneReviews®[Internet], 1993rd–2020th Ed., M. P. Adam, H. H. Ardinger, R. A. Pagon, S. E. Wallace, Eds. (University of Washington, 2012).

21. J. P. Kraus, et al., Mutation analysis in 54 propionic acidemia patients. J. Inherit. Metab. Dis. 35, 51–63 (2012).

1.2 Mitochondrial dysfunction and Barth syndrome

This original article has been published and was reprinted with permission: Anzmann AF, Claypool SM, Vernon H (2019) Mitochondrial dysfunction and Barth Syndrome. *Handbook of Mitochondrial Dysfunction.* S. I. Ahmad, Ed. (CRC Press/Taylor & Francis Group, 2019), pp. 61–77

1.2.1 Abstract

Barth syndrome (BTHS) is an X-linked inborn error of mitochondrial phospholipid metabolism, caused by pathogenic variants in the gene *tafazzin* (*TAZ*). *TAZ* encodes for a transacylase involved in the final remodeling step of cardiolipin (CL). The four acyl chains of CL allow for an array of CL species, however the determinants of the acyl chain composition of remodeled CL are still under debate. CL, localized to the inner mitochondrial membrane, has key roles in mitochondrial function including in cristae formation, organization of the mitochondrial respiratory chain, apoptosis, and mitophagy, among many others. As is typical of most primary mitochondrial diseases, BTHS is a multi-system disorder and is characterized by cardiomyopathy, skeletal myopathy, and neutropenia. Though the primary biochemical defect in BTHS has been known for several decades, there are no disease specific treatments, and the burden of morbidity and mortality in affected individuals is high. Treatment strategies under investigation include: lipid replacement, enzyme replacement, gene replacement, and drug therapy. This review summarizes Barth syndrome, with a focus on CL and its essential role in mitochondria.

1.2.2 Barth Syndrome

In 1980, Barth et al. described a novel X-linked mitochondrial disease affecting cardiac muscle, skeletal muscle and neutrophil leukocytes, at a Neuromuscular Disease Symposium held at Erasmus University.[1] Three years after this preliminary communication, Barth et al. reported a large Dutch family with cardiomyopathy, skeletal myopathy, neutropenia, and high infant mortality due to infection or cardiac failure.[2] These clinical characteristics have since become the cardinal features of what is now known as Barth syndrome (BTHS, MIM#302060) (Figure 1).[3–6] The incidence of BTHS is estimated to be about 1/300,000-400,000 live births, with fewer than 500 individuals worldwide included in the BTHS Registry & Repository. There is no known racial or ethnic predilection. [7,8]

The majority of individuals with BTHS present with cardiomyopathy within their first two years of life. [7] Classically, the cardiomyopathy presents as dilated cardiomyopathy with a component of left ventricular noncompaction, however hypertrophic cardiomyopathy has also been described. Heart function in BTHS patients can follow a waxing and waning pattern, sometimes with a period of relative stability after the toddler years and before puberty. [4] Cardiac arrhythmia and Long QT syndrome have also been described in a number of affected individuals. [9]

Skeletal myopathy and skeletal muscle fatigue are also important clinical features of BTHS. Affected individuals have decreased exercise endurance, weakness of proximal leg muscles, and overall lower activity levels. The skeletal muscle weakness and fatigue is independent of the cardiac dysfunction. [10]

Neutropenia is also seen in most affected individuals and can present as severe chronic neutropenia, cyclic neutropenia, or intermittent/non-cyclical neutropenia. Low neutrophil counts put affected individuals at risk for severe bacterial infections, ranging from mouth ulcers and gingival inflammation, to sepsis and multi-organ system failure. [7,11]

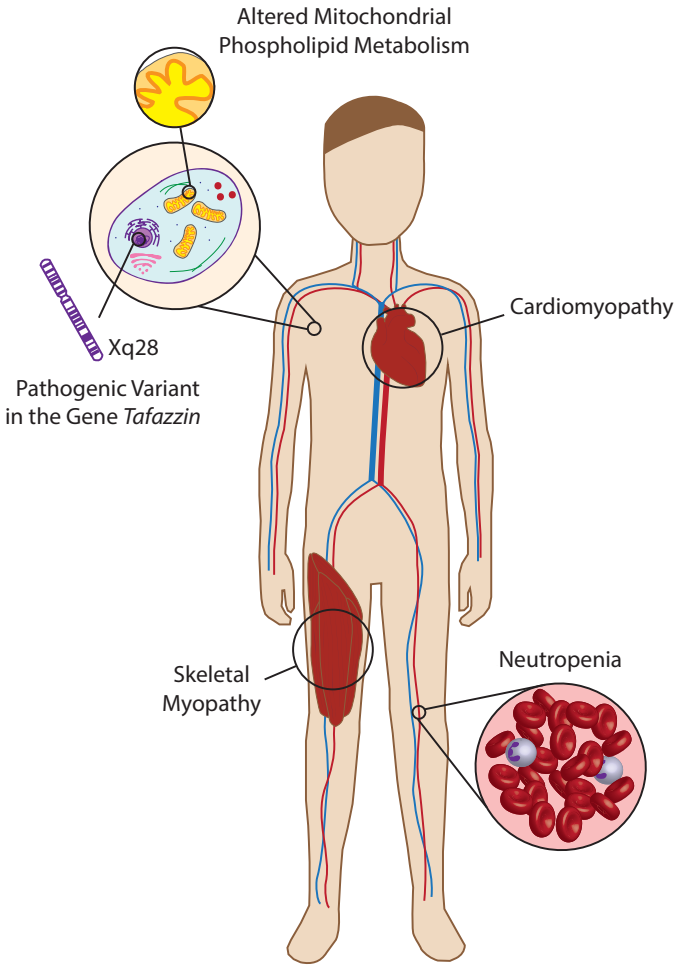

Figure 1. Barth syndrome. Barth syndrome (BTHS) is an inborn error of mitochondrial phospholipid metabolism, caused by pathogenic variants in the gene *tafazzin* (TAZ) located in the gene rich region of distal Xq28. *TAZ* encodes for a transacylase involved in the final remodeling step of cardiolipin (CL), which is essential for CL maturation. TAZ deficiency results in altered CL metabolism, with an increased monolyso-CL:CL and an abnormal acyl chain pattern in the remaining CL. Clinically, BTHS is characterized by cardiomyopathy, skeletal myopathy, and neutropenia.

Other clinical features seen in association with BTHS include failure to thrive, pre-pubertal growth delay, gastrointestinal complaints, hypoglycemia, and scoliosis.[4,7,12] There is no specific therapy for BTHS, and treatments are directed towards individual symptoms, including granulocyte-colony stimulating factor (G-CSF) therapy for neutropenia and medical treatment for cardiac failure. In cases of intractable heart failure, cardiac transplantation is performed. [5,13]

1.2.3 Tafazzin

In 1991, almost ten years after BTHS was first described, and ten years before the Human Genome Project was completed, Bolhuis et al. analyzed the linkage between the disease locus of BTHS and X-chromosomal markers.[14] Multipoint linkage analysis of the first BTHS family reported by Barth et al., a multi-generational family with seven carriers, four patients, and eight unaffected sons of carriers, mapped the disease locus to the gene rich Xq28 region.[14] Mapping to the distal Xq28 region was further confirmed in 1993 and 1995 by Ades et al. and Gedeon et al., respectively.[3,15] Then in 1996, Bione et al. reported the identification of the gene, termed *G4.5*, as responsible for BTHS.[16] The open reading frame of *G4.5* suggested several putative proteins ranging from 129 to 229 amino acids in length. Since these putative proteins did not have any homology to any previously identified nucleotide or protein sequence in GenBank at that time, they proposed that the novel proteins be named “tafazzins”.[16] This unique name pays homage to a comic from an Italian sports television show, Tafazzi, who repeatedly hits himself with an empty plastic bottle. 22 years later, the tafazzin gene/protein (*TAZ*/TAZ) maintains its reputation as a difficult subject for masochistic scientists.

TAZ is conserved form yeast to humans and has 11 exons with multiple alternative splicing isoforms. [17,18] Of the identified isoforms there are four major isoforms; the full length transcript (NM_000116), a transcript without exon 5 (Δ5, NM_181311), a transcript without exon 7 (Δ7, NM_181312), and a transcript without both exon 5 and 7 (Δ5Δ7, NM_181313). 17 Of the four isoforms, the mRNA isoform Δ5 is the predominant isoform, followed by Δ5Δ7, full-length, and Δ7. [17,19] Gene expression studies in patient lymphoblast lines and a TAZ deficient yeast model indicate that of the different isoforms, only two, the Δ5 and full-length isoforms, encode functional TAZ with transacylase (CL remodeling) activity.[17,20–22] Further, only a single polypeptide that co-migrates with the Δ5 isoform is expressed in human skin fibroblasts, Human embryonic kidney 293 (HEK293) cells, and murine heart and liver mitochondria.[23] It is interesting to note that the inclusion of exon 5 arose in the hominoid primate lineage after it branched from the Old World monkey lineage, 15-20 million years ago, due to a variant in the splice acceptor consensus sequence (GG>AG).17 This primate-specific exon is predicted to correspond to an intrinsically unstructured region of TAZ and has been speculated to contribute to primate-specific molecular interactions. [24]

As mentioned, when *TAZ* was first identified it had no sequence homology with any known nucleotide sequence. To date, the closest related protein with a known 3D structure is plant glycerol 3-phosphate acyltransferase (G3PAT), which has 20% sequence identity to human *TAZ*. [24] The mystery of TAZ function was cracked in 1997 when Neuwald reported, based on an alignment of human TAZ with two hypothetical proteins from yeast and worm, that TAZ belongs to a superfamily of acyltransferases with predicted roles in phospholipid biosynthesis.[25] Neuwald further suggested that the mitochondrial

dysfunction associated with BTHS may be due to alterations in the mitochondrial membrane phospholipids a prediction that was confirmed by Vreken et al. in 2000.[26] Indeed, TAZ is a ubiquitously expressed gene that encodes for a transacylase involved in the final remodeling step of cardiolipin (CL), a major phospholipid of the inner mitochondrial membrane (IMM).[27]

1.2.4 Cardiolipin

Mitochondria are unique organelles with two specialized membranes defining separate compartments within the mitochondrion, each with a distinct role and composition: the outer mitochondrial membrane (OMM), the intermembrane space (IMS), the IMM, and the matrix. The OMM, which is more typical of other membranes in terms of its protein to lipid ratio, is believed to be permeable to most metabolites due the presence of pore-forming porins in its bilayer. In contrast, the highly folded IMM is a tight barrier to all ions and molecules, with an atypically high protein to phospholipid ratio. [28,29] The lipid composition of both membranes is characterized by high phosphatidylcholine (PC) and phosphatidylethanolamine (PE) content and low sterol and sphingolipid count. [28] Additionally, the IMM, and mitochondrial contact sites where the OMM and IMM are in close proximity, display an enrichment of CL, which accounts for up to 20% of total mitochondrial lipids. [28,30,31]

CL was actually first purified in 1942 in an attempt to isolate a substance with serological utility in syphilis testing. Investigators termed the new non-nitrogenous phospholipid “cardiolipin” as it was isolated from bovine heart.[32] In 1964, its structure was first described as a phospholipid consisting of two phosphatidyl moieties, each with

two acyl chains, that are connected by a glycerol bridge.[33] The four acyl chains allow for an array of CL species that enable the observed tissue specific CL composition; CL in the brain is characterized by a diversified array of acyl chains including polyunsaturated chains, whereas in other tissues CL is predominantly characterized by the tetralinoleoyl form, $(18:2)_4$ CL. [34–36] The enrichment of tetralinoleoyl-CL is most obvious in human heart and skeletal muscle where it accounts for up to 80% of the CL species present.[34]

De Novo Synthesis and Remodeling

In eukaryotes, most phospholipids are synthesized in the endoplasmic reticulum (ER); however, the biosynthetic pathway of CL occurs exclusively in the mitochondrion.[37,38] This multi-step process, elucidated over the past 40 years, begins with the generation of phosphatidic acid (PA), which can be potentially sourced from several pathways.[6] PA, synthesized in the ER, on the outer surface of the OMM, or in the IMS, is then transported to the matrix side of the IMM where a condensation reaction between PA and cytidine triphosphate (CTP), catalyzed by Tam41p (Human Gene Organization (HUGO) Gene Nomenclature Committee (HGNC): *TAMM41*, Saccharomyces Genome Database (SGD): *TAM41*), forms cytidine diphosphate diacylglycerol (CDP-DAG).[6,39,40] CDP-DAG and glycerol-3-phosphate (G3P) are then converted to phosphatidylglycerol phosphate (PG-P) by PG-P synthase (HGNC: *PGS1*, SGD: *PGS1*).[41,42] PG-P is rapidly dephosphorylated to PG by PG-P phosphatase (HGNC: *PTPMT1*, SGD: *GEP4*).[43,44] PG is then bound to another molecule of CDP-DAG by CL synthase (HGNC: *CRLS1*, SGD: *CRD1*), an integral IMM protein whose active site faces the mitochondrial matrix, through a condensation reaction that forms nascent CL (Figure 2).[45–48]

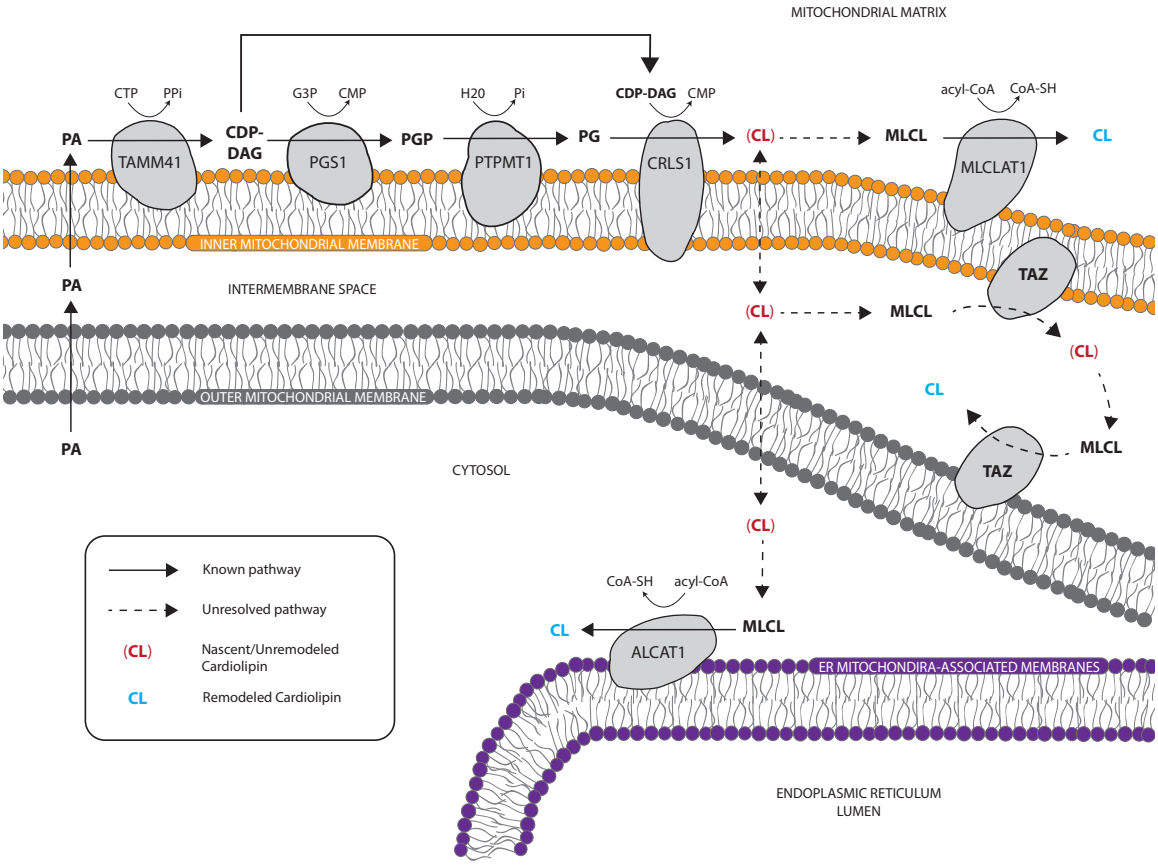

Figure 2. Cardiolipin biosynthesis and remodeling. Phosphatidic acid (PA), sourced from several pathways, is transported to the matrix side of the inner mitochondrial membrane (IMM) where a condensation reaction between PA and cytidine triphosphate (CTP), catalyzed by TAMM41, forms cytidine diphosphate diacylglycerol (CDP-DAG). CDP-DAG and glycerol-3-phosphate (G3P) are then converted to phosphatidylglycerol phosphate (PG-P) by PG-P synthase (PGP1). PG-P is rapidly dephosphorylated to PG by PG-P phosphatase (PTPMT1). PG is then bound to another molecule of CDP-DAG by CL synthase (CRLS1) through a condensation reaction that forms nascent CL. De novo synthesis of nascent CL is followed by CL remodeling, initiated with the removal of an acyl chain, which generates monolyso-CL (MLCL). In mammals, the enzyme(s) that de-acylates nascent CL and generates MLCL is unresolved. Following de-acylation, MLCL is then re-acylated by one of three enzymes: TAZ, MLCL acyltransferase 1 (MLCLAT1), or acyl-CoA:lysocardiolipin acyltransferase-1 (ALCAT1).

De novo synthesis of nascent CL, characterized by saturated acyl chains of variable length and asymmetry with respect to the two chiral centers due to the limited acyl substrate specificity of CRLS1, is followed by CL remodeling which is essential for CL

maturation.[48,49] Remodeling is initiated with the removal of an acyl chain, which generates monolyso-CL (MLCL). In yeast, this is executed by Cld1p; however, there are no known Cld1p orthologs in higher eukaryotes.[50,51] In mammals, several calcium-independent phospholipase A2 (iPLA2) members have been implicated, as these enzymes catalyze the hydrolysis of membrane glycerophospholipids into free fatty acids and lyso-lipids. [52,53] Nonetheless, the question as to which enzyme(s) de-acylates nascent CL and generates MLCL in mammals remains unanswered.

Following de-acylation, MLCL is then re-acylated by one of three enzymes: TAZ, MLCL acyltransferase 1 (MLCLAT1), or acyl-CoA:lysocardiolipin acyltransferase-1 (ALCAT1) (Figure 2).[54–58] TAZ, the assumed predominant enzyme in CL remodeling, catalyzes a reversible transacylation that acts on both sn-1 and sn-2 positions, using any number of phospholipids (PLs) and lyso-PLs as acyl chain donors and acceptors, respectively.[27,56] Deficiency of TAZ results in an increase of the intermediate MLCL, a decrease in mature CL, and an abnormal acyl chain pattern in the remaining CL, the pathognomonic biochemical defect in BTHS.[19,26,59–62] Though the primary biochemical defect in BTHS has been known for several decades, the exact mechanism(s) by which the specific acyl-chain composition of mature CL is generated is still unresolved, and has become the subject of much debate.

Determinants of the acyl chain composition of remodeled CL

When considering the acyl specificity of TAZ the debate has centered on two points; whether TAZ specificity is attributed to the physical properties of lipids and the mitochondrial membrane or whether specificity is attributed to the selectivity of TAZ itself. Schlame et al. first proposed that in the presence of TAZ, transacylations will reshuffle the

acyl residues to optimize lipid packing in curved membranes.[63] In the mitochondrion, bilayer-prone PLs, such as PC, form a stable arrangement of tightly packed lipid molecules. Bending of the bilayer membrane disturbs the packing order of the bilayer PLs, which is thermodynamically unfavorable, but allows for the intermixing of PLs with non-bilayer characteristics such as CL. CL, which has a relatively small polar head group and four acyl chains, that in its mature form are primarily unsaturated, has a cone like structure and preferentially localizes in regions of high membrane curvature.[64] Therefore, acyl specificity is driven by the packing properties of mitochondrial membranes in the final equilibrium state. This is known as the thermodynamic remodeling hypothesis.

Others have proposed that the thermodynamic remodeling hypothesis does not account for all details of TAZ-mediated CL remodeling. Specifically, the model, which suggests that <1% of endogenous mitochondrial PLs participate in transacylation, does not account for the extensive degree of CL remodeling observed in the mammalian heart and skeletal muscle, where tetralinoleoyl-CL accounts for up to 80% of all CL. Secondly, the model suggests that transacylation only occurs in non-bilayer membranes. However, it has not been established whether the curvature of the mitochondrion, which forms the mitochondrial cristae, can be categorized as non-bilayer domains.[65] Third, since CL preferentially localizes in regions of high membrane curvature, it is difficult to distinguish whether the thermodynamic remodeling hypothesis is the key determinant of TAZ acyl chain specificity. Therefore, in 2016, Abe et al, based on their investigation of purified TAZ in liposomes composed of various sets of acyl donors and acceptors, suggested that TAZ does have acyl chain selectivity, and it may be one of the factors in determining the acyl composition of mature CL. [66]

The debate between these two hypotheses has been ongoing. Schlame et al., after repeating and expanding upon the experiments performed by Abe et al., still maintained that acyl specificity of TAZ is driven by the packing properties of non-bilayered mitochondrial membranes in the final equilibrium state. Incubation of yeast TAZ with PC $(18:2)_2$ and MLCL $(18:2)_3$ produced CL $(18:2)_4$ as expected, but incubation of yeast TAZ with PC $(18:1)_2$ and MLCL $(18:2)_3$ produced four different species. Schlame et al. suggest that the incorporation of multiple 18:1 residues in CL is only possible if TAZ transfers not only 18:1 from PC to MLCL, but also transfers 18:2 from CL to lyso-PC, and that the bidirectional exchange of acyl groups cannot be under kinetic control. Abe et al. do agree that there are multiple exchanges of acyl chains that occur in TAZ-mediated transacylation, but they continue to argue that transacylation can occur in rigid lipid bilayers, such as liposomes, and that TAZ does have a degree of acyl chain specificity. Using a series of liposomes composed of different derivatives of dipalmitoleoyl $(16:1)_2$ PC they investigated the TAZ-mediated transacylation reaction between different PCs and MLCL, and found that TAZ strictly discriminates the molecular configuration of the PC acyl chains. Further, they suggest that the final acyl composition may result from a coordinated effort between a deacylase, Cld1p in yeast and yet to be identified in humans, and TAZ.

Recently, several groups have demonstrated that Cld1p, the deacylase upstream of Taz1p that was identified in yeast by Beranek et al., has selectivity as to which mitochondrial CLs it deacylates.[50,67,68] Specifically, biochemical studies and computer modeling confirmed the selectivity of Cld1p toward $(16:0)_4$, $(16:1)(16:0)_3$, and $(18:0)_4$-CL substrates and the preservation of $(18:1)_4$, and $(18:2)_4$-CL species. Therefore, the specificity of Cld1p controls the MLCL available for Taz1p to re-acylate.[51,68] Even

though the deacylase acting upstream of human TAZ has yet to be identified, we must still consider the potential contribution of a deacylase in dictating the final acyl chain composition of CL. Additionally, another determinant of the acyl chain composition of CL could be the availability of acyl chain donors, as dietary supplementation can shift the acyl chain pattern of PLs.[69,70] As the debate continues, perhaps the explanation with regards to the acyl specificity of TAZ will be a combination of each component: the packing properties of the mitochondrial membrane, the acyl specificity of TAZ itself, the role of a deacylase acting upstream of TAZ, and the availability of acyl chain donors.

Genotype-Phenotype Relationship: The role of MLCL:CL

BTHS is a result of pathogenic variants within *TAZ*, which can be identified by molecular genetic testing. To date there are over 120 causative variants that have been reported in every exon except for exon 5, including missense, nonsense, splice variants, small insertions/deletions, and large deletions.[17] In addition to molecular genetic testing, a BTHS diagnosis can be established by an increased MLCL:CL ratio, which is detectable in multiple biological specimens including bloodspots, lymphocytes, and muscle tissue. The measurement of MLCL:CL has a diagnostic sensitivity and specificity of 100%.

Investigations of different yeast lines, representing 21 distinct and conserved human *TAZ* pathogenic variants, have established seven functional classes of *TAZ* genetic variation. The first and the largest class, includes variants that result in the production of little to no functional TAZ. The remaining classes include; (2) Mitochondrial mislocalization and aggregate prone; (3) Impaired macromolecular assembly; (4) Catalytically null; (5) Hypomorphs with residual transacylase activity; (6) Degradation due to impaired folding and assembly; and (7) Temperature sensitive.[71,72] Distinct loss of

function (LOF) classes with potential for residual TAZ function suggest a possible genotype-phenotype correlation; however, prior clinical phenotyping studies have not identified such a relationship. [71,72]

Recently, a possible "CL metabotype"- phenotype relationship was established. In 2015, Bowron et al. reported 7 BTHS individuals with a modified clinical phenotype, increased MLCL, and an increased MLCL:CL ratio, but a normal level of CL.[73] The *TAZ* variants identified in these individuals were: p.Arg57Leu, p.Asn40Asp, and p.Met185Val. The substitution, p.Met185Val (C.553A>G), generates a new splice donor site within exon 7 resulting in the retention of intron 6 and a partial deletion of exon 7, confirming pathogenicity.[74] The variants, p.Arg57Leu (R57L) and p.Asn40Asp (N40D) have both been modeled in yeast; R57L/K65L is a temperature sensitive allele with reduced transacylase activity and N40D/N48D has activity identical to WT72. Therefore, the pathogenicity of N40D remains unproven.

The presentation of a modified clinical phenotype associated with a modified metabotype (elevated MLCL and normal CL) was again identified in 2016 in a multidisciplinary investigation of 42 individuals with BTHS. In this study, researchers identified several individuals with a relatively milder skeletal muscle phenotype and the modified metabotype. These modified metabotype-phenotypes were associated with the genotypes c.583+5G>A and c.873_874dupCCTGG (p.Arg292LeufsX49). They further found that MLCL:CL was inversely correlated to skeletal muscle endurance and directly correlated to left ventricular size, offering further evidence for a genotype-metabotype-phenotype relationship. As a rare disorder with isolated familial variants, continued efforts in establishing a genotype-metabotype-phenotype relationship will not only inform patient

care, but help elucidate the disease mechanism of TAZ deficiency and abnormal CL content.

Cardiolipin function: everything but the kitchen sink

Since its initial isolation in 1942, and throughout almost 2000 publications, CL has a been implicated in a laundry list of functions within the mitochondrion (Figure 3). Many proteins are known to interact with CL, in both structural and functional capacities, which establishes the foundation for CL's multifaceted role within the mitochondrion.[75] The essentiality of CL is highlighted by the observation that *ptpmt1*$^{-/-}$ mice, an enzyme essential for CL synthesis, die *in utero* prior to E8.5.44.

CL composes up to 20% of the phospholipid mass of the IMM and is critical for mitochondrial cristae formation, based on observations of abnormal IMM ultrastructure in CL-deficient models.[76–78] The mitochondrial cristae house the oxidative phosphorylation (OXPHOS) system. Therefore, it is not surprising that CL also plays a critical role in the efficiency and adaptability of the OXPHOS machinery. First, CL stabilizes the higher order assemblies of the individual respiratory complexes into respiratory supercomplexes (SCs), which are combinations of respiratory complexes I, III, and IV.[79–87] SC assembly is thought to increase the efficiency of electron transfer in OXPHOS, maximize OXPHOS function, minimize reactive oxygen species (ROS) production, and thereby reduce oxidative damage. Second, CL is proposed to act as a proton trap, restricting the diffusion of protons and funneling them toward ATP synthase to generate ATP.[88] Lastly, once ATP is formed by OXPHOS, it then passes across the IMM to the IMS via the ADP/ATP carrier. CL is needed for not only the stabilization of the carrier, but is also required for the association of the carrier with the OXPHOS

SCs.[89,90] Besides the ADP/ATP carrier, CL also plays a plays a protective and stabilizing role for various mitochondrial carriers (Figure 3).[91]

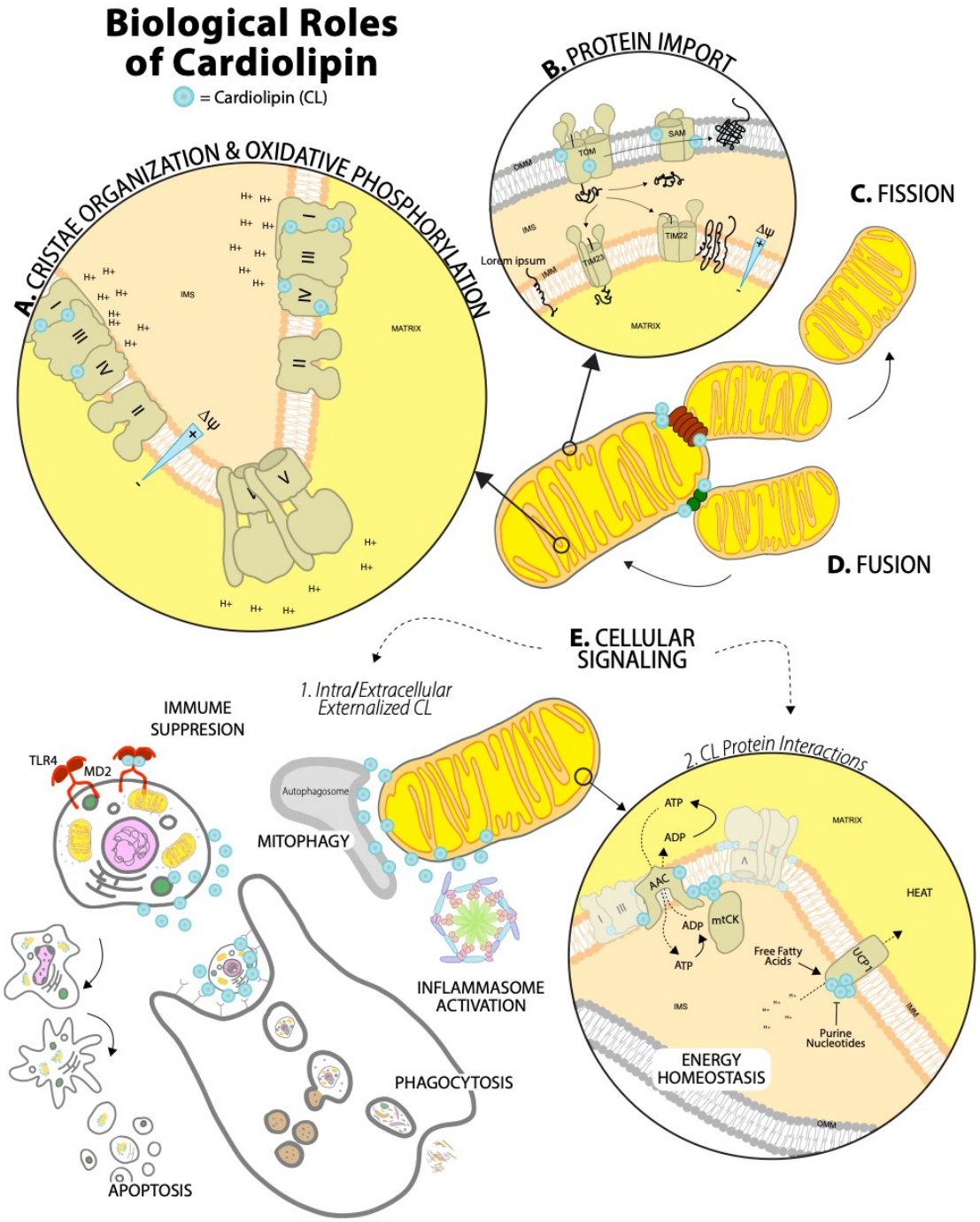

Figure 3. Biological roles of cardiolipin. (A) Cardiolipin (CL) is critical for mitochondrial cristae formation.[76–78] Within the cristae, CL plays a critical role in the efficiency and adaptability of the oxidative phosphorylation (OXPHOS) machinery, by stabilizing the

assembly of respiratory supercomplexes (SCs). SC assembly is thought to increase the efficiency of electron transfer in OXPHOS, maximize OXPHOS function, minimize reactive oxygen species (ROS) production, and thereby reduce oxidative damage. [79–87] **(B)** Reduced functionality of OXPHOS decreases the mitochondrial membrane potential, which negatively affects protein import into the IMM and mitochondrial matrix by IMM translocases, TIM22 and TIM23.[92] Separately, CL is also important for the assembly and function of OM translocases, TOM and SAM.[93] Together, CL is critical for mitochondrial biogenesis, which requires the import of a large number of proteins from the cytosol. **(C)** CL is also crucial for mitochondrial fission and **(D)** fusion, where cells reorganize the highly dynamic mitochondrial organelles by altering their shape, localization, and cellular number. [94,95] **(E1)** Intra/extracellular externalized CL is a critical signaling component in mitophagy, apoptosis, and multiple distinct immune responses, such as inflammasome activation and phagocytosis.[107,112–114] Extracellular externalized CL can be bound by the phagocyte Toll-like receptor 4 (TLR4)/Md2, which acts as a structural homologue of antigenically inactive immature Lipid A and suppresses TLR4/Md2 driven cytokine production, thus acting as an immune suppressor.[107] **(E2)** Many proteins are known to interact with CL, and recently a role for CL in the activation of thermogenic adipocytes was defined. CL may be involved in the direct activation of the thermogenic effector, UCP1, and/or decrease UCP1's binding affinity for inhibitory purine nucleotides. [117] Additionally, CL also physically interacts with creatine kinase (mtCK), an enzyme that drives thermogenesis in beige fat.[118]

CL is critical for mitochondrial biogenesis, which requires the import of a large number of proteins from the cytosol. Reduced functionality of OXPHOS in the absence of CL decreases the mitochondrial membrane potential, which negatively affects protein import into the IMM and mitochondrial matrix by IMM translocases, TIM22 and TIM23.[92] Separately, CL is also important for the assembly and function of OM translocases, TOM and SAM.[93] CL is also intimately involved in mitochondrial fusion and fission whose combined actions promote mitochondrial fitness and biogenesis (Figure 3).[94,95] There are several superb reviews which thoroughly discuss the aforementioned CL-supported functions: Chicco and Sparangna 2007, Houtkooper and Vaz 2008, Lewis and McElhaney 2009, Klingenberg 2009, Claypool and Koehler 2012, Paradies et al. 2014, Li et al. 2015, Musatov and Sedlák 2017, Ikon and Ryan 2017.[14,91,96–103]

Recently, there has been an emphasis on CL as a signaling molecule. In healthy cells, CL is localized in the IMM, whereas in damaged cells, CL externalizes to the OMM as an elimination signal. Once externalized, CL can bind and activate LC3-II, which initiates autophagosome formation resulting in mitophagy, the selective degradation of mitochondria. Further, under oxidative stress, the production of ROS results in the peroxidation of CL by Cytochrome c (Cyt c) and its subsequent externalization to the OMM as a damage signal for apoptosis, programmed cell death (Figure 3).[104–106] Extracellular externalized CL (e.g. outside of plasma membrane) is thought to have an additional role in some immune responses, such as the attraction of phagocytes through the cell surface receptor CD36, resulting in rapid degradation of the cell with extracellular externalized CL.[107] In addition to signaling the rapid removal of mitochondria and bacteria by phagocytosis, externalized CLs may also play a role in regulating the inflammatory response elicited by bacteria. CL can be bound by the phagocyte Toll-like receptor 4 (TLR4)/Md2, which acts as a structural homologue of antigenically inactive immature Lipid A and suppresses TLR4/Md2 driven cytokine production, thus acting as an immune suppressor.[107] If the innate immune system fails, or if there is a constant release of mitochondria/mitochondrial fragments with externalized CL due to cell death, the continuous presence of CL can activate antigen-presenting cells (APCs). This then stimulates an adaptive immune response resulting in the production of anti-CL antibodies and potentially autoimmune disease.[108,109] In addition to extracellular externalized CL, intracellular externalized CL (e.g. exposed to cytosol) has also been suggested to directly activate inflammasomes, such as NLRP3.[110,111] To summarize, CL and its oxidized products are critical signaling components in mitophagy, cell death, and multiple distinct

immune responses (Figure 3).[112–114] As an already diverse signaling molecule, there are likely further undiscovered roles for CL in this regard.

Recently, researchers have defined a role for CL in the activation of thermogenic adipocytes. Brown adipose tissue (BAT) converts carbohydrate and lipid substrates to thermal energy in response to cold environments. Lynes et al. measured cold-activated lipid landscapes in blood and adipose tissue by MS/MSALL, and among the 1,600 unique lipid species profiled, they identified the CL biosynthetic pathway as coordinately activated in brown and beige fat by cold.[115] Further, they found CRLS1, the gene encoding CL synthase, to be significantly enriched in cold-induced interscapular BAT as compared with other metabolic tissues, and that loss of CRLS1, and therefore CL, abolished the thermogenic capacity of the adipose tissue.[116] This suggests that CL is likely to have brown and beige fat-specific functions in thermogenesis. Previous studies have demonstrated that CL binds to the uncoupling protein, UCP1, and assists its proper folding. Therefore, CL may function through the direct activation of the thermogenic effector UCP1.[117] Additionally, CL also physically interacts with creatine kinase, an enzyme that drives thermogenesis in beige fat.[118] Together, this suggests that CL is critical for thermogenic mechanisms, adding to the ever growing list of CL functions (Figure 3).

Cardiolipin metabolism and mitochondrial dysfunction in human health: Not just Barth Syndrome

BTHS, a severe multi-system disorder caused by abnormal CL remodeling, highlights the importance of CL in human health (Figure 1). In addition to the cardinal clinical phenotypes of BTHS (cardiomyopathy, neutropenia, etc), metabolite profiles of a BTHS cohort compared to age-matched controls revealed broad metabolic dysregulation with vast

cellular implications that include: insulin regulation of fatty acid metabolism, lipid metabolism, biogenic amine metabolism, amino acid metabolism, endothelial nitric oxide synthase signaling, and tRNA biosynthesis.[119]

As a prominent player in both mitochondrial and cellular activities, it is not surprising that altered CL content and/or quantity is associated with mitochondrial dysfunction in an array of metabolic and aging-related pathological conditions.[96,100,101,120] Mitochondria, and specifically CL, are thought to be intimately involved in the aging process, characterized by the gradual deterioration of various physiologic and metabolic processes, with increased oxidative stress and an attenuated ability to respond to other stresses.[121] While aging itself may not be considered pathologic, with aging there is an increased risk of acquiring age-associated disorders, especially with regards to brain and heart function.[122–125] In Alzheimer's (AD) and Parkinson's (PD), two common age-related neurological disorders, CL is suggested to have a role in disease pathogenesis.[126–128] In an AD transgenic mouse model, lipidomics revealed not only an overall reduction in CL amount, but an altered CL species profile, specifically reduced levels of unsaturated acyl chains.[126] Studies in induced pluripotent stem cells (iPSC) and embryonic stem cells (ESC) expressing variants in SNCA (encoding α-synuclein (α-syn)), the causal gene in familial PD, revealed that CL translocates to the OMM and binds to α-syn where it facilitates the folding of α-syn to its α-helical, ordered state.[127,128] Therefore, altered CL content and/or composition, may result in misfolding and aggregation of α-syn, a key molecular event in the pathogenesis of PD. Additionally, with age, an individual is also at risk for ischemia/reperfusion (I/R) injury, which contributes to pathology in a range of conditions, such as myocardial

infarction and ischemic stroke. In multiple organs, such as the brain, heart, and liver, I/R injury significantly changes the distribution of CL molecular species with an accumulation of oxidized CL. [129–131]

Diabetes and obesity, with systemic oxidative stress and mitochondrial dysfunction, is also associated with altered CL content.[70,120,132–135] In a type I diabetic mouse model, there is depletion of tetralinoleoyl-CL as well as a diversification in its molecular speciation in heart tissue, with a significant increase in CL species containing fatty acyl chains longer than 18 carbons.[132,133] Similar to the type I model, a type II diabetic mouse model also has an altered CL profile.[132,133] Cardiac tissue from obese mice, due to a high fat diet, display a significantly altered CL species profile, specifically an increase in n-6 and n-3 polysaturation.[70]

Abnormalities in CL, including CL peroxidation, have also been associated with nonalcoholic fatty liver disease (NAFLD), one of the most common forms of liver disease, which has the potential to advance to nonalcoholic steatohepatitis (NASH), liver fibrosis, and liver failure.[136,137] As further evidence for the role of CL in NASH, in a choline-deficient rat model of induced fatty liver disease total CL content is significantly reduced, and peroxidized CL is increased.[138,139] It is currently unclear if the abnormal CL is a product of increased oxidative stress and IMM dysfunction in this disease, or if abnormalities in CL are a primary factor with downstream effects on OXPHOS and augmented production of ROS. Regardless, CL represents a target of interest in unraveling the pathophysiology of NAFLD and NASH.

Abnormalities in CL also have been shown in several models of malignancy. TAZ expression gradually increases from normal cervical tissue to squamous cervical

carcinoma, suggesting that TAZ and CL remodeling may contribute to the progression of cervical cancer.[140] Further, shotgun lipidomics from subcutaneously grown brain tumors, including astrocytomas, stem cell tumors, and microgliomas, revealed major abnormalities in CL content/composition.[141] Together, these findings suggest that altered CL is associated with malignant cell metabolism, possibly via inhibition of apoptosis or as a driver of adaptations in global cellular bioenergetics (i.e. the Warburg theory).[140,141]

Abnormalities in CL are the primary cellular defect underlying the Mendelian disease Barth syndrome, as well as part of the pathologic process in multiple common, multifactorial diseases. As such, models of BTHS have the potential to not only elucidate the underlying disease mechanism of TAZ deficiency in BTHS, but to inform the pathophysiology of common and complex diseases associated with altered CL metabolism.

1.2.6 Barth Syndrome Models

Since the identification of the gene responsible for BTHS, several models of TAZ deficiency have been generated, which all recapitulate the primary BTHS biochemical abnormality; an increased MLCL:CL ratio and an abnormal acyl chain composition of the remaining CL (Table 1). The first model generated was the *S. cerevisiae* yeast model, *taz*1Δ, which contains a null variant in the homologue of human *TAZ*. [142,143] Studies in yeast, which represent a proven model for mitochondrial disease, encompass the majority of our understanding of the role TAZ deficiency and abnormal CL metabolism in mitochondrial dysfunction. [144,145] Characterization of the yeast model, *taz*1Δ, has connected altered CL metabolism with OXPHOS dysfunction with or without aberrant SC

assembly, IMM uncoupling, increased oxidative stress, and impaired iron homeostasis (Table 1).[142,143,146–149]

Three animal models of TAZ deficiency have been developed: a *TAZ* knockout (*TAZ*KO) fruit fly, a morpholino induced *TAZ* knockdown (*TAZ*KD) zebrafish, and a doxycycline short hairpin RNA-induced *TAZ*KD mouse model.[77,78,150,151] *TAZ*KO fruit flies exhibit motor weakness, reduced flying and climbing abilities, and reduced endurance, which parallels the exercise intolerance of many BTHS individuals.[150,152] *TAZ*KD zebrafish have severe developmental and growth retardation with the cardiac phenotypes of bradycardia, pericardial effusions, and generalized edema.[151] *TAZ*KD mice recapitulate many of the cardiac phenotypes in BTHS, including left ventricular dilation, reduced left ventricular mass, and reduced ejection (Table 1). [77,78]

There are also numerous in vitro cellular models of both primary and immortalized cells; BTHS patient neutrophils, BTHS patient-derived fibroblasts and lymphoblast cell lines, *TAZ*KO and *TAZ*KD mouse embryonic stem cell (ES) lines, *TAZ*KD Human pro-myelocytic HL-60 progenitor (HL60) cell lines, *TAZ*KO and *TAZ* knock-in (*TAZ*KI) HEK293 cell lines, patient derived and engineered *TAZ*KO induced pluripotent stem cell (iPSC) lines, *TAZ*KO C2C12 myoblast cell lines, and *TAZ*KO H9c2 cell lines (Table 1).[21,119,161,153–160] Collectively, these cellular models display low basal respiration, low membrane potential, diminished OXPHOS, and destabilization OXPHOS SCs. Two models of note, the *TAZ*KO and *TAZ*KI HEK293s and patient derived and engineered *TAZ*KO iPSCs, allow for human-based studies in a variant and tissue specific context.

Table 1. Barth Syndrome model systems

Model	Gene	Gene Location	Protein	System	Phenotypes	Ref.
Yeast	*TAZ1*	ChrXVI: 814,349–815, 536	taz1	(KO) *taz*1Δ	• OXPHOS dysfunction with or without aberrant SC assembly • IMM uncoupling • Increased oxidative stress • Impaired iron homeostasis	142, 143, 146-149
Fruit Fly	*Taz*	Chr2R: 12,753,026–12,756,414 [-]	Taz	(KO) *TAZ* -/-	• Motor weakness • Reduced flying and climbing abilities • Reduced endurance	150, 152
Zebra Fish	*Taz*	Chr23: 4,915,595–4,925,724	Taz	(KD) asMO-mediated	• Severe developmental and growth retardation • Cardiac phenotypes: bradycardia, pericardial effusions, and generalized edema	151
Mouse	*Taz*	ChrX: 74,281,912–74,290,151	TAZ	(KD) Dox induction	• Cardiac phenotypes: left ventricular dilation, reduced left ventricular mass, and reduced ejection	77,78
Human	*TAZ*	ChrX: 154,411,518–154,421,726	TAZ	• BTHS Patient neutrophils • BTHS patient – derived fibroblasts • BTHS patient – derived lymphoblasts • BTHS patient – derived iPSCs • KO/KI engineered iPSCs • KD Human pro – myelocytic • (HL60) cells • KO/KI Human embryonic kidney cells (HEKs) • KO C2C12 myoblast cells • KO H9c2 cells	• Low basal respiration • OXPHOS dysfunction • Aberrant SC assembly • Smaller and fragmented mitochondria	21, 119, 153-161

To establish a novel mammalian BTHS model, Lu et al. utilized TALEN-mediated genome editing in Flp-In 293 cells, modified HEK293s which contain a single stably integrated FRT site, to generate a *TAZ*KO line, taz^{TALEN}.[23] A detailed characterization of endogenous TAZ in the taz^{TALEN} line revealed that mammalian TAZ, as previously determined in yeast, is localized to the mitochondrion, where it associates non-integrally with IMS-facing membranes and assembles in a range of complexes. Further, using the integrated FRT site to express two TAZ variants of interest, R57L and H69Q, Lu et al.

confirmed LOF mechanisms previously modeled in yeast. This human cellular model substantiated the power of modeling BTHS in yeast, as well as provided a framework with which to investigate the consequences of individual *TAZ* variants, which could prove invaluable in therapeutic discovery and validation.

Like the *TAZ*KO and *TAZ*KI HEK293 cell lines, the recent development of iPSCs allows for the investigation of TAZ deficiency and abnormal CL metabolism in a *TAZ*-variant specific context. Additionally, unlike the HEK293s, the use of iPSCs allow for investigations in a disease relevant cell type. This is of particular interest in BTHS, which clinically affects specific tissue types and metabolically affects CL composition, which is inherently tissue specific. Wang et al. established two BTHS patient derived iPSC lines, one with a deletion resulting in a frameshift (c.517delG, BTHH) and one with a missense variant (c.328C>T, BTHC), as well as two engineered lines using CRISPR-Cas9 genome editing, one with the same deletion (PGP1-TAZ$^{c.517delG}$) and one with a 14 base pair insertion (PGP1-TAZ$^{c.517ins}$).156 Extensive characterization following differentiation into cardiomyocytes (iPSC-CMs), which recapitulated the characteristic BTHS cardiolipin findings, revealed smaller and fragmented mitochondria, reduced peak OXPHOS function, and decreased ATP production in the absence of TAZ. When seeded on micropatterned fibronectin rectangles designed to mimic adult cardiomyocytes, BTHS iPSC-CMs assembled into sparse and irregular sarcomeres, and when seeded onto muscular thin film (MTF) chips the irregular sarcomeres displayed weak contraction.

Each unique model has provided mechanistic insight into the pathophysiology of BTHS (Table 1) and holds potential for the ascertainment of new therapeutic targets and strategies.

1.2.6 Barth Syndrome Therapies

Currently, there are no disease specific treatments for BTHS. Affected individuals are treated symptomatically with vigilant surveillance and management by medical specialists in metabolism, cardiology, hematology, genetic counseling, physical therapy, and nutrition. Therapeutic development has focused on four main therapeutic strategies; lipid replacement, enzyme replacement, gene replacement, and drug therapy (Figure 4).

The pathognomonic metabolic defect in BTHS is an increase in MLCL and a decrease in mature CL, specifically tetralinoleoyl-CL, resulting in an overall increased MLCL:CL. In order to compensate for TAZ activity, the supplementation of CL, or lipid replacement, may be a reasonable approach (Figure 4). This approach was previously tested in vitro, where BTHS fibroblasts, supplemented with linoleic acid, showed a time and dose dependent increase in tetralinoleoyl-CL. [162] Additionally, *TAZ*KD HL-60 cells incubated with CL nanodisks (ND), which delivered tetralinoleoyl-CL to mitochondria, displayed an attenuated apoptotic response. [163] Based on this research, Ikon et al. sought to determine the feasibility of this approach in an in vivo model. Unfortunately, lipidomics revealed that the CL-ND failed to alter the CL profile of WT or doxycycline short hairpin RNA-induced *TAZ*KD mice. [164] Though CL-ND are not a viable option, this research highlights the importance of using both *in vitro* and *in vivo* modeling in therapeutic discovery and testing.

In another approach to lipid replacement, Ball et al. suggested supplementing ethanolamine (Etn) in order to increase cellular PE.[165] PE, which can function in an overlapping manner with CL, could then potentially rescue the respiratory chain defects of

cells with altered CL metabolism. Interestingly, using the yeast models, *taz*1Δ and *crd*1Δ, Ball et al. showed that Etn ameliorates mitochondrial function, however, without increasing PE levels. Instead, Etn restored OXPHOS SC formation through increased expression of complex III and IV subunits. As an area of ongoing research it will be interesting to see the viability of this approach in mammalian models (*in vitro* and *in vivo*), especially since previous research has demonstrated the difficulties in translating successful treatments between in vivo and in vitro models.

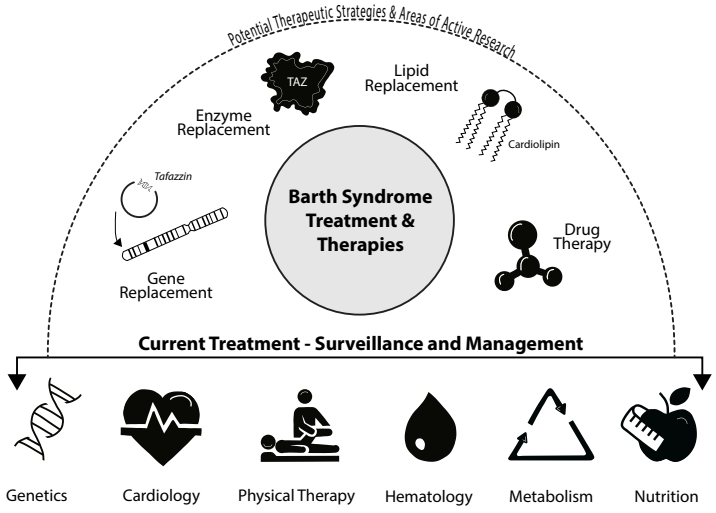

Figure 4. Barth syndrome therapeutic strategies. BTHS patients are treated symptomatically with vigilant surveillance and management by clinical teams composed of medical specialists in genetics, cardiology, physical therapy, hematology, metabolism, and nutrition. Therapeutic research has focused on four main areas of therapeutic strategies; gene, replacement, enzyme replacement, lipid replacement, and drug therapy.

Direct replacement of the TAZ enzyme is also a therapeutic approach under investigation (Figure 4). Working towards this goal, Dinca et al. have identified the mitochondrial localization signals in TAZ, TAZ (84–95) and TAZ (185–220). The TAZ (84-95) sequence, located in exon 3, targets TAZ exclusively to the mitochondrion and is sufficient to direct eGFP to mitochondria in TAZ deficient cells.161 The identification of

this 12 amino acid localization sequence may be the first step towards engineering a TAZ protein sequence that can be used for enzyme replacement therapy (ERT). Research into the in vivo applicability of TAZ ERT is currently underway.

Replacement of the defective *TAZ* gene, or gene replacement therapy, is another therapeutic approach (Figure 4). As with enzyme replacement, delivery is the biggest hurdle in gene replacement. Recombinant adeno-associated virus (rAAV) vectors are often used for gene delivery because these vectors are derived from a nonpathogenic virus that elicits a minimal immune response and do not carry a risk of insertional mutagenesis. In order to optimize an AAV vector for *TAZ* delivery, Suzuki-Hatano et al. compared three AAV2/9-*TAZ* vectors with different promoters following their intravenous administration into doxycycline short hairpin RNA-induced *TAZ*KD mice.[166] Of the three promoters, the desmin (Des) promoter was found to provide significant improvement in various assessments as compared to *TAZ*KD controls. Of the 28 listed measurements, the Des-*TAZ* treated mice showed significant improvement in 6 measurements: *TAZ* transcription, *TAZ* translation, force mechanics, mitochondrial area, mitochondrial width, and mitochondrial oxygen consumption. It is not yet known how the effects of this gene replacement strategy will translate to patients.

In terms of small molecule/ drug therapies for BTHS (Figure 4), there is an ongoing clinical trial testing the safety, tolerability, and efficacy of Elamipretide in Barth Syndrome sponsored by Stealth BioTherapeutics Inc. (ClinicalTrials.gov Identifier: NCT03098797). [167] Elamipretide, also known as SS-31 (D-Arg-dimethylTyr-Lys-Phe-NH2), was first developed in 2004 by Zhao et al. as part of a series of peptide antioxidants, Szeto-Schiller peptides (SS peptides), that are targeted to the mitochondrion and concentrated in the

IMM.[168] Since its development, it has been reported that SS-31 binds with high affinity to CL and that the SS-31/CL complex inhibits CL peroxidation by Cyt. C and optimizes OXPHOS.[169–172] In addition to its therapeutic potential, a greater understanding SS-31's mechanism of action in improving mitochondrial function may provide insight into the pathophysiology of BTHS.

1.2.7 Conclusion

Even with the significant advancements described in this review, our understanding of the pathophysiology of BTHS remains relatively limited. Specifically, the role of TAZ in determining of the acyl chain composition of remodeled CL (Figure 3), and how TAZ deficiency results in the cardinal phenotypes of BTHS (Figure 1) have not been resolved. In addition to BTHS, altered CL metabolism is also observed in various common and complex diseases are associated with altered CL metabolism. Therefore, additional studies with a variety of model systems (Table 1), including human-based models that are variant and tissue specific, will not only provide answers relevant to BTHS, but address the role of CL metabolism in other common and complex diseases.

1.2.8 References

1. P. G. Barth, et al., An X-linked mitochondrial disease affecting cardiac muscle, skeletal muscle and neutrophil leucocytes — Preliminary communication in Mitochondria and Muscular Disorders: The Proceedings of a Symposium Held at the Erasmus University, Rotterdam, 11th-12th December 1980, H. F. M. Busch, F. G. . Jennekens, H. R. Scholte, Eds. (Mefar B.V., 1981), pp. 161–164.
2. P. G. Barth, et al., An X-linked mitochondrial disease affecting cardiac muscle, skeletal muscle and neutrophil leucocytes. J. Neurol. Sci. 62, 327–355 (1983).
3. L. Ades, et al., Barth syndrome: Clinical Features and Confirmation of Gene Localization to Distal Xq28. Am. J. Med. Genet. 45, 327–334 (1993).
4. C. Ferreira, R. Thompson, H. Vernon, "Barth Syndrome" in GeneReviews®[Internet], 1993rd–2018th Ed., M. P. Adam, H. H. Ardinger, R. A. Pagon, S. E. Wallace, Eds. (University of Washington, 2014) https:/doi.org/NBK247162 [bookaccession].
5. A. E. Roberts, et al., The Barth Syndrome Registry: Distinguishing disease characteristics and growth data from a longitudinal study. Am. J. Med. Genet. Part A 158 A, 2726–2732 (2012).

6. Y. W. Lu, S. M. Claypool, Disorders of phospholipid metabolism: An emerging class of mitochondrial disease due to defects in nuclear genes. Front. Genet. 6 (2015).
7. S. L. N. Clarke, et al., Barth Syndrome. Orphanet J. Rare Dis. 8 (2013).
8. Barth Syndrome Foundation.
9. C. T. Spencer, et al., Ventricular arrhythmia in the X-linked cardiomyopathy Barth syndrome. Pediatr. Cardiol. 26, 632–637 (2005).
10. W. R. Thompson, et al., New targets for monitoring and therapy in Barth syndrome. Genet. Med. 18, 1001–1010 (2016).
11. R. I. Kelley, et al., X-linked dilated cardiomyopathy with neutropenia, growth retardation, and 3-methylglutaconic aciduria. J. Pediatr. 119, 738–747 (1991).
12. C. Rigaud, et al., Natural history of Barth syndrome: a national cohort study of 22 patients. Orphanet J. Rare Dis. 8 (2013).
13. J. Mangat, T. Lunnon-Wood, P. Rees, M. Elliott, M. Burch, Successful cardiac transplantation in Barth syndrome - Single-centre experience of four patients. Pediatr. Transplant. 11, 327–31 (2007).
14. P. A. Bolhuis, G. W. Hensels, T. J. Hulsebos, F. Baas, P. G. Barth, Mapping of the locus for X-linked cardioskeletal myopathy with neutropenia and abnormal mitochondria (Barth syndrome) to Xq28. Am. J. Hum. Genet. 48, 481–5 (1991).
15. A. K. Gedeon, M. J. Wilson, A. C. Colley, D. O. Sillence, J. C. Mulley, X linked fatal infantile cardiomyopathy maps to Xq28 and is possibly allelic to Barth syndrome. J. Med. Genet. 32, 383–8 (1995).
16. S. Bione, et al., A novel X-linked gene, G4.5. is responsible for Barth syndrome. Nat. Genet. 12, 385–389 (1996).
17. I. L. Gonzalez, Barth syndrome: TAZ gene mutations, mRNAs, and evolution. Am. J. Med. Genet. 134 A, 409–414 (2005).
18. S. M. Kirwin, A. Manolakos, S. S. Barnett, I. L. Gonzalez, Tafazzin splice variants and mutations in Barth syndrome. Mol. Genet. Metab. 111, 26–32 (2014).
19. R. H. Houtkooper, et al., The enigmatic role of tafazzin in cardiolipin metabolism. Biochim. Biophys. Acta - Biomembr. 1788, 2003–2014 (2009).
20. F. M. Vaz, R. H. Houtkooper, F. Valianpour, P. G. Barth, R. J. A. Wanders, Only One Splice Variant of the Human TAZ Gene Encodes a Functional Protein with a Role in Cardiolipin Metabolism. J. Biol. Chem. 278, 43089–43094 (2003).
21. Y. Xu, J. J. Sutachan, H. Plesken, R. I. Kelley, M. Schlame, Characterization of lymphoblast mitochondria from patients with Barth syndrome. Lab. Investig. 85, 823–830 (2005).
22. Y. Xu, et al., Characterization of tafazzin splice variants from humans and fruit flies. J. Biol. Chem. 284, 29230–29239 (2009).
23. Y. W. Lu, et al., Defining functional classes of Barth syndrome mutation in humans. Hum. Mol. Genet. 25, 1754–1770 (2016).
24. A. Hijikata, K. Yura, O. Ohara, M. Go, Structural and functional analyses of Barth syndrome-causing mutations and alternative splicing in the tafazzin acyltransferase domain. Meta Gene 4, 92–106 (2015).
25. A. F. Neuwald, Barth syndrome may be due to an acyltransferase deficiency. Nucleic Acids Res. 7, 465–466 (1966).
26. P. Vreken, et al., Defective remodeling of cardiolipin and phosphatidylglycerol in Barth syndrome. Biochem. Biophys. Res. Commun. 279, 378–382 (2000).
27. Y. Xu, A. Malhotra, M. Ren, M. Schlame, The enzymatic function of tafazzin. J. Biol. Chem. 281, 39217–39224 (2006).
28. S. E. Horvath, G. Daum, Lipids of mitochondria. Prog. Lipid Res. 52, 590–614 (2013).
29. W. Kühlbrandt, Structure and function of mitochondrial membrane protein complexes. BMC Biol. 13, 1–11 (2015).
30. D. Ardail, et al., Mitochondrial contact sites. Lipid composition and dynamics. J. Biol. Chem. 265, 18797–802 (1990).
31. R. Hovius, J. Thijssen, P. Vanderlinden, K. Nicolay, B. Dekruijff, Phospholipid asymmetry of the outer nembrane of rat liver mitochondria: Evidence for the presence of cardiolipin on the outside of the outer membrane. FEBS Lett. 330, 71–76 (1993).

32. M. C. Pangborn, Isolation and purification of a serologically active phospholipid from beef heart. J. Biol. Chem. 143, 247–256 (1942).
33. J. LeCocq, C. E. Ballou, On the Structure of Cardiolipin. Biochemistry 3, 976–980 (1964).
34. M. Schlame, M. Ren, Y. Xu, M. L. Greenberg, I. Haller, Molecular symmetry in mitochondrial cardiolipins. Chem. Phys. Lipids 138, 38–49 (2005).
35. H. Cheng, et al., Shotgun lipidomics reveals the temporally dependent, highly diversified cardiolipin profile in the mammalian brain: Temporally coordinated postnatal diversification of cardiolipin molecular species with neuronal remodeling. Biochemistry 47, 5869–5880 (2008).
36. A. A. Amoscato, et al., Imaging mass spectrometry of diversified cardiolipin molecular species in the brain. Anal. Chem. 86, 6587–6595 (2014).
37. K. Y. Hostetler, H. Van Den Bosch, L. L. M. Van Deenen, Biosynthesis of cardiolipin in liver mitochondria. Biochim. Biophys. Acta 239, 113–119 (1971).
38. E. M. Mejia, H. Nguyen, G. M. Hatch, Mammalian cardiolipin biosynthesis. Chem. Phys. Lipids 179, 11–16 (2014).
39. Y. Tamura, et al., Identification of Tam41 maintaining integrity of the TIM23 protein translocator complex in mitochondria. J. Cell Biol. 174, 631–637 (2006).
40. Y. Tamura, T. Endo, Unveiling the last missing link of the cardiolipin synthetic pathway in mitochondria. Aging (Albany. NY). 5, 392–393 (2013).
41. S. C. Chang, P. N. Heacock, C. J. Clancey, W. Dowhan, The PEL1 gene (renamed PGS1) encodes the phosphatidylglycerophosphate synthase of Saccharomyces cerevisiae. J. Biol. Chem. 273, 9829–9836 (1998).
42. K. Kawasaki, et al., Isolation of a Chinese hamster ovary (CHO) cDNA encoding phosphatidylglycerophosphate (PGP) synthase, expression of which corrects the mitochondrial abnormalities of a PGP synthase-defective mutant of CHO-K1 cells. J. Biol. Chem. 274, 1828–1834 (1999).
43. C. Osman, M. Haag, F. T. Wieland, B. Brügger, T. Langer, A mitochondrial phosphatase required for cardiolipin biosynthesis: The PGP phosphatase Gep4. EMBO J. 29, 1976–1987 (2010).
44. J. Zhang, et al., Mitochondrial phosphatase PTPMT1 is essential for cardiolipin biosynthesis. Cell Metab. 13, 690–700 (2011).
45. M. Schlame, D. Haldar, Cardiolipin Is Synthesized on the Matrix Side of the Inner Membrane in Rat Liver Mitochondria. J. Biol. Chem. 268, 74–79 (1993).
46. M. Schlame, K. Y. Hostetler, Cardiolipin synthase from mammalian mitochondria. Biochim. Biophys. Acta - Lipids Lipid Metab. 1348, 207–213 (1997).
47. S. Chang, P. N. Heacock, E. Mileykovskaya, D. R. Voelker, W. Dowhan, Isolation and Characterization of the Gene (CLS1) Encoding Cardiolipin Synthase in Saccharomyces cerevisiae * have cloned the gene (CLS1) encoding CL synthase in. J. Biol. Chem. 273, 14933–14941 (1998).
48. R. H. Houtkooper, et al., Identification and characterization of human cardiolipin synthase. FEBS Lett. 580, 3059–3064 (2006).
49. K. Y. Hostetler, J. M. Galesloot, P. Boer, H. Van Den Bosch, Further studies on the formation of cardiolipin and phosphatidylglycerol in rat liver mitochondria. Effect of divalent cations and the fatty acid composition of CDP-diglyceride. Biochim. Biophys. Acta 380, 382–389 (1975).
50. A. Beranek, et al., Identification of a cardiolipin-specific phospholipase encoded by the gene CLD1 (YGR110W) in yeast. J. Biol. Chem. 284, 11572–11578 (2009).
51. M. G. Baile, K. Whited, S. M. Claypool, Deacylation on the matrix side of the mitochondrial inner membrane regulates cardiolipin remodeling. Mol. Biol. Cell 24, 2008–2020 (2013).
52. A. Malhotra, et al., Role of calcium-independent phospholipase A2 in the pathogenesis of Barth syndrome. Proc. Natl. Acad. Sci. 106, 2337–2341 (2009).
53. Y. H. Hsu, D. S. Dumlao, J. Cao, E. A. Dennis, Assessing Phospholipase A2 Activity toward Cardiolipin by Mass Spectrometry. PLoS One 8 (2013).
54. W. A. Taylor, G. M. Hatch, Purification and characterization of monolysocardiolipin acyltransferase from pig liver mitochondria. J. Biol. Chem. 278, 12716–12721 (2003).
55. J. Cao, Y. Liu, J. Lockwood, P. Burn, Y. Shi, A novel cardiolipin-remodeling pathway revealed by a gene encoding an endoplasmic reticulum-associated acyl-CoA:lysocardiolipin acyltransferase (ALCAT1) in mouse. J. Biol. Chem. 279, 31727–31734 (2004).

56. A. Malhotra, Y. Xu, M. Ren, M. Schlame, Formation of molecular species of mitochondrial cardiolipin. 1. A novel transacylation mechanism to shuttle fatty acids between sn-1 and sn-2 positions of multiple phospholipid species. Biochim. Biophys. Acta 1791, 314–320 (2009).
57. W. A. Taylor, G. M. Hatch, Identification of the human mitochondrial linoleoyl-coenzyme a monolysocardiolipin acyltransferase (MLCL AT-1). J. Biol. Chem. 284, 30360–30371 (2009).
58. J. Li, et al., Cardiolipin Remodeling by ALCAT1 Links Oxidative Stress and Mitochondrial Dysfunction to Obesity. Cell Metab. 12, 154–165 (2011).
59. M. Schlame, et al., Deficiency of TetralinoleoylCardiolipin in Barth Syndrome. Ann. Neurol. 51, 634–637 (2002).
60. F. Valianpour, R. J. A. Wanders, P. G. Barth, H. Overmars, A. H. Van Gennip, Quantitative and compositional study of cardiolipin in platelets by electrospray ionization mass spectrometry: Application for the identification of Barth syndrome patients. Clin. Chem. 48, 1390–1397 (2002).
61. F. F. Hsu, et al., Structural characterization of cardiolipin by tandem quadrupole and multiple-stage quadrupole ion-trap mass spectrometry with electrospray ionization. J. Am. Soc. Mass Spectrom. 16, 491–504 (2005).
62. X. Han, K. Yang, J. Yang, H. Cheng, R. W. Gross, Shotgun lipidomics of cardiolipin molecular species in lipid extracts of biological samples. J. Lipid Res. 47, 864–879 (2006).
63. M. Schlame, et al., The physical state of lipid substrates provides transacylation specificity for tafazzin. Nat. Chem. Biol. 8, 862–869 (2012).
64. L. D. Renner, D. B. Weibel, Cardiolipin microdomains localize to negatively curved regions of Escherichia coli membranes. Proc. Natl. Acad. Sci. 108, 6264–6269 (2011).
65. R. M. Epand, K. D'Souza, B. Berno, M. Schlame, Membrane curvature modulation of protein activity determined by NMR. Biochim. Biophys. Acta - Biomembr. 1848, 220–228 (2015).
66. M. Abe, et al., Mechanism for remodeling of the acyl chain composition of cardiolipin catalyzed by Saccharomyces cerevisiae tafazzin. J. Biol. Chem. 291, 15491–15502 (2016).
67. M. G. Baile, et al., Unremodeled and remodeled cardiolipin are functionally indistinguishable in yeast. J. Biol. Chem. 289, 1768–1778 (2014).
68. Y. Y. Tyurina, et al., Lipidomics characterization of biosynthetic and remodeling pathways of cardiolipins in genetically and nutritionally manipulated yeast cells. ACS Chem. Biol. 12, 265–281 (2017).
69. M. Aoun, et al., Dietary fatty acids modulate liver mitochondrial cardiolipin content and its fatty acid composition in rats with non alcoholic fatty liver disease. J. Bioenerg. Biomembr. 44, 439–452 (2012).
70. E. M. Sullivan, et al., Murine diet-induced obesity remodels cardiac and liver mitochondrial phospholipid acyl chains with differential effects on respiratory enzyme activity. J. Nutr. Biochem. 45, 94–103 (2017).
71. S. M. Claypool, K. Whited, S. Srijumnong, X. Han, C. M. Koehler, Barth syndrome mutations that cause tafazzin complex lability. J. Cell Biol. 192, 447–462 (2011).
72. K. Whited, M. G. Baile, P. Currier, S. M. Claypool, Seven functional classes of barth syndrome mutation. Hum. Mol. Genet. 22, 483–492 (2013).
73. A. Bowron, et al., Barth syndrome without tetralinoleoyl cardiolipin deficiency: a possible ameliorated phenotype. J. Inherit. Metab. Dis. 38, 279–86 (2015).
74. Y. Fan, et al., A Novel Exonic Splicing Mutation in the TAZ (G4.5) Gene in a Case with Atypical Barth Syndrome. JIMD Rep. 11, 99–106 (2013).
75. J. Planas-Iglesias, et al., Cardiolipin Interactions with Proteins. Biophys. J. 109, 1282–1294 (2015).
76. D. Acehan, Y. Xu, D. L. Stokes, M. Schlame, Comparison of lymphoblast mitochondria from normal subjects and patients with Barth syndrome using electron microscopic tomography. Lab. Investig. 87, 40–48 (2007).
77. D. Acehan, et al., Cardiac and skeletal muscle defects in a mouse model of human Barth syndrome. J. Biol. Chem. 286, 899–908 (2011).
78. C. K. L. Phoon, et al., Tafazzin Knockdown in Mice Leads to a Developmental Cardiomyopathy With Early Diastolic Dysfunction Preceding Myocardial Noncompaction. J. Am. Heart Assoc. 1, jah3-e000455-jah3-e000455 (2012).
79. M. Fry, D. E. Green, Cardiolipin Requirement for Electron Transfer in Complex I and IT1 of the Mitochondrial Respiratory Chain*. J. Biol. Chem. Val 256, 1874–1880 (1981).

80. G. Paradies, G. Petrosillo, M. Pistolese, F. M. Ruggiero, Reactive oxygen species affect mitochondrial electron transport complex I activity through oxidative cardiolipin damage. Gene 286, 135–141 (2002).
81. B. Gomez, N. C. Robinson, Phospholipase digestion of bound cardiolipin reversibly inactivates bovine cytochrome bc1. Biochemistry 38, 9031–9038 (1999).
82. T. Wenz, et al., Role of phospholipids in respiratory cytochrome bc1 complex catalysis and supercomplex formation. Biochim. Biophys. Acta - Bioenerg. 1787, 609–616 (2009).
83. E. Sedlák, R. Varhač, A. Musatov, N. C. Robinson, The Kinetic Stability of Cytochrome c Oxidase: Effect of Bound Phospholipid and Dimerization. Biophys. J. 107, 2941–2949 (2014).
84. E. Sedlák, N. C. Robinson, Destabilization of the Quaternary Structure of Bovine Heart Cytochrome c Oxidase upon Removal of Tightly Bound Cardiolipin. Biochemistry 54, 5569–5577 (2015).
85. K. Pfeiffer, et al., Cardiolipin Stabilizes Respiratory Chain Supercomplexes. J. Biol. Chem. 278, 52873–52880 (2003).
86. M. Zhang, E. Mileykovskaya, W. Dowhan, Gluing the respiratory chain together: Cardiolipin is required for supercomplex formation in the inner mitochondrial membrane. J. Biol. Chem. 277, 43553–43556 (2002).
87. C. T. Schwall, V. L. Greenwood, N. N. Alder, The stability and activity of respiratory Complex II is cardiolipin-dependent. Biochim. Biophys. Acta - Bioenerg. 1817, 1588–1596 (2012).
88. T. H. Haines, N. A. Dencher, Cardiolipin: A proton trap for oxidative phosphorylation. FEBS Lett. 528, 35–39 (2002).
89. S. M. Claypool, P. Boontheung, J. M. McCaffery, J. A. Loo, C. M. Koehler, The Cardiolipin Transacylase, Tafazzin, Associates with Two Distinct Respiratory Components Providing Insight into Barth Syndrome. Mol. Biol. Cell 19, 5143–5155 (2008).
90. S. M. Claypool, Cardiolipin, a critical determinant of mitochondrial carrier protein assembly and function. Biochim. Biophys. Acta 1788, 2059–2068 (2009).
91. A. Musatov, E. Sedlák, Role of cardiolipin in stability of integral membrane proteins. Biochimie 142, 102–111 (2017).
92. F. Jiang, et al., Absence of cardiolipin in the crd1 null mutant results in decreased mitochondrial membrane potential and reduced mitochondrial function. J. Biol. Chem. 275, 22387–22394 (2000).
93. N. Gebert, et al., Mitochondrial cardiolipin involved in outer membrane protein biogenesis: implications for Barth syndrome. Curr. Biol. 19, 2133–2139 (2009).
94. T. Ban, H. Kohno, T. Ishihara, N. Ishihara, Relationship between OPA1 and cardiolipin in mitochondrial inner-membrane fusion. Biochim. Biophys. Acta - Bioenerg. 1859, 951–957 (2018).
95. I. Bustillo-Zabalbeitia, et al., Specific interaction with cardiolipin triggers functional activation of dynamin-related protein 1. PLoS One 9 (2014).
96. A. J. Chicco, G. C. Sparagna, Role of cardiolipin alterations in mitochondrial dysfunction and disease. AJP Cell Physiol. 292, C33–C44 (2006).
97. R. H. Houtkooper, F. M. Vaz, Cardiolipin, the heart of mitochondrial metabolism. Cell. Mol. Life Sci. 65, 2493–2506 (2008).
98. R. N. A. H. Lewis, R. N. McElhaney, The physicochemical properties of cardiolipin bilayers and cardiolipin-containing lipid membranes. Biochim. Biophys. Acta - Biomembr. 1788, 2069–2079 (2009).
99. M. Klingenberg, Cardiolipin and mitochondrial carriers. Biochim. Biophys. Acta - Biomembr. 1788, 2048–2058 (2009).
100. S. M. Claypool, C. M. Koehler, The complexity of cardiolipin in health and disease. Trends Biochem. Sci. 37, 32–41 (2012).
101. G. Paradies, V. Paradies, F. M. Ruggiero, G. Petrosillo, Cardiolipin and Mitochondrial Function in Health and Disease. Antioxid. Redox Signal. 20, 1925–1953 (2014).
102. X. X. Li, B. Tsoi, Y. F. Li, H. Kurihara, R. R. He, Cardiolipin and Its Different Properties in Mitophagy and Apoptosis. J. Histochem. Cytochem. 63, 301–311 (2015).
103. N. Ikon, R. O. Ryan, Cardiolipin and mitochondrial cristae organization. Biochim. Biophys. Acta 1859, 1156–1163 (2017).

104. C. T. Chu, et al., Cardiolipin externalization to the outer mitochondrial membrane acts as an elimination signal for mitophagy in neuronal cells. Nat. Cell Biol. 15, 1197–1205 (2013).
105. F. Gonzalvez, et al., Cardiolipin provides an essential activating platform for caspase-8 on mitochondria. J. Cell Biol. 183, 681–696 (2008).
106. V. E. Kagan, et al., Cardiolipin Signaling Mechanisms: Collapse of Asymmetry and Oxidation. Antioxid. Redox Signal. 22, 1667–1680 (2015).
107. K. Balasubramanian, et al., Dichotomous roles for externalized cardiolipin in extracellular signaling: Promotion of phagocytosis and attenuation of innate immunity. Sci. Signal. 8 (2015).
108. A. Broder, J. J. Chan, C. Putterman, Dendritic cells: An important link between antiphospholipid antibodies, endothelial dysfunction, and atherosclerosis in autoimmune and non-autoimmune diseases. Clin. Immunol. 146, 197–206 (2013).
109. C. Alessandri, F. Conti, M. Pendolino, R. Mancini, G. Valesini, New autoantigens in the antiphospholipid syndrome. Autoimmun. Rev. 10, 609–616 (2011).
110. R. Zhou, A. S. Yazdi, P. Menu, J. Tschopp, A role for mitochondria in NLRP3 inflammasome activation. Nature 469, 221–226 (2011).
111. S. S. Iyer, et al., Mitochondrial cardiolipin is required for Nlrp3 inflammasome activation. Immunity 39, 311–323 (2013).
112. J. J. Maguire, et al., Known Unknowns of Cardiolipin Signaling: The Best Is Yet To Come. Biochim. Biophys. Acta 1862, 8–24 (2017).
113. V. E. Kagan, et al., Elimination of the Unnecessary: Intra- and Extracellular Signaling by Anionic Phospholipids. Biochem. Biophys. Res. Commun. 482, 482–490 (2017).
114. J. Dudek, Role of Cardiolipin in Mitochondrial Signaling Pathways. Front. Cell Dev. Biol. 5, 1–17 (2017).
115. M. D. Lynes, et al., Cold-Activated Lipid Dynamics in Adipose Tissue Highlights a Role for Cardiolipin in Thermogenic Metabolism. Cell Rep. 24, 781–790 (2018).
116. E. G. Sustarsic, et al., Cardiolipin Synthesis in Brown and Beige Fat Mitochondria Is Essential for Systemic Energy Homeostasis. Cell Metab. 28, 159-174.e11 (2018).
117. T. Hoang, M. D. Smith, M. Jelokhani-Niaraki, Expression, folding, and proton transport activity of human uncoupling protein-1 (ucp1) in lipid membranes. J. Biol. Chem. 288, 36244–36258 (2013).
118. G. Paradies, V. Paradies, V. De Benedictis, F. M. Ruggiero, G. Petrosillo, Functional role of cardiolipin in mitochondrial bioenergetics. Biochim. Biophys. Acta - Bioenerg. 1837, 408–417 (2014).
119. Y. Sandlers, et al., Metabolomics Reveals New Mechanisms for Pathogenesis in Barth Syndrome and Introduces Novel Roles for Cardiolipin in Cellular Function. PLoS One 11 (2016).
120. Y. Shi, Emerging roles of cardiolipin remodeling in mitochondrial dysfunction associated with diabetes, obesity, and cardiovascular diseases. J. Biomed. Res. 24, 6–15 (2010).
121. G. Paradies, G. Petrosillo, V. Paradies, F. M. Ruggiero, Oxidative stress, mitochondrial bioenergetics, and cardiolipin in aging. Free Radic. Biol. Med. 48, 1286–1295 (2010).
122. H. K. Saini-Chohan, et al., Cardiolipin biosynthesis and remodeling enzymes are altered during development of heart failure. J. Lipid Res. 50, 1600–1608 (2009).
123. E. J. Lesnefsky, P. Minkler, C. L. Hoppel, Enhanced modification of cardiolipin during ischemia in the aged heart. J. Mol. Cell. Cardiol. 46, 1008–1015 (2009).
124. G. Paradies, G. Petrosillo, V. Paradies, F. M. Ruggiero, Mitochondrial dysfunction in brain aging: Role of oxidative stress and cardiolipin. Neurochem. Int. 58, 447–457 (2011).
125. E. J. Lesnefsky, Q. Chen, C. L. Hoppel, Mitochondrial Metabolism in Aging Heart. Circ. Res. 118, 1593–1611 (2016).
126. V. F. Monteiro-Cardoso, et al., Cardiolipin profile changes are associated to the early synaptic mitochondrial dysfunction in Alzheimer's disease. J. Alzheimer's Dis. 43, 1375–1392 (2015).
127. S. Ghio, F. Kamp, R. Cauchi, A. Giese, N. Vassallo, Interaction of α-synuclein with biomembranes in Parkinson's disease - Role of cardiolipin. Prog. Lipid Res. 61, 73–82 (2016).
128. T. Ryan, et al., Cardiolipin exposure on the outer mitochondrial membrane modulates α-synuclein. Nat. Commun. 9 (2018).
129. J. C. Martens, et al., Lipidomic analysis of molecular cardiolipin species in livers exposed to ischemia/reperfusion. Mol. Cell. Biochem. 400, 253–263 (2014).
130. J. Ji, et al., Deciphering of mitochondrial cardiolipin oxidative signaling in cerebral ischemia-reperfusion. J. Cereb. Blood Flow Metab. 35, 319–328 (2015).

131. G. Paradies, V. Paradies, F. M. Ruggiero, G. Petrosillo, Mitochondrial bioenergetics and cardiolipin alterations in myocardial ischemia/reperfusion injury. Implications for pharmacological cardioprotection. Am. J. Physiol. Circ. Physiol., ajpheart.00028.2018 (2018).
132. Q. He, X. Han, Cardiolipin remodeling in diabetic heart. Chem. Phys. Lipids 179, 75–81 (2014).
133. X. Han, et al., Alterations in myocardial cardiolipin content and composition occur at the very earliest stages of diabetes: A shotgun lipidomics study. Biochemistry 46, 6417–28 (2007).
134. T. L. Croston, et al., Evaluation of the cardiolipin biosynthetic pathway and its interactions in the diabetic heart. Life Sci. 93, 313–22 (2013).
135. L. K. Cole, et al., Impaired cardiolipin biosynthesis prevents hepatic steatosis and diet-induced obesity. Diabetes 65, 3289–3300 (2016).
136. G. Paradies, V. Paradies, F. M. Ruggiero, G. Petrosillo, Oxidative stress, cardiolipin and mitochondrial dysfunction in nonalcoholic fatty liver disease. World J. Gastroenterol. 20, 14205–14218 (2014).
137. Z. Younossi, et al., Global burden of NAFLD and NASH: Trends, predictions, risk factors and prevention. Nat. Rev. Gastroenterol. Hepatol. 15, 11–20 (2018).
138. G. Petrosillo, et al., Mitochondrial dysfunction in rat with nonalcoholic fatty liver. Involvement of complex I, reactive oxygen species and cardiolipin. Biochim. Biophys. Acta - Bioenerg. 1767, 1260–1267 (2007).
139. T. Hayasaka, H. Fuda, S.-P. Hui, H. Chiba, Imaging Mass Spectrometry Reveals a Decrease of Cardiolipin in the Kidney of NASH Model Mice. Anal. Sci. 32, 473–476 (2016).
140. M. Chen, Y. Zhang, P. S. Zheng, Tafazzin (TAZ) promotes the tumorigenicity of cervical cancer cells and inhibits apoptosis. PLoS One 12, 1–13 (2017).
141. M. A. Kiebish, X. Han, H. Cheng, J. H. Chuang, T. N. Seyfried, Cardiolipin and electron transport chain abnormalities in mouse brain tumor mitochondria: lipidomic evidence supporting the Warburg theory of cancer. J. Lipid Res. 49, 2545–2556 (2008).
142. Z. Gu, et al., Aberrant cardiolipin metabolism in the yeast taz1 mutant: A model for Barth syndrome. Mol. Microbiol. 51, 149–158 (2004).
143. L. Ma, F. M. Vaz, Z. Gu, R. J. A. Wanders, M. L. Greenberg, The human TAZ gene complements mitochondrial dysfunction in the yeast taz1Δ mutant: Implications for Barth syndrome. J. Biol. Chem. 279, 44394–44399 (2004).
144. M. G. Baile, S. M. Claypool, The power of yeast to model diseases of the powerhouse of the cell. Front. Biosci. (Landmark Ed. 18, 241–78 (2013).
145. A. Saric, K. Andreau, A. S. Armand, I. M. Møller, P. X. Petit, Barth syndrome: From mitochondrial dysfunctions associated with aberrant production of reactive oxygen species to pluripotent stem cell studies. Front. Genet. 6, 359 (2016).
146. K. Brandner, et al., Taz1, an outer mitochondrial membrane protein, affects stability and assembly of inner membrane protein complexes: implications for Barth Syndrome. Mol. Biol. Cell 16, 5202–5214 (2005).
147. S. Chen, Q. He, M. L. Greenberg, Loss of tafazzin in yeast leads to increased oxidative stress during respiratory growth. Mol. Microbiol. 68, 1061–1072 (2008).
148. A. S. Joshi, J. Zhou, V. M. Gohil, S. Chen, M. L. Greenberg, Cellular functions of cardiolipin in yeast. Biochim. Biophys. Acta - Mol. Cell Res. 1793, 212–218 (2009).
149. G. J. Gaspard, C. R. McMaster, The mitochondrial quality control protein Yme1 is necessary to prevent defective mitophagy in a yeast model of Barth syndrome. J. Biol. Chem. 290, 9284–9298 (2015).
150. Y. Xu, et al., A Drosophila model of Barth syndrome. Proc. Natl. Acad. Sci. U. S. A. 103, 11584–11588 (2006).
151. Z. Khuchua, Z. Yue, L. Batts, A. W. Strauss, A zebrafish model of human barth syndrome reveals the essential role of tafazzin in cardiac development and function. Circ. Res. 99, 201–8 (2006).
152. D. Damschroder, C. Reynolds, R. Wessells, Drosophila tafazzin mutants have impaired exercise capacity. Physiol. Rep. 6, e13604 (2018).
153. P. G. Barth, et al., X-linked cardioskeletal myopathy and neutropenia (Barth syndrome): Respiratory-chain abnormalities in cultured fibroblasts. J. Inherit. Metab. Dis. 19, 157–60 (1996).
154. T. W. Kuijpers, et al., Neutrophils in Barth syndrome (BTHS) avidly bind annexin-V in the absence of apoptosis. Blood 103, 3915–23 (2004).

155. J. Dudek, et al., Cardiolipin deficiency affects respiratory chain function and organization in an induced pluripotent stem cell model of Barth syndrome. Stem Cell Res. 11, 806–19 (2013).
156. G. Wang, et al., Modeling the mitochondrial cardiomyopathy of Barth syndrome with induced pluripotent stem cell and heart-on-chip technologies. Nat. Med. 20, 616–23 (2014).
157. W. Lou, et al., Loss of tafazzin results in decreased myoblast differentiation in C2C12 cells: A myoblast model of Barth syndrome and cardiolipin deficiency. Biochim. Biophys. Acta - Mol. Cell Biol. Lipids 1863, 857–865 (2018).
158. V. Makaryan, et al., The cellular and molecular mechanisms for neutropenia in Barth syndrome. Eur. J. Haematol. 88, 195–209 (2012).
159. D. Acehan, et al., Distinct effects of tafazzin deletion in differentiated and undifferentiated mitochondria. Mitochondrion 9, 86–95 (2009).
160. Q. He, N. Harris, J. Ren, X. Han, Mitochondria-targeted antioxidant prevents cardiac dysfunction induced by tafazzin gene knockdown in cardiac myocytes. Oxid. Med. Cell. Longev., 654198 (2014).
161. A. A. Dinca, W. M. Chien, M. T. Chin, Identification of novel mitochondrial localization signals in human Tafazzin, the cause of the inherited cardiomyopathic disorder Barth syndrome. J. Mol. Cell. Cardiol. 114, 83–92 (2018).
162. F. Valianpour, et al., Linoleic acid supplemention of Barth syndrome fibroblasts restores cardiolipin levels. J. Lipid Res. 44, 560–566 (2003).
163. N. Ikon, B. Su, F. F. Hsu, T. M. Forte, R. O. Ryan, Exogenous cardiolipin localizes to mitochondria and prevents TAZ knockdown-induced apoptosis in myeloid progenitor cells. Biochem. Biophys. Res. Commun. 464, 580–5 (2015).
164. N. Ikon, F. Hsu, J. Shearer, T. M. Forte, R. O. Ryan, Evaluation of cardiolipin nanodisks as lipid replacement therapy for Barth syndrome. 32, 107–112 (2018).
165. W. B. Ball, et al., Ethanolamine ameliorates mitochondrial dysfunction in cardiolipin-deficient yeast cells. J. Biol. Chem. 293, 10870–10883 (2018).
166. S. Suzuki-Hatano, et al., AAV-Mediated TAZ Gene Replacement Restores Mitochondrial and Cardioskeletal Function in Barth Syndrome. Hum. Gene Ther. (2018) https:/doi.org/10.1089/hum.2018.020.
167. A Trial to Evaluate Safety, Tolerability and Efficacy of Elamipretide in Subjects With Barth Syndrome (TAZPOWER).
168. K. Zhao, et al., Cell-permeable peptide antioxidants targeted to inner mitochondrial membrane inhibit mitochondrial swelling, oxidative cell death, and reperfusion injury. J. Biol. Chem. 279, 34682–34690 (2004).
169. A. V. Birk, et al., The Mitochondrial-Targeted Compound SS-31 Re-Energizes Ischemic Mitochondria by Interacting with Cardiolipin. J. Am. Soc. Nephrol. 24, 1250–61 (2013).
170. S. Liu, Y. Soong, S. V. Seshan, H. H. Szeto, Novel cardiolipin therapeutic protects endothelial mitochondria during renal ischemia and mitigates microvascular rarefaction, inflammation, and fibrosis. AJP Ren. Physiol. 306, F970-80 (2014).
171. A. V. Birk, W. M. Chao, C. Bracken, J. D. Warren, H. H. Szeto, Targeting mitochondrial cardiolipin and the cytochrome c/cardiolipin complex to promote electron transport and optimize mitochondrial ATP synthesis. Br. J. Pharmacol. 171, 2017–2028 (2014).
172. H. H. Szeto, First-in-class cardiolipin-protective compound as a therapeutic agent to restore mitochondrial bioenergetics. Br. J. Pharmacol. 171, 2029–50 (2014).

1.3 Identifying novel pathways of interest in mitochondrial disorders

Methylmalonic acidemia (MMA), propionic acidemia (PA), and Barth syndrome (BTHS), are three genetic disorders of mitochondrial intermediary metabolism where the primary

genetic defects are well-established, yet knowledge of the downstream cellular effects are limited. Investigating these downstream mechanisms of cellular pathogenesis has the potential to provide novel targets for disease monitoring and treatment.

To investigate the diverse cellular effects that result from the primary metabolic defects in MMA, PA, and BTHS, we performed hypotheses generating multi-omics investigations in both patient and novel CRISPR/Cas9 edited cellular models. “Omics”, branches of investigation that end in the suffix -omics such as genomics, proteomics, metabolomics, is the collective characterization and quantification of pool of biological molecules that translate into structure, function, and dynamics. The two branches of omics harnessed in our investigations were proteomics and metabolomics.

Proteomics is the study of the proteome, the entire protein complement of the genome. [1–3] Contrary to the previously suggested and accepted one gene, one protein maxim, research has made it increasingly obvious that the proteome is as complex as genetic variation. The proteome consists of all the proteins present in a cell or individual, such as proteins that result from direct translation of the genetic code or those that result after alternative splicing and extensive post-translational modification. Since proteins are the executors of the prescribed genetic code, they are thereby responsible for or involved in almost every cellular function or regulatory mechanism. Therefore, the proteome is responsible for the phenotype of the cell and ultimately that of the entire individual. Like the genome, the proteome can be altered by disease states, including by changes in protein expression, modification, or processing. Proteomics is specifically aimed at identifying and characterizing these protein changes that occur as a result of disease state or chronic stress. [1–3]

Metabolomics is the study of the metabolome, the complete collection of metabolites or small molecule chemical such as amino acids or organic acids. [4, 5] Like the genome and proteome, which can be altered by disease, the metabolome of is sensitive to internal and external variables such as genetics, age, gender, and diet. [4, 5] More importantly, a single gene defect as in IEMs, can lead to a 10,000-fold change in a single endogenous metabolite levels, with far-reaching downstream metabolite perturbations. [4]

Using the data generated from untargeted quantitative proteomics and metabolomics to perform functional analyses and annotation, we aimed to unveil novel pathways perturbed by disease. By identifying novel pathways of interest and expanding our knowledge of the downstream cellular effect of the single gene defect, we can ultimately identify new targets for therapy and clinical monitoring in MMA, PA, and BTHS, three IEMs with a significant burden of morbidity and mortality.

1.3.1 References

1. A. F. M. Altelaar, J. Munoz, A. J. R. Heck, Next-generation proteomics: Towards an integrative view of proteome dynamics. Nat. Rev. Genet. 14, 35–48 (2013).
2. C. Monti, M. Zilocchi, I. Colugnat, T. Alberio, Proteomics turns functional. J. Proteomics 198, 36–44 (2019).
3. B. Aslam, M. Basit, M. A. Nisar, M. Khurshid, M. H. Rasool, Proteomics: Technologies and their applications. J. Chromatogr. Sci. 55, 182–196 (2017).
4. D. S. Wishart, Metabolomics for investigating physiological and pathophysiological processes. Physiol. Rev. 99, 1819–1875 (2019).
5. A. C. Schrimpe-Rutledge, S. G. Codreanu, S. D. Sherrod, J. A. McLean, Untargeted Metabolomics Strategies—Challenges and Emerging Directions. J. Am. Soc. Mass Spectrom. 27, 1897–1905 (2016).

Chapter 2

Multi-omics studies in cellular models of methylmalonic acidemia and propionic acidemia reveal dysregulation of serine metabolism

This original article has been published and was reprinted with permission: Anzmann AF, Pinto S, Busa V, Carlson J, McRitchie S, Sumner S, Pandey A, Vernon HJ (2019) Multi-omics studies in cellular models of methylmalonic acidemia and propionic acidemia reveal dysregulation of serine metabolism. *Biochimica Biophysica Acta Molecular Basis of Disease* 1865(12):165538.

2.1 Abstract

Background: Methylmalonic acidemia (MMA) and propionic acidemia (PA) are related disorders of mitochondrial propionate metabolism, caused by defects in methylmalonyl-CoA mutase (MUT) and propionyl-CoA carboxylase (PCC), respectively. These biochemical defects lead to a complex cascade of downstream metabolic abnormalities, and identification of these abnormal pathways has important implications for understanding disease pathophysiology. Using a multi-omics approach in cellular models of MMA and PA, we identified serine and thiol metabolism as important areas of metabolic dysregulation.

Methods: We performed global proteomic analysis of fibroblasts and untargeted metabolomics analysis of plasma from individuals with MMA to identify novel pathways of dysfunction. We probed these novel pathways in CRISPR-edited, MUT and PCCA null HEK293 cell lines via targeted metabolomics, gene expression analysis, and flux metabolomics tracing utilization of 13C-glucose.

Results: Proteomic analysis of fibroblasts identified upregulation of multiple proteins involved in serine synthesis and thiol metabolism including: phosphoserine amino transferase (PSAT1), cystathionine beta synthase (CBS), and mercaptopyruvate sulfurtransferase (MPST). Metabolomics analysis of plasma revealed significantly increased levels of cystathionine and glutathione, central metabolites in thiol metabolism. CRISPR-edited MUT and PCCA HEK293 cells recapitulate primary defects of MMA and PA and have upregulation of transcripts associated with serine and thiol metabolism including PSAT1. 13C-glucose flux metabolomics in MUT and PCCA null HEK293 cells identified increases in serine de novo biosynthesis, serine transport, and abnormal downstream TCA cycle utilization.

Conclusion: We identified abnormal serine metabolism as a novel area of cellular dysfunction in MMA and PA, thus introducing a potential new target for therapeutic investigation.

2.2 Introduction

Serine is a non-essential amino acid that can be synthesized de novo from glucose via 3-phosphoglycerate, a glycolytic and gluconeogenic intermediate. Serine has multiple critical

roles in the synthesis of fundamental cellular metabolites including phosphatidylcholine, creatine, one-carbon metabolites, and S-adenosylmethionine, the key methyl donor in cells [1].

Recently, alterations in serine metabolism have been described in several models of mitochondrial disease including the Deletor mouse model of mtDNA deletions, as well as in affected humans with POLGassociated disease, Myoclonic epilepsy with ragged red fibers (MERRF) and Mitochondrial encephalomyopathy, lactic acidosis, and stroke-like episodes (MELAS) [2–4]. Evidence points towards redirected flux towards one carbon metabolism and glutathione as a protective mechanism for managing mitochondrial bioenergetic stress. Interestingly, similar changes have also been reported in multiple studies of various forms of malignancy [5–8], suggesting that serine metabolism represents a central response to diverse forms of mitochondrial metabolic challenges. In this study, we explored the role of serine metabolism in propionic acidemia (PA) and methylmalonic acidemia (MMA).

PA and MMA are closely related autosomal recessive disorders of isoleucine and valine metabolism and result in defective entry of propiogenic metabolites into the TCA cycle at the level of succinyl CoA [9,10]. PA is caused by genetic defects in propionyl CoA carboxylase (encoded by PCCA and PCCB). MMA is caused by genetic defects in methylmalonyl-CoA mutase (encoded by MUT), or in vitamin B12 metabolism, among other rarer causes [10–13]. There is a strong clinical overlap between these disorders, but also important phenotypic differences [9,14–16]. In both disorders, there are multiple layers of evidence for mitochondrial dysfunction and oxidative stress [17–19].

We used global proteomic analysis to identify novel pathways of cellular dysfunction in fibroblasts from individuals with PA and MMA. In both disorders, we uncovered enrichment of proteins involved in serine biosynthesis and thiol metabolism. We next employed untargeted metabolomics to evaluate the plasma of individuals with PA and MMA and identified increased excretion of key metabolites associated with serine metabolism, cystathionine and glutathione.

In order to obtain further mechanistic insight into disturbances of serine metabolism in PA and MMA, we developed CRISPR/Cas9 edited PCCA-null and MUT-null HEK293 cell lines, which showed increased expression of genes associated with serine metabolism, notably phosphoserine amino transferase (PSAT). Finally, we employed flux metabolomics and showed significant increases in de novo serine metabolism in these cells.

2.3 Methods

Fibroblast cell culture

Primary fibroblast lines were derived from unrelated individuals with mut0 MMA (n = 2), PA (n = 2), and healthy controls (n = 2). Patient fibroblast experiments and the collection of clinical history had institutional IRB approval via Johns Hopkins University protocols NA_00026986 and NA_00036487. Individuals were diagnosed with MMA via lack of MUT enzyme activity in fibroblasts, the molecular confirmation of two pathological variants in MUT, and a clinical history of diagnostic urine organic acid analysis that includes massive elevations of methylmalonic acid. Individuals were diagnosed with PA via lack of functional PCC enzyme activity in fibroblasts, the molecular confirmation of

two pathological variants in PCCA, and a clinical history of diagnostic urine organic acid analysis that includes massive elevations of propionylglycine, methylcitrate, and tiglyglycine. Additionally, all 4 individuals, with MMA or PA, had a clinical history consistent with the infantile onset, severe form of the respective disease. The primary fibroblast cell lines were grown in RPMI 1640 medium (Gibco, Thermo Fisher Scientific) with 10% FBS (Gemini BioProducts) at 37 °C with 5% CO, unless otherwise noted. Control fibroblasts were obtained from healthy individuals without a known metabolic disorder.

Prior to harvesting, each primary fibroblast cell line (n = 2 for each condition) was grown to 70% confluence and then maintained in serum-free medium for 12 h. Cells were lysed and the protein concentration was estimated using BCA assay (Pierce). Sample processing for proteomics was performed based on modified filter aided sample preparation (FASP) protocol. 100 µg of protein lysate from each cell line was subjected to filtration using 30 kDa filters and 8 M urea to reduce the amount of SDS in the lysate. The reduced protein lysate was alkylated using 20 mM iodoacetamide (IAA) and incubated for 10 min in the dark at room temperature (RT). Prior to digestion, the concentration of urea was reduced to < 1 M using 50 mM Triethylammonium bicarbonate buffer (TEABC). Trypsin digestion was performed using 6-(1-tosylamido-2-phenyl) ethyl chloromethyl ketone (TPCK) treated trypsin (Promega) at an enzyme: substrate ratio of 1:20 for 12–16 h at 37 °C.

Global proteomics

Tandem mass tag (TMT) labeling and reversed phase liquid chromatography (RPLC) fractionation of proteins.

Digested peptide samples (n = 2 for each condition) were labeled using TMT 6-plex reagents as per manufacturer's instruction (Thermo Fischer Scientific). Briefly, peptide digests from each condition were reconstituted in 50 mM TEABC buffer and mixed with the TMT reagent and incubated at RT for 1 h. After incubation, the reaction was quenched by adding 5% hydroxylamine. The TMT-labeled samples were pooled at 1:1:1:1:1:1 ratio, evaporated to dryness and subjected to desalting using SepPak C18 cartridges. Peptides were fractionated by bRPLC [20]. Briefly, TMT-labeled and lyophilized peptide mixtures were resuspended in buffer A (10 mM TEABC) and fractionated by bRPLC chromatography on an Agilent 1100 LC system using a linear gradient of 8–60% buffer B (10 mM TEABC in 90% acetonitrile (ACN)) for 60 min at a flow rate of 1 mL/min. A total of 96 fractions were collected, concatenated to 12 fractions, vacuum dried and stored at −80 C until LC-MS/MS analysis.

LC-MS/MS analysis

TMT-labeled samples were analyzed on LTQ-Orbitrap Velos mass spectrometer (Thermo Fisher Scientific) interfaced with Proxeon Easy nLC system (Thermo Fisher Scientific). Each fraction was loaded and concentrated on a trap column (75 μm × 2 cm) packed in-house using C18 material (Magic C18AQ, 5 μm, 100 Å, Michrom Biosciences Inc.) with a flow rate of 3 μL/min and resolved on an analytical column (75 μm × 30 cm, Magic C18AQ, 5um, 100A, Michrom Biosciences Inc.) at a flow rate of 200 nl/min using a linear gradient of 5–30% ACN over 90 min. Precursor MS scan (m/z 350–1700) and MS/MS was acquired with a mass resolution of 60,000 and 30,000 at 400 m/z in orbitrap mass analyzer respectively. The top ten intense peaks were selected for MS/MS fragmentation in each scan and fragmented using higher-energy collision dissociation (HCD) mode with 45%

normalized collision energy. The isolation width was set to 1.9 m/z. Acquired ions selected in a given scan were selectively excluded for 30 s. The maximum ion accumulation time was set to 200 msec for MS and 300 msec for MS/MS scans. The lock mass option was enabled using polysiloxane ion (m/z, 445.120025) from ambient air for internal calibration.

Proteomic data analysis

Mass spectrometry-derived data were processed and quantified using Proteome Discoverer (Version 1.4) software suite (Thermo Fisher Scientific). The data were searched against NCBI Human RefSeq protein database (Release 59) containing common contaminants using Mascot (version 2.2.0) and Sequest search algorithms. The precursor mass tolerance was set to 10 ppm and the fragment mass tolerance was set to 0.05 Da. The search parameters included oxidation of methionine set as a dynamic modification, carbamidomethylation of cysteine (+57.0215 Da) and TMT tag (+229.1629 Da) at N-termini of peptides and lysine residues. A maximum of 2 missed cleavage were allowed for tryptic peptides. Identified peptides were validated using a Percolator algorithm with a q-value threshold of 0.01. The ratios were calculated by the quantitation node in proteome discoverer. Protein signals (as a proxy for quantity) were analyzed as log base 10 ratios of relative abundance between cell lines. Using the statistical program "R" for analysis, we confirmed that each result set showed a normal Gaussian distribution, (R Core Team (2013) [48]. R: A language and environment for statistical computing. R Foundation for Statistical Computing, Vienna, Austria. URL http://www.R-project.org/). In order to increase the specificity and avoid false positives, only proteins that were within two standard deviations of the mean within genotypes (MMA1 vs. MMA2, PA1 vs. PA2, WT1 vs. WT2) were considered for further analysis. Therefore, proteins which were highly discordant in

abundance within each genotype were discarded. Subsequently, in order to determine differentially expressed proteins in MMA and PA fibroblast cell lines, the ratios of protein abundance were analyzed as log base 10 ratios of relative abundance between disease groups (MMA vs. control, PA vs. control, MMA vs. PA). Proteins that were at least 2 standard deviations from the mean were assessed for functional annotation.

Functional annotation of differentially expressed proteins in fibroblasts

To appreciate the functional characteristics of the differentially expressed proteins, we employed the DAVID Bioinformatics Resource v6.7 to determine the KEGG pathways and GO terms that are enriched proteins differentially expression in PA and MMA as compared to WT [21,22]. Pathways and GO terms were tested for significant enrichment via Fisher Exact test.

Untargeted metabolomics analysis

Metabolomics subjects

Fifty-two plasma samples were selected to identify discriminating biomarkers that correlate with PA and MMA. Samples included: 17 samples from individual with phenotypes consistent with the classical, neonatal onset form of PA (average age 10y 9.6 m; age range 4y 2 m to 25y 9.9 m), 15 samples from individuals with the classical mut0 type of MMA (average age 12y 3 m; age range 8 m to 31y 0m, and 20 sexmatched control samples (average age 9y 8.8 m; age range 7 m to 25y 6 m). Control samples were obtained from individuals who underwent routine laboratory testing and were not known to have a genetic or metabolic condition. All samples were acquired during a “well” outpatient visit to mitigate effects of intercurrent illness or metabolic decompensation. Patient plasma

experiments had institutional IRB approval via Johns Hopkins University protocol NA_00069372.

Metabolomics sample preparation and analysis

Sample preparation, data acquisition and analysis were performed as previously described [23–25]. Briefly, each of the fifty-two plasma samples were prepared by adding 400 µl cold methanol with tryptophan-d5 internal standard to 50 µl of plasma for protein precipitation. After centrifugation at 16,000 rcf, 350 µl of supernatant was lyophilized overnight and re-constituted in 100 µl of 95:5 water:methanol. In addition, phenotypic pooled samples were prepared by combining 30 µl from each of the study samples belonging to the same phenotype (MMA, PA, Control). In addition, total pools were created by taking a 250 µl aliquot from each of the phenotypic pools. Pooled plasma samples (phenotypic and total) were prepared identically to the individual study samples.

Samples were analyzed on a SYNAPT G2-Si QTOF mass spectrometer coupled to an Acquity UPLC (Waters Corporation, MA). Prior to analyzing the study samples, the column and the system were equilibrated with five injections of quality control samples. The compounds were separated on a Waters Acquity UPLC HSS T3 column (2.1 × 100 mm, 1.8 µm particle size) operating at 50 °C using a reversed-phase chromatographic method. A gradient mobile phase consisting of water with 0.1% formic acid (A) and methanol with 0.1% formic acid (B) were used. All MS data were collected over 50–1000 m/z in electrospray ionization (ESI) positive ion mode. Leucine enkephalin was used as the lock mass and a lock mass scan was collected every 45 s and averaged over 3 scans to perform correction for any mass drift over the course of the analytical run. Source and desolvation temperatures were set at 110 °C and 400 °C, respectively.

Metabolomics data processing

The raw mass spectrometric data was processed (alignment and peak picking) using Progenesis QI (Waters Corporation). The normalized data were mean centered and scaled by dividing by the standard deviation and multivariate analysis methods (principal component analysis (PCA), orthogonal partial least squares discriminant analysis (OPLS-DA)) were used to reduce the dimensionality and to visualize the study groups (SIMCA 14.1, MKS Umetrics, Umea, Sweden) [26,27]. The PCA scores plot was used to ensure that the quality control samples clustered in the center of the study samples from which they were derived, which has become a standard method for assessing the quality of untargeted metabolomics data. OPLS-DA, which is a supervised analysis method, was used to identify peaks important to differentiating the study groups. Loadings plots and variable influence on projection (VIP) plots were inspected. All models used a 7-fold cross-validation to assess the predictive variation of the model (Q2). Descriptive statistics and t-tests using the Satterthwaite approximation for unequal variances were conducted using SAS 9.4 (SAS Institute Inc., Cary, NC). In this exploratory study, p-values were not adjusted for multiple testing. Peaksthat had a VIP $\geq$ 2.0 with a jack-knife confidence interval that did not include 0 or had a p-value $<$ 0.001 were determined to be important for differentiating the study groups.

Putative identification of the signals differentiating the study groups was made using a database search against the ERCMRC's in-house exact-mass-retention-time library of standards and the Human Metabolome Database (HMDB). Peaks that could not be library-matched were classified as unknown.

MUT-null and PCCA-null CRISPR/Cas9 edited cells

Development of MUT-null and PCCA-null CRISPR/Cas9 edited HEK293 cells

Cas9-nickase with two adjacent guide RNAs (gRNAs) was used to make the null HEK293 cell lines as previously described [28]. MUT exon 5 and PCCA exon 12 were targeted for editing, based on the location of previously reported human disease-causing mutations [12,29]. gRNAs were designed using http://tools.genome-engineering.org (Supplementary Table 1) [30]. Synthesized gRNAs were inserted into a CR-BluntII-TOPO plasmid (Invitrogen) and transformed into E.coli. A plasmid co-expressing Cas9 and GFP (Addgene) was co-transfected with the gRNA-plasmids into WT HEK293 cells via lipofectamine. GFP positive single cells were FACS sorted into 96-well plates. Positive clones were identified by PCR and Sanger sequencing (Supplementary Table 2). For whole cell lysate extraction, confluent culture dishes were lysed with RIPA lysis buffer (1% (v/v) Triton X-100, 20 mm HEPES–KOH, pH 7.4, 50 mm NaCl, 1 mm EDTA, 2.5 mm MgCl2, 0.1% (w/v) SDS) spiked with 1 mm PMSF). Insoluble material was removed by centrifugation, the supernatant collected, and protein quantified using a BCA assay (Pierce). Absence of expressed PCCA (Novus Biologicals) or MUT (Abcam) protein was then confirmed in whole cell lysates via immunoblot of 3 individual cell passages for each genotype.

HEK293 cells were obtained from Thermo Fisher Scientific (Waltham, MA). Cells were cultured with DMEM (Corning Cellgro, ThermoFisher Scientific) supplemented with 10% FBS (Gemini BioProducts), and 1% L-glutamine (Gibco, Thermo Fisher Scientific), and grown at 37 °C with 5% CO, unless otherwise noted.

Metabolite measurements in HEK293 cells

Acylcarnitines were analyzed in spent media from confluent cell culture 6-wells at 4 days, 11 days and 18 days after cell plating via tandem mass spectrometry (MS/MS) without chromatographic separation in the positive-ion mode using multiple-reaction monitoring (MRM) as previously published [31,32]. Methylmalonate was quantified in spent media from confluent cell culture 6-wells at 4 days, 11 days and 18 days via stable-isotope dilution and gas chromatography/mass spectrometry (GC/MS) as previously published [33].

Metabolite measurements were performed with n = 3 (3 individual 6-well cell culture wells assayed of each genotype for each metabolite at all time points).

Gene expression in HEK293 cells

150,000 cells from each genotype (MUT-null, PCCA-null, and WT HEK293 cells) were plated in 6-well culture dishes. Following plating, gene expression was measured at day 1, 2, 4 and 8. SYBR green (BioRad) labeled reverse transcription-quantitative PCR (RT-qPCR) was carried out on cDNA derived from cells as previously described [34] for expression of the following genes: PSAT1, CBS, ASNS, SLC7A5, SLC3A2 and 18S rRNA (as a loading control) (Supplementary Table 3). Gene expression from each genotype at each time point was tested in triplicate. Each of the three measurements was made on cells derived from individual wells.

Glucose-13C6 flux metabolomics

Cell preparation for flux metabolomics

225,000 cells from each genotype (MUT-null, PA-null, WT) were plated into five 100 mm culture dishes (n = 5 per genotype) in DMEM (Gibco, Thermo Fisher Scientific) with 10% FBS (Gemini Bio-Products) and 1% L-glutamine (Gibco, Thermo Fisher Scientific). When

cells reached 70% confluency, log phase of growth, growth media was replaced with DMEM-no glucose (Gibco, Thermo Fisher Scientific), with 10% FBS (Gemini Bio-Products), 1% L-glutamine (Gibco, Thermo Fisher Scientific), and D-Glucose-13C6 to a final concentration of 4500 mg/L (Cambridge Isotope Laboratories, Inc.). After 8 h, cells were washed, and metabolites were extracted from each dish (n = 5 for each genotype). An internal control (Human Metabolome Technologies, Inc.) was added to each sample, followed by ultrafiltration of cell extracts and sample evaporation. Samples were stored at −80 °C.

Metabolite measurements

The metabolite samples were further processed and analyzed by Human Metabolome Technologies (HMT). Briefly, the compounds were measured in the Cation and Anion modes of Capillary Electrophoresis Time-of-Flight Mass Spectrometry (CE-TOFMS) followed by metabolome analysis on an Agilent CE-TOFMS system (Agilent Technologies Inc.) Cationic samples were run in ESI positive mode and anionic samples were run in ESI negative mode [35,36].

Data processing and quantification

Peaks detected by CE-TOFMS analysis were extracted using automatic integration software (MasterHands ver. 2.17.1.11 developed at Keio University) in order to obtain peak information including m/z, migration time (MT), and peak area. Putative metabolites were then assigned from HMT's target library and their isotopic ions on the basis of m/z and MT. Absolute quantification was performed for total amount of each detected metabolite. All the metabolite concentrations were calculated by normalizing the peak area

of each metabolite with respect to the area of the internal standard and by using standard curves, which were obtained by single-point (100 μM) calibrations.

2.4 Results

Differentially expressed proteins in fibroblasts from patients with propionic acidemia (PA) and methylmalonic acidemia (MMA)

Discovery proteomics analysis was performed on fibroblasts from individuals with PA (n = 2), MMA (n = 2), and WT (n = 2) in order to generate hypotheses about novel adaptive pathways in MMA and PA, with the goal of performing targeted studies downstream to validate pathways of interest. A total of 4086 proteins were identified across the MMA, PA and WT fibroblast cohorts. To eliminate intra-cohort discordance, we removed all proteins that fell beyond 2 standard deviations of the mean protein abundance for each matched pair (i.e. MMA1/MMA2, PA1/PA2, and WT1/WT2). After this exclusion, 3449 proteins were considered for inter-cohort analysis (Fig. 1, Supplementary Fig. 1).

We then identified proteins with significant differential expression between disease groups (inter-cohort) by selecting proteins that fell beyond 2 standard deviations from the mean protein abundance across all proteins measured for each disease pair (i.e. PA/WT and MMA/WT). In the control vs PA fibroblast cohort comparison, a total of 103 proteins fell at least 2 standard deviation below the mean, and 95 proteins fell at least 2 standard deviations above the mean. In the control vs MMA fibroblast cohort comparison, a total of 111 proteins fell at least 2 standard deviations below the mean, and 69 proteins fell at least 2 standard deviations above the mean (Fig. 1). The 378 differentially expressed proteins were then assessed via in silico functional analysis using DAVID to determine KEGG

pathways and GO terms enriched for the proteins of interest (Supplementary Table 4). Pathways were tested for significant enrichment via Fisher Exact test.

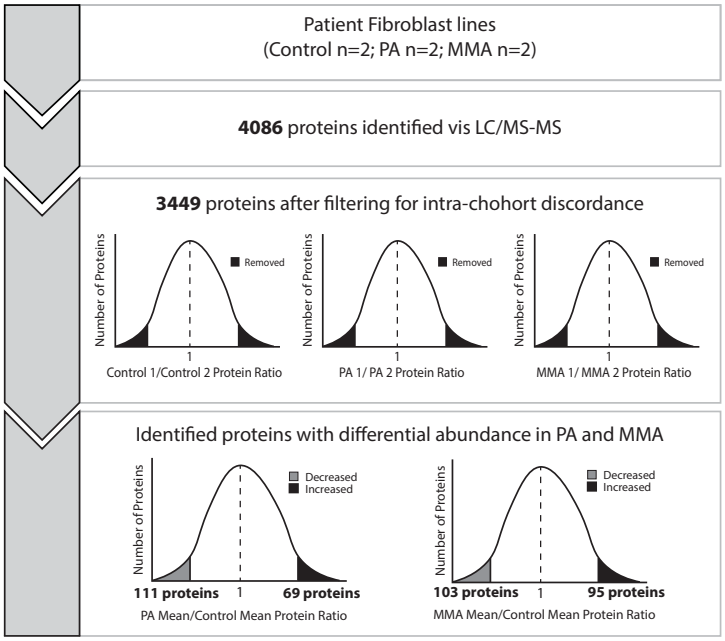

Figure 1. Workflow for proteomics analysis. A total of 4086 proteins were identified across the MMA (n = 2), PA (n = 2) and WT (n = 2) fibroblast cohorts. We removed all proteins that fell beyond 2 standard deviations of the mean protein abundance for each matched pair from further analysis. After this exclusion, 3449 proteins were considered for further analysis to determine differentially expressed proteins between cases and controls. Proteins with abundances that fell above +2 or below −2 standard deviations when comparing PA/Control and MMA/Control were then considered for functional analysis. MMA, methylmalonic acidemia. PA, propionic acidemia.

Of the 69 proteins with significantly increased abundance in the MMAfibroblast group, KEGG pathway analysis showed significant enrichment for proteins involved in the biosynthesis of amino acids (p = 2.3e−3), and cysteine and methionine metabolism (p = 8.2e−3). Significantly enriched GO terms included: cellular amino acid biosynthetic processes (p =1.1e−4), neutral amino acid transport (p = 4.6e−2), hydrogen sulfide biosynthetic processes (p = 1.4e−2), and transsulfuration (p = 1.8e−2). Of the 95 proteins with significantly increased abundance in the PA fibroblast group, KEGG pathway analysis

showed increased enrichment of proteins involved in biosynthesis of amino acids (approaching statistical significance, p = 7.1e−2). Significantly enriched GO terms included: cellular amino acid biosynthetic processes (p = 7.1e−3), hydrogen sulfide biosynthetic processes (p = 1.9e−2), and transsulfuration (p = 2.4e−2) and neutral amino acid transport (p = 1.3e−2).

Of the 111 proteins with significantly decreased abundance in MMA fibroblast group, KEGG pathway analysis showed significant enrichment of proteins in pyruvate metabolism (p = 3.8e−3), valine, leucine and isoleucine degradation (p = 6.00e−3), among other pathways. Significantly enriched GO terms included: oxidation-reduction process (p = 2.7e−4), autophagy (p = 9.1e−3), and response to hypoxia (p = 2.1e−2). Of the 103 proteins with significantly decreased abundance in PA fibroblast group, KEGG pathway analysis showed significant enrichment of proteins in the following pathways: valine, leucine and isoleucine degradation (p = 4.60e−4), protein digestion and absorption (p = 3.1e−2), and pyruvate metabolism (p = 3.9e−2), and other pathways. Significantly enriched GO terms included: oxidationreduction process (p = 2.4e−3), response to hypoxia (p = 5.1e−4) and branched-chain amino acid catabolic process (5.40e−3).

Plasma metabolomics shows altered levels of metabolites in patients with MMA and PA

Supervised multivariate data analysis (OPLS-DA) showed clear differentiation of control subjects with MMA (Fig. 2A, R2X = 0.45, R2Y = 0.98, Q2 = 0.75) and PA (Fig. 2B, R2X = 0.37, R2Y = 0.97, Q2 = 0.78).

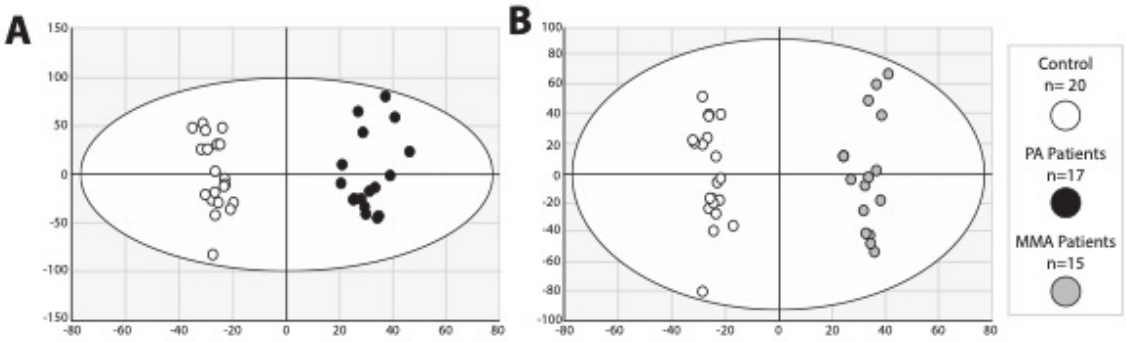

Figure 2. OPLS-DA score plots show clustering of cohorts. Plots showing the separation of **(A)** PA (black filled circles) to control (white filled circles) and **(B)** and MMA (grey filled circles) to control (white filled circles) show that disease cohorts are tightly clustered, and there are no significant outliers. MMA, methylmalonic acidemia. PA, propionic acidemia.

Seven hundred ninety five (795) peaks were identified as being important to differentiating individuals with PA compared to controls (VIP ≥ 2.0 with a jack-knife confidence interval that did not include 0 or a p-value < 0.001) and 60 peaks were library-matched to metabolites. Thirty four (34) individual metabolites were significantly reduced compared with controls (range of−43.3-fold to−1.3-fold), and 25 metabolites were significantly increased compared with controls (range of 1.5-fold to 199.6-fold). Of the 5 metabolites with the most highly increased abundance, one is a known metabolite of propionic acid (propionylcarnitine, 64-fold increase) (Fig. 3). Cystathionine sulfoxide was increased 52-fold compared with controls, which is consistent with the upregulation of sulfur metabolism found in our proteomics studies (Fig. 3). The other three most highly increased metabolites were homocitric acid, which was increased 38-fold, methyl sorbate, which was increased 67.9-fold, and 2-hexenoylcarnitine, which was increased 199.6-fold (Fig. 3).

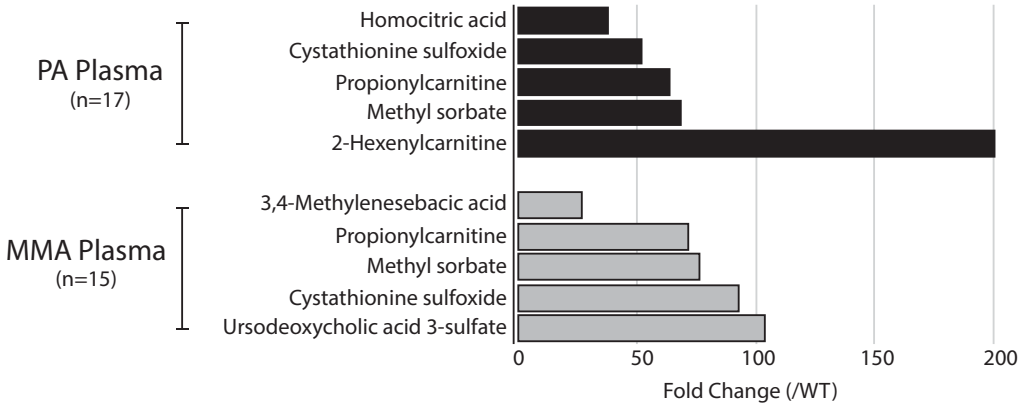

Figure 3. Metabolites with increased abundance in propionic acidemia (PA) and methylmalonic acidemia (MMA) plasma samples. Fold change of the top 5 increased plasma metabolites ($p < 0.001$) in PA and MMA compared to controls.

Eight hundred fifty seven (857) peaks were identified as being important to differentiating individuals with MMA compared to controls (VIP ≥ 2.0 with a jack-knife confidence interval that did not include 0 or a p-value < 0.001) and 56 peaks were library-matched to metabolites. Twenty (20) metabolites had increased abundance compared with controls (range of 2.5-fold to 103.6-fold), and 36 metabolites had decreased abundance compared with controls (range of 1.3-fold to 21.3-fold). Of the 5 metabolites with the most highly increased abundance in samples from MMA patients, one is a well-known metabolite of propionic acid (propionylcarnitine, 71.5-fold increase). Cystathionine sulfoxide was increased 92.9-fold compared with controls, which is consistent with the upregulation of sulfur metabolism found in functional protein annotation. Similar to the PA individuals, methyl sorbate had a 76.5-fold increase, which is flavoring agent and may be a formula artifact but is also a biological product that has precursor structures similar to MMA. The remaining two metabolites of the top 5 include ursodeoxycholic acid 3-sulfate (103.6-fold increase) and 3,4 methylenesebacic acid (27.3-fold increase), whose significance are not known at this time. Additionally, outside of the top 5 metabolites,

glutathione (15.2-fold) and S-formylmethylglutathione (16.3-fold) were also significantly increased in MMA individuals.

Characterization of CRIPSR edited MUT-null and PCCA-null HEK293 cells

CRISPR/Cas9 editing of HEK293 cells targeting exon 12 of *PCCA* resulted in a homozygous 13 bp deletion (*PCCA*$^{E12\Delta13}$) (Fig. 4C). Immunoblotting against PCCA revealed no detectable expression of PCCA (Fig. 4A). CRISPR/Cas9 editing of HEK293 cells targeting exon 5 of *MUT* resulted in a homozygous 22 bp insertion (*MUT*$^{E5\Delta22}$) (Fig. 4D). Immunoblotting against MUT revealed no detectable MUT protein (Fig. 4B).

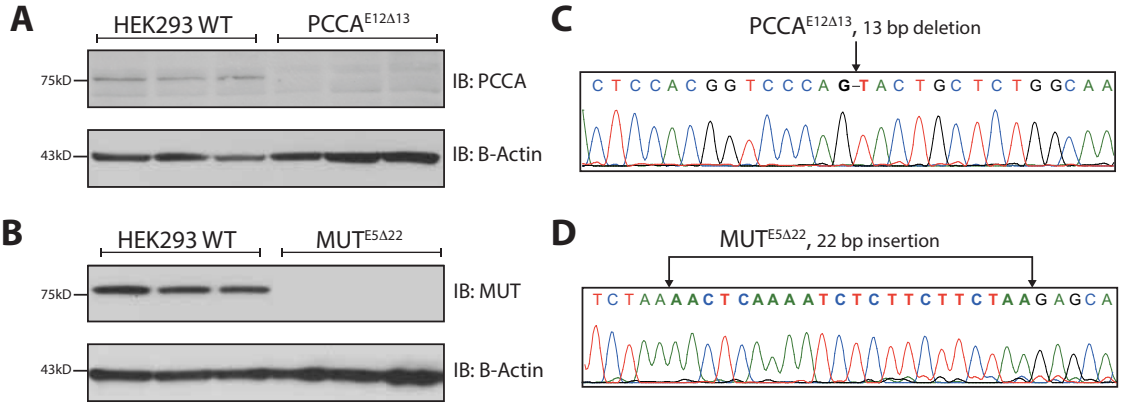

Figure 4. Generation of MUT-null and PCCA-null HEK293 cells. (A) Immunoblot shows absent expression of PCCA in *PCCA*$^{E12\Delta13}$cells (n = 3, serial passages) compared to WT cells (n = 3, serial passages). β-Actin was used as a loading control. **(B)** Immunoblot shows absent expression of MUT in *MUT*$^{E5\Delta22}$ cells (n = 3, serial passages) compared to WT cells (n = 3, serial passages). β-Actin was used as a loading control. **(C)** Sanger sequencing trace of *PCCA*$^{E12\Delta13}$ highlights a 13 bp deletion in exon 12 of *PCCA*. **(D)** Sanger sequencing trace of *MUT*$^{E5\Delta22}$ cells highlights a 22 bp insertion within exon 5 of *MUT*.

Propionylcarnitine (C3) was measured in spent media from confluent *PCCA*$^{E12\Delta13}$ (n = 3, individual 6-well culture wells), *MUT*$^{E5\Delta22}$ (n = 3, individual 6-well culture wells), and WT (n = 3, individual 6-well culture wells) HEK293 cells at days 4, 11 and 18. Both *PCCA*$^{E12\Delta13}$and *MUT*$^{E5\Delta22}$ cells showed a significant increase in the excretion of propionylcarnitine compared to controls at days 11 and 18 (Fig. 5A).

Methylmalonylcarnitine (C5DC) was below the limit of detection in all 3 cell lines. Methylmalonic acid was measured in spent media confluent *PCCA*$^{E12\Delta13}$ (n = 3, individual 6-well culture wells), *MUT*$^{E5\Delta22}$ (n = 3, individual 6-well culture wells), and WT (n = 3, individual 6-well culture wells) HEK293 cells at days 4, 11 and 18. At days 11 and 18, *MUT*$^{E5\Delta22}$ cells had significantly increased excretion of methylmalonic acid compared to both control and *PCCA*$^{E12\Delta13}$ cells (Fig. 5B). Additionally, the methylmalonic acid in spent media was decreased in *PCCA*$^{E12\Delta13}$ cells compared to controls, which is expected because the metabolic block in PA inhibits the production of methylmalonic acid.

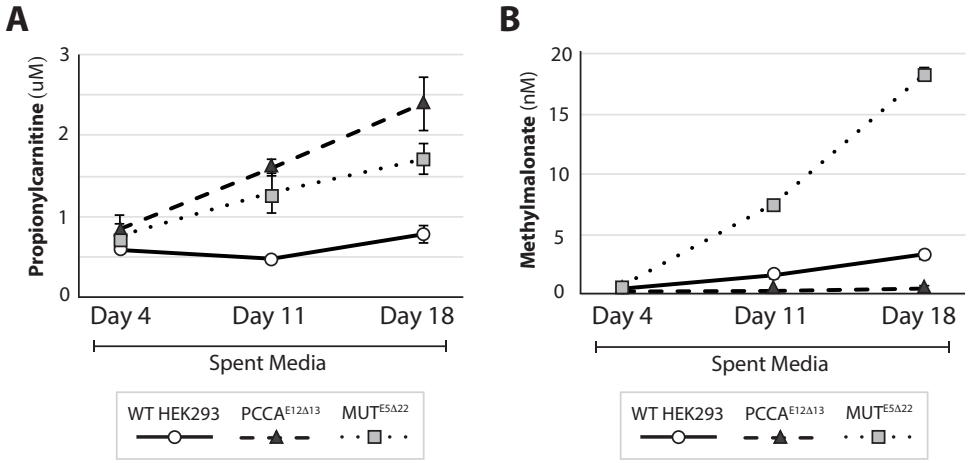

Figure. 5. Metabolites in spent media from in *PCCA*$^{E12\Delta13}$, *MUT*$^{E5\Delta22}$ cells and WT cells. (A) Propionylcarnitine (C3) levels are significantly higher in spent media at 11 and 18 days of growth in *PCCA*$^{E12\Delta13}$ (dashed line) and *MUT*$^{E5\Delta22}$ cells (dotted line) cells compared to WT (solid line). **(B)** Methylmalonate levels are significantly higher in spent media at 11 and 18 days of cell growth in *MUT*$^{E5\Delta22}$ cells (dotted line) compared to *PCCA*$^{E12\Delta13}$ (dashed line) and WT (solid lines) cells, and in WT compared to *PCCA*$^{E12\Delta13}$ cells. (n= 3, individual 6-well culture wells of each genotype for each metabolite at all time points).

Altered gene expression in PCCA$^{E12\Delta13}$*, MUT*$^{E5\Delta22}$*, and WT cells*

Based on our proteomic and metabolomic findings we selected 5 genes to assess for mRNA expression in the *PCCA*$^{E12\Delta13}$ and *MUT*$^{E5\Delta22}$ cells: *CBS*, *PSAT*, *SLC7A5*, *SLC3A2*, and *ASNS*. *CBS* and *PSAT* have critical roles in serine and thiol metabolism and have

significantly increased protein expression in MMA and PA patient-derived fibroblasts. *SLC7A5* and *SLC3A2* are involved in the transport of serine across the cellular membrane and have increased expression in MMA and PA patient derived fibroblasts. *ASNS* is a canonical target of the ATF4 transcription factor, which helps to regulate the integrated cellular stress response [37].

We measured RNA expression in $PCCA^{E12\Delta13}$ (n = 3, individual culture wells), $MUT^{E5\Delta22}$ (n = 3, individual culture wells) and WT cells (n = 3, individual culture wells) at 1, 2, 4 and 8 days after plating to capture gene expression through the log phase of growth and at confluence (Supplementary Fig. 2). Each experiment was carried with n = 3, 3 individual 6-well culture wells analyzed per genotype per time point.

At day 4 (~70% confluence, log phase of growth), $MUT^{E5\Delta22}$ had increased expression of serine transporter gene *SLC7A5* (1.6-fold) and *SLC3A2* (1.7-fold) compared to WT. $PCCA^{E12\Delta13}$ had increased expression of *ASNS* compared to WT (2.7-fold). Additionally, $PCCA^{E12\Delta13}$ had decreased expression of both serine transporters gene *SLC7A5* and *SLC3A2* (0.3-fold and 0.5-fold, respectively) compared to WT. *CBS* and *PSAT1* expression was comparable to WT for both $MUT^{E5\Delta22}$ and $PCCA^{E12\Delta13}$ (Fig. 6A).

At day 8 (cells at confluence), $PCCA^{E12\Delta13}$ and $MUT^{E5\Delta22}$ had increased expression of *ASNS* (1.4-fold and 1.7-fold, respectively) and *PSAT1* (2.0-fold and 3.1-fold, respectively) compared to WT. Additionally, both $PCCA^{E12\Delta13}$ and $MUT^{E5\Delta22}$ had decreased expression of *SLC7A5* (0.1-fold and 0.3-fold, respectively) and *SLC3A2* (0.2-fold and 0.9-fold, respectively) compared to WT (Fig. 6B).

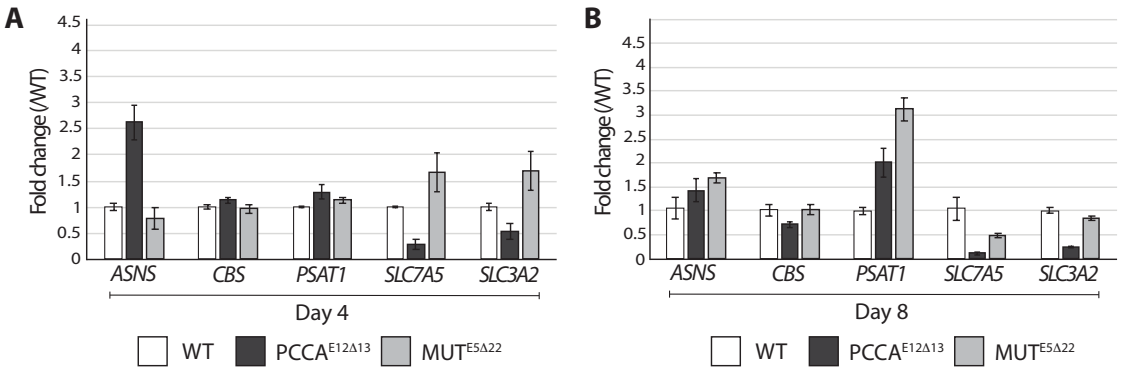

Figure 6. mRNA expression in *PCCA*$^{E12\Delta13}$ and *MUT*$^{E5\Delta22}$ cells at 4 and 8 days of growth. (A) At day 4 (log phase of growth), *MUT*$^{E5\Delta22}$ had increased expression of serine transporter gene *SLC7A5* (1.6-fold) and *SLC3A2* (1.7-fold) compared to WT, though this did not reach statistical significance. Additionally, *PCCA*$^{E12\Delta13}$ had significantly decreased expression of both serine transporters gene *SLC7A5 andSLC3A2* (0.3 fold and 0.5-fold, respectively) compared to WT. **(B)** At day 8 (cells at confluence), *PCCA*$^{E12\Delta13}$ and *MUT*$^{E5\Delta22}$ had increased expression of *ASNS* (1.4-fold and 1.7-fold, respectively) and *PSAT1* (2.0-fold and 3.1-fold, respectively) compared to WT. Additionally, *PCCA*$^{E12\Delta13}$ had significantly decreased expression of *SLC7A5* (0.1-fold) and *SLC3A2* (0.2-fold) compared to WT. (n=3, 3 individual 6-well culture wells per genotype per time point) (n=3, 3 individual 6-well culture wells analyzed per genotype per time point). *indicates a statisticially significant change ($p < 0.05$) compared to WT.

Flux metabolomics reveals alteration in serine synthesis and transport

From CE-TOFMS measurement, 231 peaks (112 in Cation and 119 in Anion Mode, respectively) of isotopic ions and their total amount for each compound were identified.

De novo serine synthesis from glucose was increased in both *PCCA*$^{E12\Delta13}$ and *MUT*$^{E5\Delta22}$ cells compared to WT, as shown by the amount of serine with all 3 carbons labeled with 13C (Fig. 7A-B). Additionally, glucose-6-phosphate, with all 6 carbons labeled with ^{13}C, was significantly reduced in both *PCCA*$^{E12\Delta13}$ and *MUT*$^{E5\Delta22}$ compared to WT (0.4-fold reduction (p=5.7e-04) and 0.6-fold reduction (p=0.019) respectively) indicating a rapid flux towards serine biosynthesis, as glucose-6-phosphate is a pool of "trapped" intracellular glucose for cellular metabolite biosynthesis. Lastly, glycine with both carbons labeled with ^{13}C, which is the product of SHMT from serine, was significantly

increased in *PCCA*$^{E12\Delta13}$ compared to WT (1.2-fold increase, p=0.018) but not *MUT*$^{E5\Delta22}$ compared to WT (data not shown). Interestingly, serine transport (as measured by serine with no ^{13}C labeled carbons) was only increased in *MUT*$^{E5\Delta22}$ (Fig. 7C).

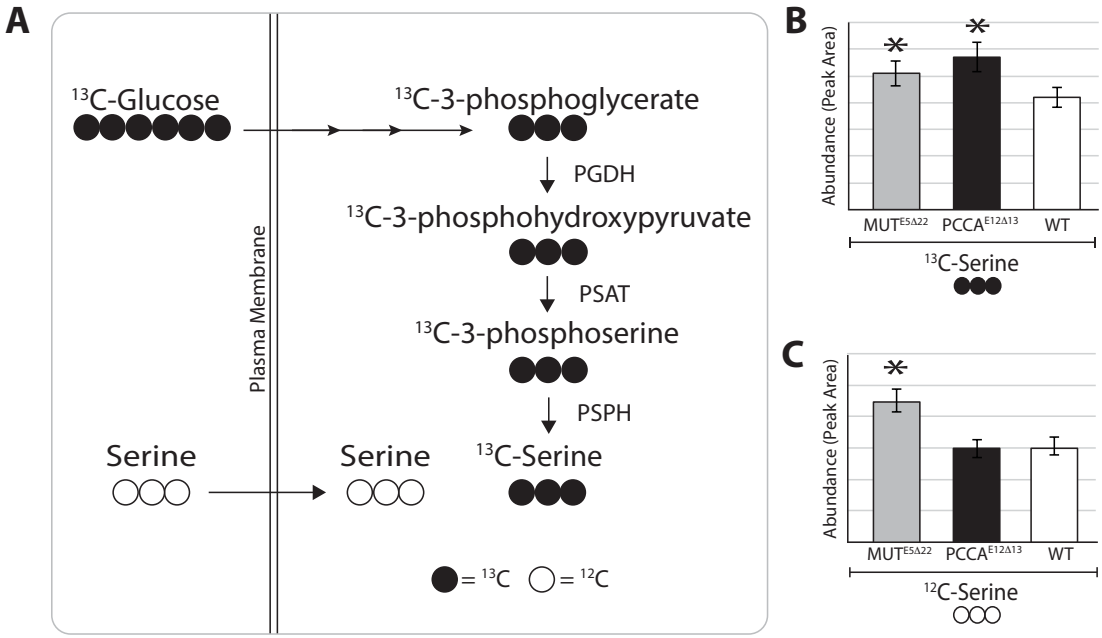

Figure 7. Serine biosynthesis and transport in *MUT*$^{E5\Delta22}$ and *PCCA*$^{E12\Delta13}$ cells. (A) ^{13}C labeled glucose (^{13}C-Glucose) is metabolized to ^{13}C labeled serine (^{13}C-Serine). **(B)** *MUT*$^{E5\Delta22}$ (n = 5, individual culture dishes) and *PCCA*$^{E12\Delta13}$ (n = 5, individual culture dishes) cells have significantly increased *de novo* synthesis of serine from extracellular glucose compared to WT cells (n = 5, individual culture dishes) (1.4-fold increase (p = 0.001) and 1.2-fold increase (p = 0.007), respectively). **(C)** Additionally, the intracellular pool of unlabeled serine (^{12}C-Serine) is significantly higher in *MUT*$^{E5\Delta22}$ compared to both WT and *PCCA*$^{E12\Delta13}$ (1.7-fold increase (p = 5.6e−05) and 1.8 fold increase (p = 4.6e−05), respectively) indicating increased uptake from the extracellular milieu. Values (y-axis) are represented as average MS peak heights±standard deviation for each genotype. Raw values were corrected for protein content. *indicates a statistically significant ($p < 0.05$) compared to WT.

In addition to evaluating serine biosynthetic intermediates, we also evaluated the entrance of pyruvate with all three carbons labeled with ^{13}C, into the TCA cycle (Fig. 8). The TCA cycle intermediates we assessed are from the first "turn" of the cycle and therefore have two carbons labeled with 13C. In *MUT*$^{E5\Delta22}$ cells, proximal TCA cycle

intermediates, with the exception of isocitrate, are significantly decreased compared to WT (Fig. 8B-E). In *PCCA*$^{E12\Delta13}$ cells, we found that the proximal TCA cycle intermediates are not significantly different compared to WT. Proximal intermediates include: citrate, aconitate, isocitrate, and alpha-ketoglutarate. However, the distal TCA cycle intermediates malate and fumarate are significantly decreased compared to WT (Fig. 8F-G). The differences noted are not due to the availability of labeled pyruvate, since the amount of pyruvate at the start of the cycle is not significantly different between cell types (Fig. 8A).

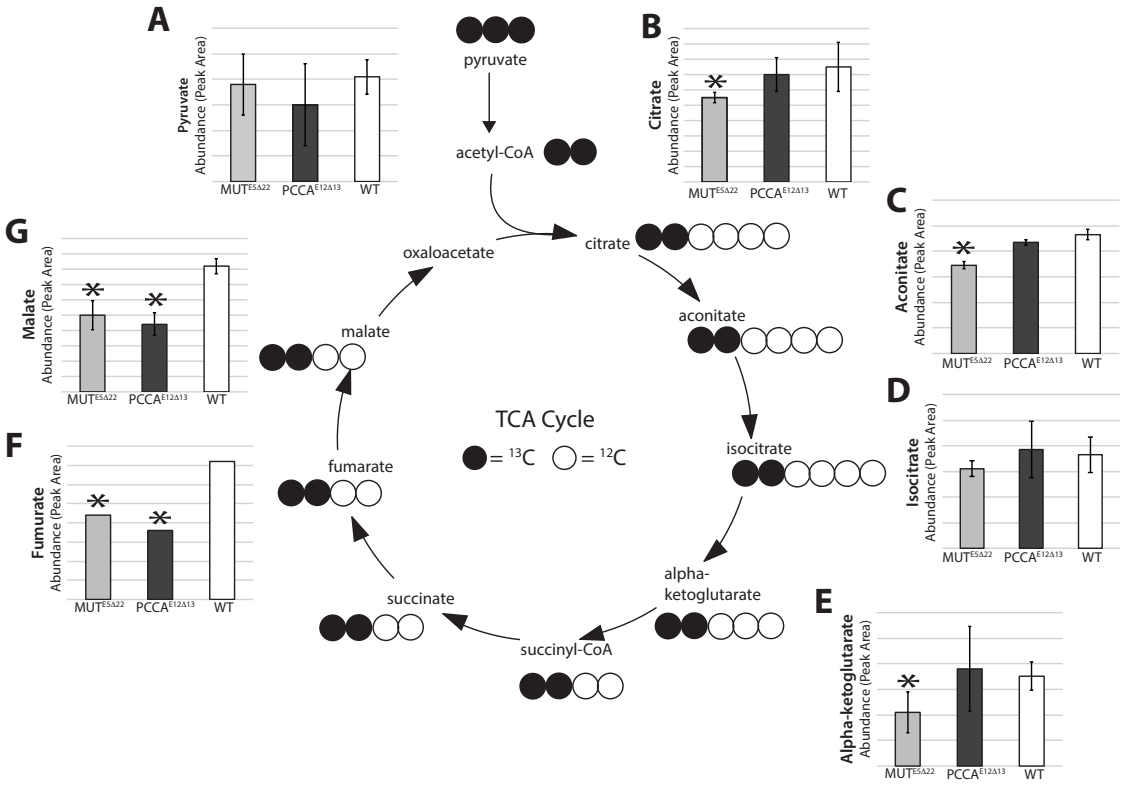

Figure 8. ^{13}C-labeled TCA intermediates *MUT*$^{E5\Delta22}$ and *PCCA*$^{E12\Delta13}$ cells. (A) ^{13}C labeled pyruvate is not significantly different in and *MUT*$^{E5\Delta22}$ (n = 5, separate culture dishes) and *PCCA*$^{E12\Delta13}$ cells (n = 5, separate culture dishes) compared to WT (n = 5, separate culture dishes) **(B)** Citrate is significantly lower in *MUT*$^{E5\Delta22}$ compared to WT (0.7-fold, p = 0.045). **(C)** Aconitate is significantly lower in *MUT*$^{E5\Delta22}$ compared to WT (0.7-fold, p = 0.035). **(D)** Isocitrate is not significantly different between cell types. **(E)** Alpha-ketoglutarate is significantly lower in *MUT*$^{E5\Delta22}$ compared to WT (0.6-fold, p = 0.025). **(F)** Fumarate is significantly lower in *MUT*$^{E5\Delta22}$ and *PCCA*$^{E12\Delta13}$ compared to WT (0.6-fold (p = 0.002) and 0.5 fold (p = 1.9e−04) respectively). **(G)** Malate is

significantly lower in *MUT*$^{E5\Delta22}$ and *PCCA*$^{E12\Delta13}$ compared to WT (0.6-fold ($p = 7.8e{-}04$) and 0.6 fold ($p = 3.6e{-}05$) respectively). Values (y-axis) are represented as average MS peak heights±standard deviation for each genotype. Raw values were corrected for protein content.13C labeled succinate, succinyl CoA, oxaloacetate and acetyl CoA were not measured in this assay due to technical limitations. *indicates a statistically significant ($p < 0.05$) change compared to WT.

2.5 Discussion

Disturbances in serine metabolism are increasingly implicated as a mechanism of response to mitochondrial stress in primary mitochondrial disease [2–4,38]. Evidence points towards shifting of serine flux towards synthesis of one-carbon metabolite intermediates and glutathione [2,3]. In this study, we provide multiple lines of evidence to demonstrate similar secondary metabolic disturbances in methylmalonic acidemia (MMA) and propionic acidemia (PA), suggesting that adaptations in serine metabolism represent a central theme of the cellular response to diverse mitochondrial stressors. This has significant implications for identifying both novel targets for therapeutic intervention, and targets for clinical monitoring in both primary and secondary disorders of mitochondrial function.

We employed a discovery proteomics approach in fibroblasts from individuals with PA and MMA, in order to generate hypotheses about novel adaptive pathways in these disorders. Here we uncovered potential adaptations in serine and thiol metabolism. We then undertook a series of targeted studies downstream to validate these adaptations, and to understand their potential role in the pathogenesis of MMA and PA.

In PA and MMA patient derived fibroblasts, we uncovered an enrichment of proteins involved in serine and thiol metabolism, including phosphoserine aminotransferase (PSAT), cystathionine beta synthase (CBS), and mercaptopyruvate

sulfurtransferase (MPST). Additionally, we also identified increased expression of multiple canonical proteins whose corresponding gene expression is regulated by the transcription factor ATF4. This is particularly relevant because ATF4 activation is known to activate serine biosynthesis and has also been reported in various models of primary mitochondrial disease [2]. In the MMA fibroblasts, proteins with significantly increased expression correspond with classic ATF4 response genes BCAT, ASNS, SLC7A5, and PSAT. These same genes had increased protein expression in the PA fibroblasts, as well as one other classic ATF4 response gene, SLC38A2 (SNAT2) [39,40]. Activation of ATF4 in response to mitochondrial stress results in the upregulation of genes involved in the integrated response to adapt and alter cellular metabolism [37].

We chose to model MMA and PA in HEK293 cells due to their well characterized mitochondrial function, retention of relevant biochemical pathways, amenability to metabolomic tracer studies, and prior evidence for in vivo relevance in other disorders of mitochondrial intermediary metabolism [2,41]. Once our *PCCA*-null and *MUT*-null CRISPR edited HEK293 cells were shown to faithfully replicate the canonical biochemical defects in MMA and PA, we showed that these cells had alterations in expression of genes associated with serine biosynthesis and ATF4 regulation. Serial measurements of gene expression during the lag, exponential (log), and stationary phases of cell growth of the *PCCA*-null and *MUT*-null cells show differential expression compared to WT. Genes encoding for neutral amino acid transport including serine (*SLC3A2* and *SLC7A5*) had increased expression during early phases of growth, while genes associated with amino acid metabolism had increased expression during later phases of growth (*ASNS*, *PSAT*).

In order to determine the biochemical etiology and downstream intracellular fate of serine, we performed 13C-labeled glucose flux experiments in *PCCA*- and *MUT*-null HEK293 cells. We found that both cell types have an increased de novo synthesis from extracellular glucose. In addition to elevations of 13C-serine in *MUT*-null cells, we also observed increased unlabeled serine compared to WT and *PCCA*-null cells. This could indicate either increased transport of serine from the periphery in the *MUT*-null cells, or increased serine biosynthesis from other intracellular sources. At this time, it is not clear why the *MUT* and *PCCA*-null cells are different in this regard.

Interestingly, 13C-flux experiments also showed increased de novo synthesis of glycine from 13C-serine in *PCCA*-null cells. Massive elevations in plasma glycine are commonly seen in individuals with PA. In fact, before the canonical organic acid was identified, PA disorder was originally named "non-ketotic hyperglycinemia" [42,43]. It has been previously hypothesized that the increased plasma glycine could be due to inhibition of the glycine cleavage system [44]. However, our results would suggest that increased synthesis from serine may contribute to elevated plasma levels of glycine found in PA compared to unaffected individuals [43]. We did not observe an increase in de novo glycine synthesis in the *MUT*-null cells. While increased glycine levels may also be seen in MMA compared to unaffected individuals, typically it is at a significantly lower level than the plasma glycine levels observed in PA [43]. Perhaps introduction of mitochondrial stress in the *MUT*-null cellular model could induce elevated glycine synthesis.

In addition to alterations in biosynthesis of serine, we also examined the flux of 13C-labeled glucose into the TCA cycle. Anaplerotic deficiencies of the TCA cycle have been previously described in MMA and PA, and anaplerotic therapy has been suggested as

a mechanism of treatment in these disorders [45,46]. These deficiencies are intuitive considering that the metabolic flux of propionyl-CoA metabolism is towards succinyl-CoA. However, we found that *MUT*-null cells have proximal defects in the TCA cycle, which may represent defective conversion of pyruvate to acetyl CoA at the step of pyruvate dehydrogenase. Thus, the TCA cycle defects in MMA cannot be solely due to limited flux of propionyl-CoA into succinyl-CoA.

Furthermore, in *PCCA*-null cells, we found that flux of 13C labeled alpha-ketoglutarate to the distal segment of the TCA cycle is limited. This could be at the step of either alpha-ketoglutarate dehydrogenase or succinate dehydrogenase. Within the current experiment, we were unable to measure 13C labeled succinate, and therefore we are unable to resolve the precise location of this relative metabolic inhibition. However, as seen in *MUT*-null cells, the anaplerotic abnormalities in PA are not solely due to limited flux of propionyl-CoA into succinyl-CoA.

From a clinical standpoint, abnormally low plasma serine has been reported in a number of individuals with various primary mitochondrial disorders, and has also been reported in an individual with MMA after liver/kidney transplant [4,47]. Importantly, re-disturbed flux of serine has been shown to paradoxically deprive some biologically important synthetic pathways of serine (i.e. sphingolipid synthesis), thus resulting in biochemical and clinical pathogenesis [4]. Therefore, correction of serine deficits is potentially highly clinically relevant.

Further studies are necessary to determine if serine levels vary with metabolic stress, i.e. depletion of bioenergetic precursors. Our evidence would suggest that provision of glucose is particularly important for the de novo biosynthesis of serine in MMA and PA.

It follows, that serine supplementation could represent an avenue for therapy, though our evidence would suggest that this could be more beneficial in MMA, where transport of extracellular serine (as opposed to *de novo* synthesis) may be the dominant mechanism. There are several limitations to this work. The measurements of unlabeled TCA cycle intermediates in our experiment are unable to differentiate between cytoplasmic and mitochondrial metabolites. Therefore, we are unable to estimate the total amounts of mitochondrial TCA intermediates. Additionally, while HEK293 cells are derived from human kidney cells, they do not necessarily represent the affected tissues in MMA and PA. Therefore, we cannot be sure our HEK293 cellular models are capturing the full extent of the adaption and alteration of cellular metabolism in response to mitochondrial stress in MMA and PA. However, the confluence of evidence from the three biological experimental systems (patient-derived fibroblasts, patient-derived plasma, and cellular modeling) provides a strong argument for the importance of serine metabolism in the cellular pathogenesis of these disorders.

In future work, we plan to expand upon these findings, and explore how substrate utilization differs in the setting of bioenergetic stress, such as starvation or increased reactive oxygen stress. This may provide insight into the biochemical adaptations that occur in the setting of physiologic stressors and metabolic crises in individuals with MMA and PA.

2.6 References

1. S.C. Kalhan, R.W. Hanson, Resurgence of serine: an often neglected but indispensable amino acid, J. Biol. Chem. 287 (24) (2012) 19786–19791.

2. X.R. Bao, S.E. Ong, O. Goldberger, J. Peng, R. Sharma, D.A. Thompson, S.B. Vafai, A.G. Cox, E. Marutani, F. Ichinose, et al., Mitochondrial dysfunction remodels onecarbon metabolism in human cells, Elife 5 (2016).
3. J. Nikkanen, S. Forsstrom, L. Euro, I. Paetau, R.A. Kohnz, L. Wang, D. Chilov, J. Viinamaki, A. Roivainen, P. Marjamaki, et al., Mitochondrial DNA replication defects disturb cellular dNTP pools and remodel one-carbon metabolism, Cell Metab. 23 (4) (2016) 635–648.
4. C.R. Ferreira, S.M.I. Goorden, A. Soldatos, H.M. Byers, Vlugt J.M.M. Ghauharali-vander, F.S. Beers-Stet, C. Groden, C.D. van Karnebeek, W.A. Gahl, F.M. Vaz, et al., Deoxysphingolipid precursors indicate abnormal sphingolipid metabolism in individuals with primary and secondary disturbances of serine availability, Mol. Genet. Metab. 124 (3) (2018) 204–209.
5. D. Samanta, G.L. Semenza, Serine synthesis helps hypoxic cancer stem cells regulate redox, Cancer Res. 76 (22) (2016) 6458–6462.
6. B. Liu, Y. Jia, Y. Cao, S. Wu, H. Jiang, X. Sun, J. Ma, X. Yin, A. Mao, M. Shang, Overexpression of phosphoserine aminotransferase 1 (PSAT1) predicts poor prognosis and associates with tumor progression in human esophageal squamous cell carcinoma, Cell. Physiol. Biochem. 39 (1) (2016) 395–406.
7. C. Qian, Y. Xia, Y. Ren, Y. Yin, A. Deng, Identification and validation of PSAT1 as a potential prognostic factor for predicting clinical outcomes in patients with colorectal carcinoma, Oncol. Lett. 14 (6) (2017) 8014–8020.
8. Y. Yang, J. Wu, J. Cai, Z. He, J. Yuan, X. Zhu, Y. Li, M. Li, H. Guan, PSAT1 regulates cyclin D1 degradation and sustains proliferation of non-small cell lung cancer cells, Int. J. Cancer 136 (4) (2015) E39–E50.
9. Shchelochkov OA, Carrillo N, Venditti C: Propionic acidemia. In: GeneReviews((R)). Edited by Adam MP, Ardinger HH, Pagon RA, Wallace SE, Bean LJH, Stephens K, Amemiya A. Seattle (WA); 1993.
10. Manoli I, Sloan JL, Venditti CP: Isolated methylmalonic acidemia. In: GeneReviews ((R)). Edited by Adam MP, Ardinger HH, Pagon RA, Wallace SE, Bean LJH, Stephens K, Amemiya A. Seattle (WA); 1993.
11. J.P. Kraus, E. Spector, S. Venezia, P. Estes, P.W. Chiang, G. Creadon-Swindell, S. Mullerleile, L. de Silva, M. Barth, M. Walter, et al., Mutation analysis in 54 propionic acidemia patients, J. Inherit. Metab. Dis. 35 (1) (2012) 51–63.
12. P. Forny, A.S. Schnellmann, C. Buerer, S. Lutz, B. Fowler, D.S. Froese, M.R. Baumgartner, Molecular genetic characterization of 151 Mut-type methylmalonic aciduria patients and identification of 41 novel mutations in MUT, Hum. Mutat. 37 (8) (2016) 745–754.
13. B. Fowler, J.V. Leonard, M.R. Baumgartner, Causes of and diagnostic approach to methylmalonic acidurias, J. Inherit. Metab. Dis. 31 (3) (2008) 350–360.
14. J.L. Fraser, C.P. Venditti, Methylmalonic and propionic acidemias: clinical management update, Curr. Opin. Pediatr. 28 (6) (2016) 682–693.
15. M.R. Baumgartner, F. Horster, C. Dionisi-Vici, G. Haliloglu, D. Karall, K.A. Chapman, M. Huemer, M. Hochuli, M. Assoun, D. Ballhausen, et al., Proposed guidelines for the diagnosis and management of methylmalonic and propionic acidemia, Orphanet J Rare Dis 9 (2014) 130.
16. S.C. Grunert, S. Mullerleile, L. De Silva, M. Barth, M. Walter, K. Walter, T. Meissner, M. Lindner, R. Ensenauer, R. Santer, et al., Propionic acidemia: clinical course andoutcome in 55 pediatric and adolescent patients, Orphanet J Rare Dis 8 (2013) 6.
17. R.J. Chandler, P.M. Zerfas, S. Shanske, J. Sloan, V. Hoffmann, S. DiMauro, C.P. Venditti, Mitochondrial dysfunction in mut methylmalonic acidemia, FASEB J. 23 (4) (2009) 1252–1261.
18. Z.K. Zsengeller, N. Aljinovic, L.A. Teot, M. Korson, N. Rodig, J.L. Sloan, C.P. Venditti, G.T. Berry, S. Rosen, Methylmalonic acidemia: a megamitochondrial disorder affecting the kidney, Pediatr. Nephrol. 29 (11) (2014) 2139–2146.
19. K.A. Chapman, J. Ostrovsky, M. Rao, S.D. Dingley, E. Polyak, M. Yudkoff, R. Xiao, M.J. Bennett, M.J. Falk, Propionyl-CoA carboxylase pcca-1 and pccb-1 gene deletions in Caenorhabditis elegans globally impair mitochondrial energy metabolism, J. Inherit. Metab. Dis. 41 (2) (2018) 157–168.
20. S.M. Pinto, R.S. Nirujogi, P.L. Rojas, A.H. Patil, S.S. Manda, Y. Subbannayya, J.C. Roa, A. Chatterjee, T.S. Prasad, A. Pandey, Quantitative phosphoproteomic analysis of IL-33-mediated signaling, Proteomics 15 (2–3) (2015) 532–544.

21. Huang da W, Sherman BT, Lempicki RA: Systematic and integrative analysis of large gene lists using DAVID bioinformatics resources. Nat. Protoc. 2009, 4(1):44–57.
22. Huang da W, Sherman BT, Lempicki RA: Bioinformatics enrichment tools: paths toward the comprehensive functional analysis of large gene lists. Nucleic Acids Res. 2009, 37(1):1–13.
23. W.B. Dunn, D. Broadhurst, P. Begley, E. Zelena, S. Francis-McIntyre, N. Anderson, M. Brown, J.D. Knowles, A. Halsall, J.N. Haselden, et al., Procedures for large-scale metabolic profiling of serum and plasma using gas chromatography and liquid chromatography coupled to mass spectrometry, Nat. Protoc. 6 (7) (2011) 1060–1083.
24. S. Dhungana, J.E. Carlson, W. Pathmasiri, S. McRitchie, M. Davis, S. Sumner, S.E. Appt, Impact of a western diet on the ovarian and serum metabolome, Maturitas 92 (2016) 134–142.
25. B.K. Williamson, N.M. Hawkey, D.A. Blake, J.W. Frenkel, K.P. McDaniel, J.K. Davis, C. Satija, A. Beazer, S. Dhungana, J. Carlson, et al., The effects of glaucoma drainage devices on oxygen tension, glycolytic metabolites, and metabolomics profile of aqueous humor in the rabbit, Transl Vis Sci Technol 7 (1) (2018) 14.
26. J. Trygg, E. Holmes, T. Lundstedt, Chemometrics in metabonomics, J. Proteome Res. 6 (2) (2007) 469–479.
27. Eriksson L BT, Johansson E, Trygg J, Vikström C. Multi- and Megavariate Data Analysis: Basic Principles and Applications. 3rd ed. Umeå, Sweden: Umetric Academy; 2013.
28. Yang L, Yang JL, Byrne S, Pan J, Church GM: CRISPR/Cas9-directed genome editing of cultured cells. Curr Protoc Mol Biol 2014, 107:31 31 31–17.
29. L.R. Desviat, B. Perez, C. Perez-Cerda, P. Rodriguez-Pombo, S. Clavero, M. Ugarte, Propionic acidemia: mutation update and functional and structural effects of the variant alleles, Mol. Genet. Metab. 83 (1–2) (2004) 28–37.
30. F.A. Ran, P.D. Hsu, J. Wright, V. Agarwala, D.A. Scott, F. Zhang, Genome engineering using the CRISPR-Cas9 system, Nat. Protoc. 8 (11) (2013) 2281–2308.
31. P. Rinaldo, T.M. Cowan, D. Matern, Acylcarnitine profile analysis, Genet Med 10 (2) (2008) 151–156.
32. Smith EH, Matern D: Acylcarnitine analysis by tandem mass spectrometry. Curr Protoc Hum Genet 2010, Chapter 17:Unit 17 18 11–20.
33. K. Rasmussen, Solid-phase sample extraction for rapid determination of methylmalonic acid in serum and urine by a stable-isotope-dilution method, Clin. Chem. (2) (1989) 260–264.
34. Green MR, Sambrook J: Quantification of RNA by real-time reverse transcriptionpolymerase chain reaction (RT-PCR). Cold Spring Harb Protoc 2018, 2018(10):pdbprot095042.
35. T. Soga, Y. Ueno, H. Naraoka, Y. Ohashi, M. Tomita, T. Nishioka, Simultaneous determination of anionic intermediates for Bacillus subtilis metabolic pathways by capillary electrophoresis electrospray ionization mass spectrometry, Anal. Chem. 74 (10) (2002) 2233–2239.
36. T. Soga, Y. Ohashi, Y. Ueno, H. Naraoka, M. Tomita, T. Nishioka, Quantitative metabolome analysis using capillary electrophoresis mass spectrometry, J. Proteome Res. 2 (5) (2003) 488–494.
37. P.M. Quiros, M.A. Prado, N. Zamboni, D. D'Amico, R.W. Williams, D. Finley, S.P. Gygi, J. Auwerx, Multi-omics analysis identifies ATF4 as a key regulator of the mitochondrial stress response in mammals, J. Cell Biol. 216 (7) (2017) 2027–2045.
38. Buzkova J, Nikkanen J, Ahola S, Hakonen AH, Sevastianova K, Hovinen T, YkiJarvinen H, Pietilainen KH, Lonnqvist T, Velagapudi V et al.: Metabolomes of mitochondrial diseases and inclusion body myositis patients: treatment targets and biomarkers. EMBO Mol Med 2018, 10(12).
39. J. Han, S.H. Back, J. Hur, Y.H. Lin, R. Gildersleeve, J. Shan, C.L. Yuan, D. Krokowski, S. Wang, M. Hatzoglou, et al., ER-stress-induced transcriptional regulation increases protein synthesis leading to cell death, Nat. Cell Biol. 15 (5) (2013) 481–490.
40. S. Broer, A. Broer, Amino acid homeostasis and signalling in mammalian cells and organisms, Biochem. J. 474 (12) (2017) 1935–1963.
41. M. Schiff, B. Haberberger, C. Xia, A.W. Mohsen, E.S. Goetzman, Y. Wang, R. Uppala, Y. Zhang, A. Karunanidhi, D. Prabhu, et al., Complex I assembly function and fatty acid oxidation enzyme activity of ACAD9 both contribute to disease severity in ACAD9 deficiency, Hum. Mol. Genet. 24 (11) (2015) 3238–3247.

42. B. Childs, W.L. Nyhan, M. Borden, L. Bard, R.E. Cooke, Idiopathic hyperglycinemia and hyperglycinuria: a new disorder of amino acid metabolism, I. Pediatrics 27 (1961) 522–538.
43. M. Nizon, C. Ottolenghi, V. Valayannopoulos, J.B. Arnoux, V. Barbier, F. Habarou, I. Desguerre, N. Boddaert, J.P. Bonnefont, C. Acquaviva, et al., Long-term neurological outcome of a cohort of 80 patients with classical organic acidurias, Orphanet J Rare Dis 8 (2013) 148.
44. K. Hayasaka, K. Narisawa, T. Satoh, H. Tateda, K. Metoki, K. Tada, K. Hiraga, T. Aoki, T. Kawakami, H. Akamatsu, et al., Glycine cleavage system in ketotic hyperglycinemia: a reduction of H-protein activity, Pediatr. Res. 16 (1) (1982) 5–7.
45. I. Knerr, N. Weinhold, J. Vockley, K.M. Gibson, Advances and challenges in the treatment of branched-chain amino/keto acid metabolic defects, J. Inherit. Metab. Dis. 35 (1) (2012) 29–40.
46. N. Longo, L.B. Price, E. Gappmaier, N.L. Cantor, S.L. Ernst, C. Bailey, M. Pasquali, Anaplerotic therapy in propionic acidemia, Mol. Genet. Metab. 122 (1–2) (2017) 51–59.
47. H.J. Vernon, C.J. Sperati, J.D. King, A. Poretti, N.R. Miller, J.L. Sloan, A.M. Cameron, D. Myers, C.P. Venditti, D. Valle, A detailed analysis of methylmalonic acid kinetics during hemodialysis and after combined liver/kidney transplantation in a patient with mut (0) methylmalonic acidemia, J. Inherit. Metab. Dis. 37 (6) (2014) 899–907.
48. R. Core Team, R: A language and environment for statistical computing, R Foundation for Statistical Computing, Vienna, Austria, 2013, http://www.Rproject.org/.

2.7 Supplementary Information

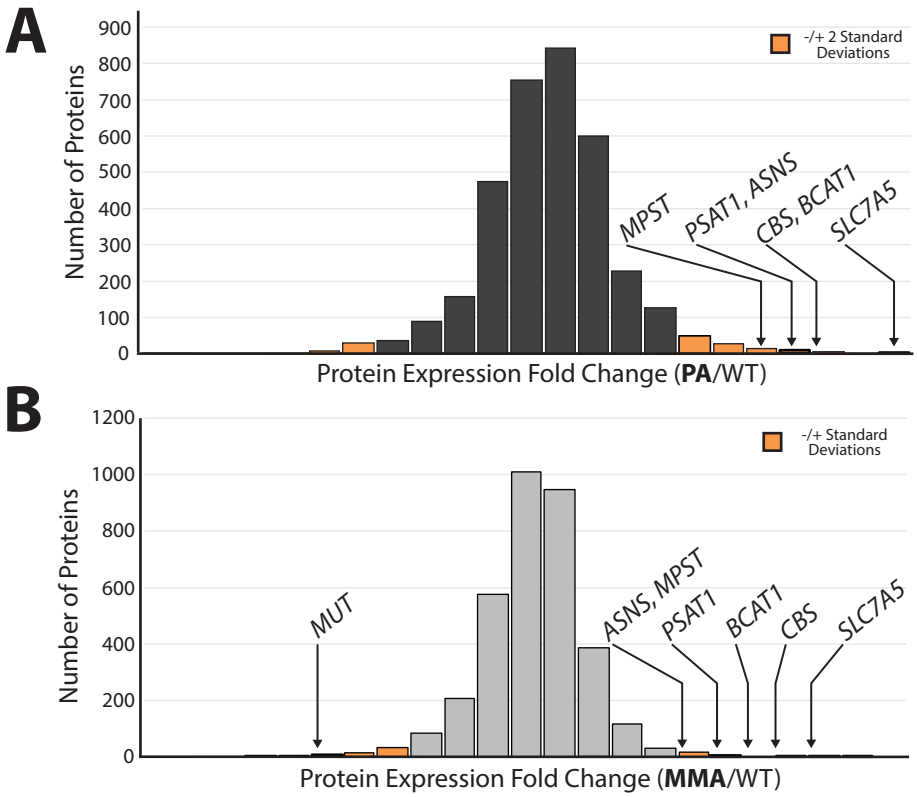

Supplemental Figure 1. Histogram of the protein expression fold change across 3,449 proteins measured via shotgun proteomics in (A) Propionic acidemia fibroblasts compared to controls (PA) and **(B)** Methylmalonic acidemia (MMA) fibroblasts compared to controls. In both PA and MMA, *SLCA7A5*, *CBS*, *BCAT1*, *PSAT1* and *ASNS* have an increased protein expression compared to WT (>2SD above the average protein expression fold change).

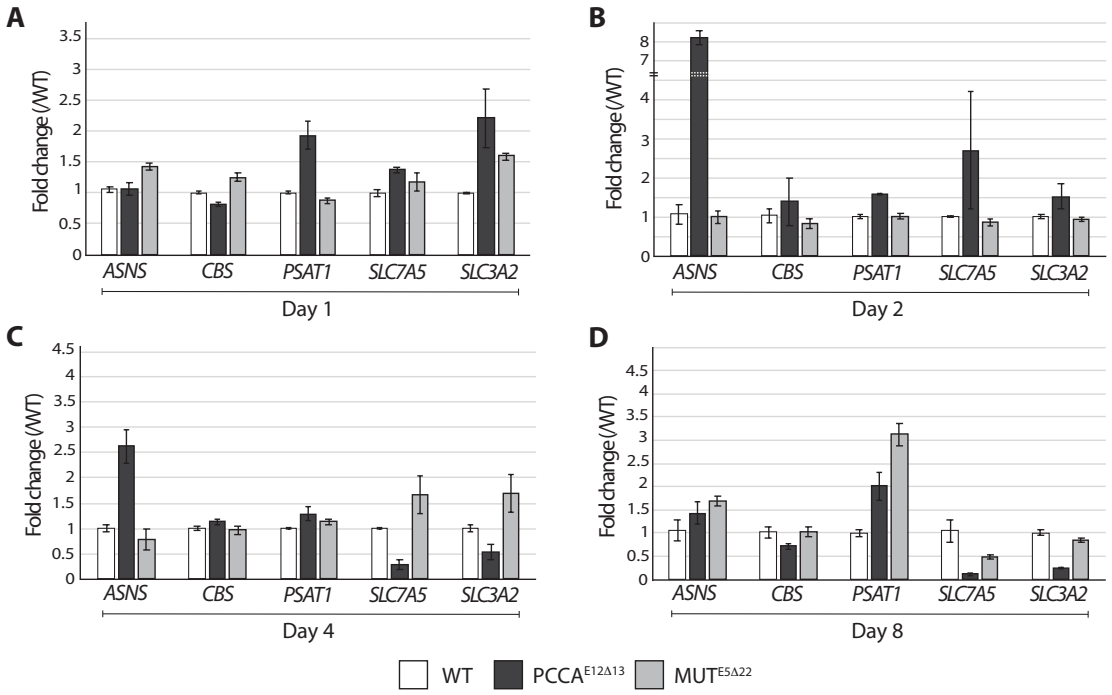

Supplementary Figure 2. mRNA expression in *PCCA*$^{E12\Delta13}$ and *MUT*$^{E5\Delta22}$ cells at 1, 2, 4 and 8 days of growth. (A) At day 1 after seeding culture wells, *MUT*$^{E5\Delta22}$ (n=3, separate culture wells) had significantly increased expression of *ASNS* (1.4-fold), *CBS* (1.2-fold), and *SLC3A2* (1.6-fold) compared to WT. *PCCA*$^{E12\Delta13}$ had significantly increased expression of *PSAT1* (1.9-fold) and *SLC7A5* (1.4 fold) compared to WT. Increased expression of *SLC3A2* approached significance in *PCCA*$^{E12\Delta13}$ compared to WT (2.2 fold, P-value 0.06). **(B)** At day 2 (prior to log phase of growth), *PCCA*$^{E12\Delta13}$ had significantly increased expression of *ASNS* (8.1-fold)and *PSAT1* (1.6-fold) compared to WT. **(C)** At day 4 (log phase of growth), *MUT*$^{E5\Delta22}$ (n=3, separate culture wells) had increased expression of serine transporter gene *SLC7A5* (1.6-fold) and *SLC3A2* (1.7 fold) compared to WT (n=3, separate culture wells), though this did not reach statistical significance. Additionally, *PCCA*$^{E12\Delta13}$ had significantly decreased expression of both serine transporters gene *SLC7A5* and *SLC3A2* (0.3 fold and 0.5-fold, respectively) compared to WT. **(D)** At day 8 (cells at confluence), *PCCA*$^{E12\Delta13}$ and *MUT*$^{E5\Delta22}$had increased expression of *ASNS* (1.4-fold and 1.7-fold, respectively) and *PSAT1* (2.0-fold and 3.1-fold, respectively) compared to WT. Additionally, both *PCCA*$^{E12\Delta13}$ had significantly decreased expression of *SLC7A5* (0.1-fold) and *SLC3A2* (0.2-fold) compared to WT. *indicates $p<0.05$.

Supplemental Table 1
sgRNA sequences for *MUT and PCCA*

Gene	Exon	sgRNA1 (5' – 3')	sgRNA2 (5' – 3')
MUT	5	CACACTGTCAGACATCTGGA (TGG)	CCTAAAAACTCAAAATCTCT (TCT)
PCCA	12	TGGGACCGTGGAGTTCCTTG (TGG)	CCAGAGCAGTAAAATATTCC (TCT)

*The upstream PAM sequences, not included in the guide sequence, are highlighted in red.

Supplemental Table 2
Primer sequences for Surveyor Assay screening and sequencing of edited clones

Gene	Exon	Forward Primer (5' – 3')	Reverse Primer (5' – 3')
MUT	5	TGTACGTGCACTGATCTTAATTC	TTAACCACCAGAGGGAGACAA
PCCA	12	AAAGTTGACTTATTTGAGCATGTTATG	GATGTCTTAGCACAAGCATAAAAAC

Supplemental Table 3
qRT-PCR Primer sequences for mRNA expression in HEK293 cells

Gene	Forward (5' – 3')	Reverse (5' – 3')
SLC3A2	CTGGTGCCGTGGTCATAATC	TGCTCAGGTAATCGAGACGCC
SLC7A5	TCATCATCCGGCCTTCATCG	TCACGCTGTAGCAGTTCACG
PSAT1	TCTACGTCATGGGCTTGGTTC	TCTTGCTTCTATTTTGGGGCTC
CBS	GGGTCCCCAGAGGATAAGGA	GGGGTGTCCCCGATTTTCTT
ASNS	TGTTGGATGGTGTGTTTGCAT	TCGCGGAGTGCTTCAATGTA
S18	CGGCGACGACCCATTCGAAC	GAATCGAACCCTGATTCCCCGTC

Supplemental Table 4A
Significantly enriched GO terms and KEGG pathways identified by DAVID analysis of proteins with reduced abundance in fibroblast cells from individuals with methylmalonic acidemia (MMA).

Term	P-Value
GO Terms, Biological Process	
extracellular matrix disassembly	1.00E-04
oxidation-reduction process	2.70E-04
cyclooxygenase pathway	1.60E-03
autophagy	9.10E-03
response to vitamin B1	1.20E-02
positive regulation of reactive oxygen species metabolic process	1.40E-02
response to hypoxia	2.10E-02
negative regulation of extracellular matrix disassembly	2.40E-02
negative regulation of cell proliferation involved in contact inhibition	2.40E-02
renal absorption	2.40E-02
cell-cell adhesion	2.60E-02
muscle contraction	2.80E-02
response to oxidative stress	3.00E-02
positive regulation of adaptive immune response	3.00E-02
proteolysis	3.40E-02
proteolysis involved in cellular protein catabolic process	3.50E-02
doxorubicin metabolic process	4.80E-02
response to selenium ion	4.80E-02
daunorubicin metabolic process	4.80E-02
response to calcium ion	4.90E-02
KEGG Pathways	
Pyruvate metabolism	3.80E-03
Valine, leucine and isoleucine degradation	6.00E-03
Amino sugar and nucleotide sugar metabolism	6.40E-03
Arachidonic acid metabolism	1.30E-02
Histidine metabolism	1.40E-02
Metabolic pathways	2.60E-02
Pentose and glucuronate interconversions	3.30E-02
Tryptophan metabolism	4.00E-02
Fatty acid degradation	4.80E-02

Supplemental Table 4B
Significantly enriched GO terms and KEGG pathways identified by DAVID analysis of proteins with increased abundance in fibroblast cells from individuals with methylmalonic acidemia (MMA).

Term	P-Value
GO Terms, Biological Process	
cellular amino acid biosynthetic process	1.10E-04
response to virus	7.50E-03
negative regulation of cell proliferation	1.40E-02
hydrogen sulfide biosynthetic process	1.40E-02
nuclear transport	1.80E-02
transsulfuration	1.80E-02
establishment of integrated proviral latency	2.90E-02
organ morphogenesis	4.40E-02
neutral amino acid transport	4.60E-02
KEGG Pathways	
Biosynthesis of amino acids	2.30E-03
Cysteine and methionine metabolism	8.20E-03
Metabolic pathways	2.30E-02
Biosynthesis of antibiotics	4.00E-02
Glycerophospholipid metabolism	4.60E-02

Supplemental Table 4C
Significantly enriched GO terms and KEGG pathways identified by DAVID analysis of proteins with reduced abundance in fibroblast cells from individuals with propionic acidemia (PA).

Term	P-Value
GO Terms, Biological Process	
extracellular matrix disassembly	8.10E-05
response to hypoxia	5.10E-04
oxidation-reduction process	2.40E-03
positive regulation of osteoblast differentiation	5.20E-03
branched-chain amino acid catabolic process	5.40E-03
protein localization	5.40E-03

memory	5.70E-03
response to cadmium ion	9.30E-03
angiogenesis	9.90E-03
response to vitamin B1	1.20E-02
positive regulation of I-kappaB kinase/NF-kappaB signaling	1.50E-02
positive regulation of vasoconstriction	1.50E-02
apoptotic process	1.80E-02
protein homooligomerization	2.00E-02
negative regulation of cell proliferation involved in contact inhibition	2.30E-02
valine catabolic process	2.30E-02
negative regulation of extracellular matrix disassembly	2.30E-02
negative regulation of protein ubiquitination	2.40E-02
response to oxidative stress	2.70E-02
proteolysis	2.70E-02
cellular response to lipopolysaccharide	2.80E-02
peripheral nervous system axon regeneration	2.90E-02
positive regulation of adaptive immune response	2.90E-02
cellular response to amino acid stimulus	3.10E-02
proteolysis involved in cellular protein catabolic process	3.20E-02
response to drug	3.30E-02
leukocyte migration	3.50E-02
defense response to Gram-negative bacterium	4.10E-02
response to calcium ion	4.50E-02
response to mechanical stimulus	4.70E-02
KEGG Pathways	
Proteoglycans in cancer	1.40E-04
Valine, leucine and isoleucine degradation	4.60E-04
Glyoxylate and dicarboxylate metabolism	1.90E-02
Protein digestion and absorption	3.10E-02
Pyruvate metabolism	3.90E-02
Metabolic Pathways	4.50E-02
Fatty acid degradation	4.60E-02

Supplemental Table 4D
Significantly enriched GO terms and KEGG pathways identified by DAVID analysis of proteins with increased abundance in fibroblast cells from individuals with propionic acidemia (PA).

Term	P-Value
GO Terms, Biological Process	
extracellular matrix organization	3.90E-04
cell adhesion	3.90E-04
cellular amino acid biosynthetic process	7.10E-03
glycosaminoglycan metabolic process	8.80E-03
cell migration	1.00E-02
cell-cell adhesion	1.00E-02
amino acid transport	1.30E-02
adherens junction organization	1.40E-02
muscle contraction	1.50E-02
collagen fibril organization	1.60E-02
hydrogen sulfide biosynthetic process	1.90E-02
transsulfuration	2.40E-02
heterophilic cell-cell adhesion via plasma membrane cell adhesion molecules	2.50E-02
cerebral cortex development	3.10E-02
regulation of cell shape	3.10E-02
elastic fiber assembly	3.40E-02
cardiac muscle fiber development	3.80E-02
KEGG Pathways	
Focal Adhesion	3.30E-02
Vascular smooth muscle contraction	3.30E-02
Biosynthesis of antibiotics	3.60E-02
Metabolic pathways	4.80E-02
Cell adhesion molecules (CAMs)	5.10E-02
Biosynthesis of amino acids	7.10E-02

Chapter 3

Barth syndrome cellular models have dysregulated respiratory complex I and mitochondrial quality control due to abnormal cardiolipin

This original article has been published and was reprinted with permission: Anzmann AF, Sniezek OL, Pado A, Busa V, Vaz FM, Kreimer SD, Cole RN, Le A, Kirsch BJ, Claypool SM, Vernon HJ (2021) Barth syndrome cellular models have dysregulated respiratory chain complex I and mitochondrial quality control due to abnormal cardiolipin. bioRxiv doi: https://doi.org/10.1101/2021.01.06.425502

3.1 Abstract

Objectives: Barth syndrome (BTHS) is an X-linked genetic condition caused by defects in *TAZ*, which encodes a transacylase involved in the remodeling of the inner mitochondrial membrane phospholipid, cardiolipin (CL). CL has been implicated in numerous mitochondrial functions, and the role of defective CL in the clinical pathology of BTHS is under intense investigation.

Methods: We used untargeted proteomics, shotgun lipidomics, gene expression analysis, and targeted metabolomics to identify novel areas of mitochondrial dysfunction in a new model of TAZ deficiency in HEK293 cells.

Results: Functional annotation analysis of proteomics data revealed abnormal regulation of mitochondrial respiratory chain complex I (CI), driven by the reduced abundance of 6 CI associated proteins in TAZ-deficient HEK293 cells: MT-ND3, NDUFA5, NDUFAB1, NDUFB2, NDUFB4, and NDUFAF1. This resulted in reduced assembly and function of CI in TAZ-deficient HEK293 cells as well as BTHS patient derived lymphoblast cells. We also identified increased abundance of PARL, a rhomboid protein involved in the regulation of mitophagy and apoptosis, and abnormal downstream processing of PGAM5, another mediator of mitochondrial quality control, in TAZ-deficient cells. Lastly, we modulated CL via the phospholipase inhibitor bromoenol lactone and the CL targeted SS-peptide, SS-31, and showed that each is able to remediate abnormalities in CI abundance as well as PGAM5 processing.

Conclusions: Mitochondrial respiratory chain CI and PARL/PGAM5 regulated mitochondrial quality control, both of whose functions localize to the inner mitochondrial membrane, are dysregulated due to TAZ deficiency and are partially remediated via modulation of CL.

3.2 Introduction

Barth syndrome (BTHS, MIM#302060) is a rare X-linked inborn error of mitochondrial phospholipid metabolism caused by variants in the gene *TAFAZZIN* (*TAZ*) [1-3]. *TAZ* encodes a transacylase essential for the remodeling and maturation of the mitochondrial phospholipid cardiolipin (CL) [1,4]. CL, primarily localized to inner mitochondrial membrane, has many key functions, including roles in maintaining mitochondrial cristae

structure, organization of respiratory complexes, protein import, fusion, fission, and cellular signaling [1]. TAZ deficiency results in abnormal CL content, including an accumulation of the remodeling intermediate monolysocardiolipin (MLCL), decreased remodeled CL, and a shift towards saturated CL species [1,5]. An elevated MLCL:CL ratio is the pathognomonic metabolic defect in BTHS and is found in 100% of affected individuals [6].

BTHS is a multisystem disorder characterized by prenatal onset of left ventricular noncompaction, early onset cardiomyopathy, skeletal myopathy, growth abnormalities, and neutropenia among other features, and is the only known Mendelian disorder of CL metabolism [1, 7-9]. Despite knowledge of the primary metabolic defect in BTHS, there is limited knowledge of downstream mechanisms of cellular pathogenesis, and consequently there is a dearth of targets for therapeutic intervention and clinical monitoring [10]. In addition to BTHS, CL abnormalities have been described in common conditions such as idiopathic cardiomyopathy, fatty liver disease, and diabetes [1, 11-14]. Consequently, studies in BTHS have the potential to illuminate pathophysiology in a range of common diseases.

To identify novel and unappreciated cellular pathways impacted by TAZ deficiency we employed a discovery-based approach in a new HEK293 TAZ-deficient cellular model, starting with untargeted proteomics followed by functional analysis, and validation of pathways of interest in both HEK293 TAZ-deficient cells and patient-derived lymphoblastoid cell lines (LCLs). With this approach we characterized two major areas of dysfunction in the inner mitochondrial membrane: complex I (CI) of the mitochondrial respiratory chain and mitochondrial quality control (MQC).

Prior studies seeking to define the mitochondrial pathology of TAZ deficiency have described abnormal assembly and function of the mitochondrial respiratory complexes [15-17]. In agreement with these findings, we identified aberrations in mitochondrial respiratory chain protein abundance and enzymatic function, specifically in CI. Significantly, our findings show that TAZ deficiency results in the reduced CI mRNA expression with evidence for distinct regulation in differing cell types.

In addition to expanding our current understanding of respiratory chain abnormalities in TAZ deficiency, we also identified novel abnormalities in regulators of MQC. We uncovered aberrant abundance of the MQC protein PARL, which was accompanied by altered cleavage of the downstream MQC mediator and PARL target, PGAM5. PGAM5 cleavage abnormalities were further amplified by uncoupling of mitochondrial oxidative phosphorylation, suggesting that baseline MQC abnormalities in TAZ-deficient cells can be exacerbated with additional stress.

Finally, we found that modulating CL normalizes gene expression of CI subunits, normalizes the abundance of CI holoenzyme, and remediates the aberrant ratio of cleaved to full length PGAM5. Thus, abnormal CL in TAZ deficiency has a direct role in dysregulating both CI of the mitochondrial respiratory chain and MQC.

3.3 Methods

Cell lines and culture conditions.

HEK293 WT cells were purchased from ATCC (293 [HEK-293]x ATCC® CRL-1573™). Collection of control (LCL Control #1) and BTHS patient (LCL BTHS #1-5) derived LCL

lines had institutional IRB approval via Johns Hopkins University protocols #IRB00098987 (Table S11). Individuals were diagnosed with BTHS via an increased MLCL:CL ratio. Additional control LCL lines (n=9) were acquired through the following sources: Biochemical Genetics Laboratory at Kennedy Krieger Institute (LCL Control #2-3), Valle Laboratory (LCL Control #4-5), Coriell NINDS Biobank (LCL Control #6-9) (Table S11).

LCL lines were transformed by the Biochemical Genetics Laboratory at Kennedy Krieger Institute and the Valle Laboratory used the following protocol. Peripheral blood samples were centrifuged for 15 minutes at 3000 rpm. The "buffy coat" was then resuspended in RPMI and further centrifuged for 10 minutes at 1000 rpm. The resulting cell pellet was resuspended in RPMI and incubated with Epstein-Barr (EB) virus and T-cell growth factor (TCGF) at 37C for 48-72 hours. After incubation period, additional RPMI was added to the flask. Cells were monitored and fed RMPI for two weeks, after which the established transformed cell lines were passaged for experiments and/or freezing. LCL lines acquired through the Coriell NINDS Biobank were also transformed via EB virus.

All cells were grown at 37°C, 5% CO2. HEK293 WT and *TAZ*$^{\Delta 45}$ were maintained in DMEM with L-glutamine and 4.5 g/L Glucose (Corning Cellgro Cat. #10-017) containing 10% fetal bovine serum (FBS, Gemini) and 2 mM L-glutamine (Gibco, Cat. #25030149). Patient derived lymphoblastoid cells (LCLs) were maintained in RPMI 1640 (Gibco, Cat. # 11875119) containing 10% FBS (Gemini). Mycoplasma contamination was routinely monitored and not detected.

For CCCP treatment, HEK293s were seeded into 6-well plates. At confluence, cells were either treated with 20uM CCCP (Sigma, Cat. #C2759) for 0,10,30,60,90, and 120 mins, or 0,10,20,40,80,100uM CCCP for 45 mins.

For BEL treatment, HEK293s (400K) were seeded into 6-well plates. 48hrs later, at 80-90% confluence, cells were treated with 2.5uM BEL (Sigma, Cat. #B1552) for 48hrs.

For SS-31 treatment, HEK293s (50K) were seeded into 6-well plates. For 7 days, cells were fed fresh 100nM SS-31 (Provided by Stealth Therapeutics).

CRISPR/Cas9 genome editing

sgRNAs (Figure S1 & Table SI) targeting exon 2 of *TAZ* were designed at www.crispr.mit.edu and selected based on the scoring algorithm detail in Hsu et al. 2013 (Table S1) (55, 56). Synthesized sgRNA 1 and sgRNA 2 were individually cloned into pSpCas9(BB)-2A-Puro (PX459) V2.0 vector pSpCas9(BB)-2A-Puro (PX459) V2.0 was a gift from Feng Zhang (Addgene plasmid # 62988 ; http://n2t.net/addgene:62988 ; RRID:Addgene_62988 (55). HEK293 WT cells were transfected with both sgRNA vectors using Lipofectamine 2000 (Invitrogen). 24-hours after transfection cells were subjected to Puromycin selection (2ug/mL) for approximately 48 hours. Following selection, cells we passaged in order to isolate single cell clones. Confluent colonies of single cell clones were collected using a cloning cylinder and expanded for DNA isolation and screening.

Screening and genotyping

Genomic DNA was extracted from an aliquot of 3 x 10^6 cells using the Gentra Purgene Kit (Qiagen). The genomic region surrounding the CRISPR/Cas9 target site (741 bp) was PCR amplified using AccuPrime GC-Rich DNA Polymerase (Invitrogen) (Table S1). The PCR

product was then used for screening with Surveyor Assay Kit (IDT). The PCR product of Surveyor-Positive clones was further analyzed by Sanger sequencing.

RT-PCR

RNA was extracted from an aliquot of 3 x 10^6 cells using the RNeasy Plus Kit (Qiagen). cDNA was synthesized from extracted RNA using the iScript cDNA Synthesis Kit (BioRad). The region surrounding the CRISPR/Cas9 target site was PCR amplified using AccuPrime GC-Rich DNA Polymerase (Invitrogen) (Forward Primer: 5' TACATGAACCACCTGACCGT 3', Reverse Primer: 5' CAGATGTGGCGGAGTTTCAG 3'). PCR products were resolved on a 0.8% agarose gel.

Whole Cell Lysate Extraction

An aliquot of 3 x 10^6 cells was centrifuged for 4 minutes at 1000rpm. The resultant cell pellet washed twice with ice-cold PBS and lysed with RIPA lysis buffer (1% (v/v) Triton X-100, 20 mm HEPES–KOH, pH 7.4, 50 mm NaCl, 1 mm EDTA, 2.5 mm $MgCl_2$, 0.1% (w/v) SDS) spiked with 1 mm PMSF for 30 min at 4°C with rotation. Insoluble material was removed by centrifugation for 30 min at 21000g at 4°C, the supernatant collected, and protein quantified using a bichichronic acid (BCA) assay (Pierce).

Mitochondrial Isolation

Mitochondrial isolation of HEK293s was performed as previously described by Lu et al.[3]. Mitochondrial isolation of LCLs was also performed as previously described, with slight modification. LCLs were grown in maintenance media until total cell count exceeded 100 x 10^6 cells. LCLs were then centrifuged for 4 minutes at 1000rpm before beginning the previously described protocol by Lu et al. [3].

Immunoblotting

Whole cell extracts or mitochondria, resuspended in XT Sample Buffer (BioRad) and Reducing Agent (BioRad), were resolved on Criterion XT 12% Bis-Tris gels (BioRad) in XT MOPS Running buffer (BioRad). Proteins were transferred to Immuno-Blot PVDF (BioRad) at 100V for 1 hour. Following transfer, membranes were blocked with 5% milk, 0.05% Tween-20 in PBS (Blocking Buffer) for 1 hour at room temperature or at 4C if longer, with rocking. Following blocking, membranes were briefly washed with PBST (PBS with 0.2% Tween-20) and then incubated with primary antibody in PBST with 0.02% Na-Azide overnight at 4C with rocking. Following three successive 10-minute washes with PBST at room temperature, HRP-conjugated secondary antibodies were added and incubated for 45 min at room temperature. The membranes were then washed three times for 10 minutes with PBST and twice for 10 minutes with PBS. Immunoreactive bands were visualized using ECL Western Blotting Detection (Amersham) or SuperSignal West Pico PLUS (Pierce). Images were captured with a Fluorchem Q (Cell Biosciences, Inc.) or on film. Film was scanned before quantification. Quantitation of bands was performed using ImageJ and protein expression values were normalized to loading controls.

Antibodies

Antibodies against the following proteins were used; β-actin (loading control, Life Technologies #AM4302), GRP75 (loading control, 75-127), TAZ (#2C2C9, Epitope: 237-TDFIQEEFQHL, exon 11)[3], NDUFAF1 (Abcam, #ab79826), PARL (Abcam #ab45231, Proteintech #26679-1-AP, Langer Laboratory), UQCRC2 (Abcam, #ab14745), NDUFA9 (Abcam, #ab14713), NDUFS3 (Abcam, #ab110246), NDUFB6 (Abcam, #ab110244). Two

HRP-conjugated secondary antibodies were used; goat anti-rabbit (Abcam, #ab6721), goat anti-mouse (Abcam, #ab205719).

Lipidomics

Lipids were extracted from cell pellets (3 x 10^6 cells) and analyzed as previously described by Vaz et al. [57].

Proteomics

Samples (HEK293 WT n=3, and TAZ$^{\Delta 45}$ n=3, serial passages) were reduced in 5 mM DTT for 1 hour at 56C, alkylated in 10 mM iodoacetamide for 30 minutes in the dark at room temperature, and precipitated in cold (-20C) acetone 10% trichloroacetic acid. The precipitate was pelleted by centrifugation at 16,000 g for 15 minutes, the supernatant was discarded, and the pellet was rinsed with cold acetone and dried at room temperature. The samples were reconstituted in 50 µL of 20% acetonitrile 80 mM triethyl ammonium bicarbonate (TEAB) and digested with 3.3 µg of trypsin/Lys-C mix (Promega) at 37C overnight. The digested samples were labeled with TMT 10-plex reagent (Thermo, Lot #SK257889) and combined. The sample was lyophilized and reconstituted in 0.5 mL of 10 mM TEAB and fractionated by high (8-9) pH reversed phase chromatography into 84 fractions which were concatenated into 24. Each of the 24 fractions was lyophilized and reconstituted in 2% acetonitrile 0.1% formic acid and separated over a 90-minute low (2-3) pH reversed phase gradient (120 minutes run time) for mass spectrometry (MS) analysis on an Orbitrap Fusion.

MS data were acquired using serial data-dependent fragmentation of individual precursor ions (DDA). An intact precursor ion scan (MS1) spanning 400 - 1600 Th was acquired every 3 seconds at a resolution of 120,000 (at m/z = 200). Fragmentation scans

(MS2) were acquired at 60,000 resolution between precursor scans by isolation of individual precursor ions at 0.6 Th resolution, accumulation to 5 $x10^4$ automatic gain control for a maximum injection time of 250 ms, and activation with beam collision (HCD) at 38% energy. Mass accuracy was maintained throughout the experiment by internal calibrant lock mass.

The acquired data were searched against the SwissProt Human database by MASCOT using 4 ppm and 0.01 Da precursor and fragment maximum mass error, respectively. TMT labeled lysine and peptide N-termini and carbamidomethylation of cysteine were set as static modifications. Oxidation of methionine and deamidation of asparagine and glutamine were set as dynamic modifications. The results were rescored by Percolator in Proteome Discoverer 2.2 and quantitative analysis was carried out based on reporter ion intensities.

Functional Annotation

We selected proteins with a protein abundance fold change (FC, $TAZ^{\Delta 45}$/ WT) less than or equal to 0.80 (FC $\leq$ 0.80) and proteins with a FC greater than or equal to 1.2 (FC $\geq$ 1.20). Each subset was individually uploaded to DAVID 6.8 and compared to the background "Homo sapiens" [18-19]. With the functional annotation tool, we pulled all KEGG pathways and GO terms for further analysis.

Quantitative RT-PCR

Total RNA was extracted from an aliquot of 3 x 106 cells using the RNeasy Plus Kit (Qiagen). cDNA was synthesized from extracted RNA using the iScript cDNA Synthesis Kit (BioRad) in 20 µl reactions according to the manufacturer's suggested protocol using 1 ug of RNA. cDNA was subsequently diluted 10-fold with water. 2.4 µl of cDNA was

analyzed in 12 µl reactions using the SsoAdvanced Universal SYBR Green Supermix (Bio-Rad) according to the manufacturer's instructions and included each respective forward and reverse gene-specific primers (Table S12). Each sample-primer reaction was plated in triplicate per plate. Each plate also included both no reverse-transcriptase controls (No-RT) for each cDNA sample and no template controls (No-Template) for each primer pair. The reaction conditions were as follows: 2 min at 95°C, followed by 40 two-temperature cycles of 5 s at 95°C and 30 s at 60°C. For nuclear genes, expression of each gene was analyzed by the comparative CT (ΔΔCT) method with *TBP* and *HPRT1* being averaged as endogenous reference genes. For mitochondrial genes (*MT-ND3)*, expression of each gene was analyzed by the comparative CT (ΔΔCT) method with *MT-RNR1*, *MT-CO1*, and *MT-ATP6* being averaged as endogenous reference genes. Values were represented as average fold change relative to respective wildtype or untreated controls.

1D BN-PAGE

Cell pellets (100,000 cells, ~120ug) were solubilized for 30 min on ice in 20 mm Bis-Tris, 10% glycerol, 50 mM NaCl, supplemented with 1% (v/v) Triton X-100 and protease inhibitors (PMSF, Leupeptin, Pepstatin). Extracts were clarified by centrifugation for 30 min at 21 000g at 4C and analyzed by 1D BN/SDS–PAGE as described by Claypool et al. [58].

Complex I and II activity assays

The activity of complex I was measured using the Complex I Enzyme Activity Microplate Assay Kit (Abcam, #ab109721) according to the manufacturer's instructions using 200ug of isolated mitochondria for both HEK293s and LCLs. The activity of complex II was measured using the Complex II Enzyme Activity Microplate Assay Kit (Abcam,

#ab109908) according to the manufacturer's instructions using 200ug of isolated mitochondria for both HEK293s and LCLs.

NDUFAF1 Transfection

HEK293 cells were seeded into 15 cm plates. When cells reached ~80% confluency cells were transiently transfected with *NDUFAF1*(NM_016013) C-Myc/DDK-tagged plasmid (Origene #RC200029) with Lipofectamine 3000 (Thermo #L3000001) according to manufacturer's instructions. 75.4 ug of plasmid was transfected with 105 uL of Lipofectamine 3000 per 15 cm plate. The cells were grown in galactose media for 48hrs before mitochondria extraction performed as described previously.

Metabolomics

HEK and LCL cell samples undergoing metabolic analysis were initially kept on ice and washed with ice-cold PBS prior to collection, followed by centrifugation at 1500RPM and 4°C. Metabolites within the cell pellet were extracted with 80% HPLC-grade methanol (Fisher Scientific) and 20% mass-spec (MS)-grade water as previously described (59). The extraction solution was then collected and evaporated using a speed-vac and a lyophilizer which resulted in a white powder of dried metabolites. The collected metabolites were subsequently resuspended in 50% (vol/vol) acetonitrile diluted with MS-grade water and analyzed via an Agilent 1260 HPLC and 6490 triple-quadrupole (QQQ) mass spectrometer.

The Agilent 1260 HPLC-autosampler system was kept at 4°C for the entirety of the run to prevent any degradation within the samples. Optimal separation was achieved with a reverse phase chromatography system with an aqueous mobile phase of MS-grade water with 0.1% formic acid and an organic mobile phase of 98% acetonitrile with 0.1% formic acid. The Discovery® HS F5 HPLC Column (3µm particle size, L × I.D. 15 cm × 2.1 mm,

Sigma) with a compatible guard column (Sigma) were used and maintained at a temperature of 35°C. The injection volume was 2µL and the runtime was 50 minutes per sample. The flow rate, buffer gradient, and mass spectrometer parameters for the method were the same as previously described [60].

Data from pure standards of each compound of interest were acquired prior and simultaneously with samples in identical setting: precursor and product ion transitions, collision energy, and ion polarity. Agilent MassHunter and Agilent Qualitative and Quantitative Analysis Software packages were used to analyze the metabolic profiles. The metabolite peaks were integrated for raw intensities and then normalized by protein concentration collected from the original cell pellet. Protein concentration was determined using a FilterMax F5 microplate reader and a Bovine Serum Albumin (BSA) standard.

Data Analysis

All statistical analyses were performed using R version 3.3.2 (2016-10-31) [61]. Between-group comparisons were performed using Welch's two-sample t-test. Outliers, outside 1.5x the interquartile range above the upper quartile and below the lower quartile were only removed for statistical analyses of the isogenic HEK293 cell lines.

3.4 Results

Generation of a HEK293 TAZ-deficient model, $TAZ^{\Delta 45}$

We used CRISPR/Cas9 genome editing in HEK293s to create a novel TAZ-deficient cellular model. Using two single guide RNAs (sgRNAs) targeting exon 2 of *TAZ*, we isolated 3 individual clones with a resultant 45bp deletion at the 3'- end of exon 2; $TAZ^{\Delta 45.4}$,

TAZ$^{\Delta 45.5}$, *TAZ*$^{\Delta 45.6}$ (Fig. S1). The deletion encompasses a predicted acyltransferase domain and covers an area of *TAZ* where multiple pathological variants have been described, such as p.R57L and p.H69Q (Fig. S1) [3]. The 45bp in-frame deletion is not predicted to result in NMD (Fig. 1A). However, the deletion resulted in undetectable expression of TAZ in all three clones (Fig. 1B). In the absence of TAZ there was no significant difference in the abundance of cytosolic and mitochondrial proteins/immunoblotting controls; GRP75, ß-actin, VDAC1, and TOM20 (Fig. S2).

Shotgun lipidomics via mass spectrometry revealed a significant decrease in CL, a significant increase in MLCL, and a significantly increased MLCL:CL ratio ($p=0.03$, $p=4.9 \times 10^{-5}$, $p=4.6 \times 10^{-6}$, respectively) (Fig. 1C). TAZ-based remodeling is characterized by the incorporation of unsaturated acyl chains compared to nascent CL. Of the 31 CL species assessed, the *TAZ*$^{\Delta 45}$ clones had a significant increase in CL containing 1 to 3 double bonds ($p=0.007$, $p=1.5 \times 10^{-9}$, $p=7.4 \times 10^{-6}$, respectively) and a significant decrease in CL containing 4 to 6 double bonds ($p=0.03$, $p=0.003$, $p=4.2 \times 10^{-9}$, respectively), highlighting the loss of TAZ-based remodeling (Fig. 1D). Collectively, the *TAZ*$^{\Delta 45}$ clones recapitulate the pathognomonic metabolic defect of BTHS and validate the *TAZ*$^{\Delta 45}$ clones as TAZ-deficient cellular models of BTHS.

We amplified and Sanger sequenced 5 of the top 10 predicted off-target sites, 5 off-target sites per sgRNA, which revealed no detectable off-target CRISPR/Cas9 genome editing activity (Table S1). The other 5 off-target sequences were not able to be amplified likely due to highly repetitive sequences and/or increased GC base pair content. None of the top 10 predicted off-target sites were located in coding regions. In order to mitigate

consequences of undetected off-target editing in any one of the clones, the clones, *TAZ*$^{\Delta 45.4}$, *TAZ*$^{\Delta 45.5}$, *TAZ*$^{\Delta 45.6}$, were combined at a 1:1:1 ratio to create the cellular model *TAZ*$^{\Delta 45}$.

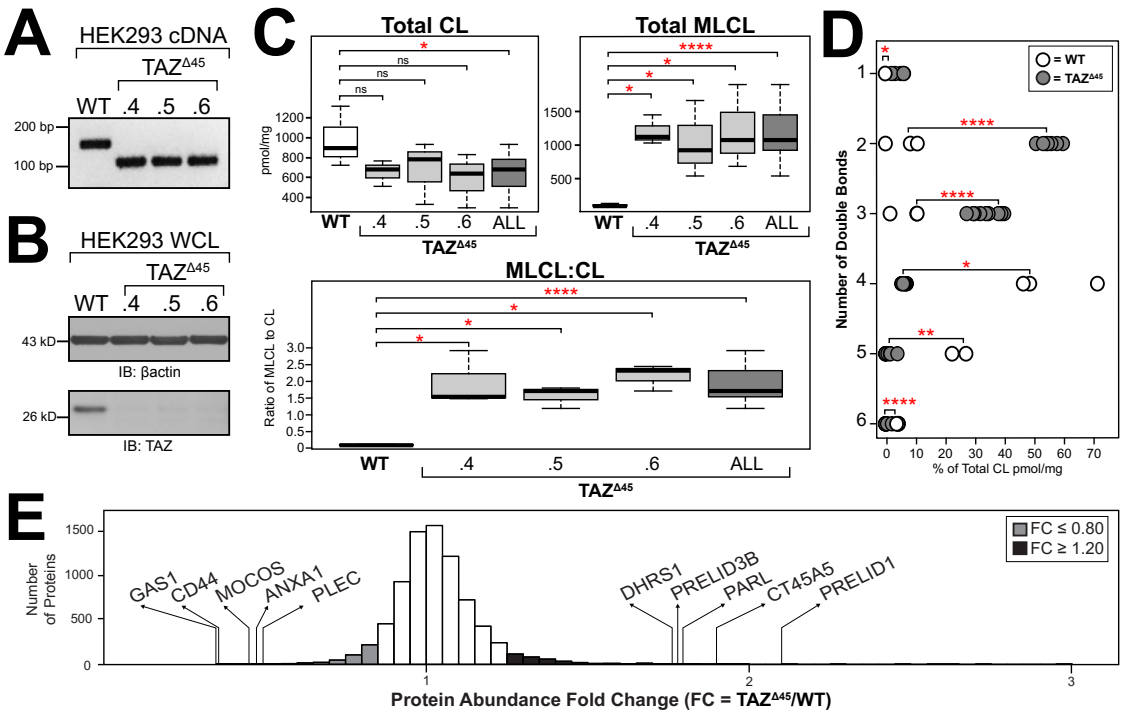

Figure 1. *TAZ*$^{\Delta 45}$ HEK293 genetic characterization, CL profiling and proteomics analysis. (A) RT-PCR of RNA extracted from the HEK293 *TAZ*$^{\Delta 45}$ clones using primers specific to the region of *TAZ* being edited. **(B)** Whole cells lysate (45ug) of the indicated cell lines immunoblotted for TAZ and loading control β-actin. **(C)** The abundance of CL and MLCL in WT (n=3) and *TAZ*$^{\Delta 45}$ clones (n=3, per clone) was determined by shotgun lipidomics via mass spectrometry. **(D)** The distribution of double bonds across CL species was determined as a percentage of total CL. **(E)** 7713 proteins were identified and quantified with TMT 10-plex mass spectrometry of whole cell lysate (200ug) of *TAZ*$^{\Delta 45}$ (n=3) and WT cells (n=3). Protein abundance fold change (FC) calculated by dividing the average abundance per protein identified in *TAZ*$^{\Delta 45}$ cells by WT average abundance per protein. The genes that encode the most significantly reduced proteins in *TAZ*$^{\Delta 45}$ cells are *GAS1* (FC=0.35, p=2.5 x 10-4), *CD44* (FC=0.367, p=6.6 x 10-4), *MOCOS* (FC=0.45, p=0.011), *ANAX1* (FC=0.478, p=0.01), and *PLEC* (FC=0.491, p=2.7 x 10-4). The genes that encode the most significantly increased proteins in *TAZ*$^{\Delta 45}$ cells are *PRELID1* (FC=2.125, p=8.4 x 10-4), *CT45A5* (FC=1.909, p=0.023), *PARL* (FC=1.815, p=0.016), *PRELID3B* (FC=1.795, p=3.9 x 10-4), and *DHRS1* (FC=1.774, p=0.016). Proteins with a fold change (FC) ≤ 0.80 are highlighted in grey (n=215) and proteins with a FC ≥ 1.20 are highlighted in black (n=621). Significant differences are indicated; * ≤ 0.05, ** ≤ 0.005, *** ≤ 0.0005, **** ≤ 0.00005.

Differentially abundant proteins in TAZ$^{\Delta 45}$ cells reveal downstream cellular dysfunction due to TAZ deficiency

Shotgun proteomics analysis identified a total of 7713 proteins in HEK293 WT and *TAZ*$^{\Delta 45}$ cells. To focus our downstream workflow on proteins with differential abundance between the WT and *TAZ*$^{\Delta 45}$ cells, we selected proteins with a protein abundance fold change (FC, *TAZ*$^{\Delta 45}$/ WT) less than or equal to 0.80 (FC $\leq$ 0.80) and proteins with a FC greater than or equal to 1.2 (FC $\geq$ 1.20) (Fig. 1E). Based on these criteria, there were a total of 836 differentially abundant proteins, 215 with a FC $\leq$ 0.80 and 621 with a FC $\geq$ 1.20 (Fig. 1E). Functional annotation of the differentially abundant proteins, with KEGG pathway and gene ontology (GO) term enrichment analysis, identified multiple pathways of interest in *TAZ*$^{\Delta 45}$ cells (Table S2A-B) [18-19].

We identified 86 significantly enriched ($p \leq 0.05$) KEGG pathways and GO terms for proteins with a FC $\leq$ 0.80, such as: oxidative phosphorylation ($p=2.7 \times 10^{-6}$), mitochondrial respiratory chain complex I assembly ($p=7.9 \times 10^{-5}$), mitochondrial chain complex I ($p= 2.1 \times 10^{-4}$), response to oxidative stress ($p=1.6 \times 10^{-3}$), NADH dehydrogenase (ubiquinone) activity ($p=2.1 \times 10^{-3}$), and metabolic pathways ($p=0.019$) (Table S2A). We identified 127 significantly enriched ($p \leq 0.05$) KEGG pathways and GO terms for proteins with a FC $\geq$ 1.20, such as: mitochondrion ($p=2.2 \times 10^{-4}$), metabolic pathways ($p=3.1 \times 10^{-3}$), positive regulation of apoptotic process ($p=4.2 \times 10^{-3}$), AMPK signaling pathway ($p=7.5 \times 10^{-3}$), response to oxidative stress ($p=9.3 \times 10^{-3}$) (Table S2B).

Functional annotation analysis: proteins of respiratory complex I and mitochondrial quality control

Defects in OXPHOS function have been previously described in BTHS, and consistent with these previous studies, we found that of the 86 terms significantly enriched for proteins with FC ≤ 0.80 in *TAZ*$^{\Delta 45}$ cells, 18 reference the mitochondrion and/or OXPHOS, including the OXPHOS KEGG pathway (Table S2A). Specifically, 11 proteins with a FC ≤ 0.80 are encoded by genes associated with the OXPHOS KEGG pathway (Fig. S3). Of these 11 proteins, 5 are subunits of complex I (CI) and the remaining 6 proteins are subunits of complex III, IV, and V (Fig. S3). When we further examined the 18 terms that reference the mitochondrion and/or OXPHOS, we found that 4 specifically reference CI of OXPHOS (Table S2A).

The enrichment of the CI-associated terms in our functional annotation analysis was driven by 7 proteins encoded by the genes: *MT-ND3, NDUFAF1, NDUFA5, NDUFAB1, NDUFB2, NDUFB4,* and *OXA1L* (Fig. 2A). Five are subunits of CI (*MT-ND3, NDUFA5, NDUFAB1, NDUFB2, NDUFB4*), one is a CI assembly factor (*NDUFAF1*), and one assists with inserting proteins into the mitochondrial membrane and has been implicated in CI biogenesis (*OXA1L*) [20-21]. In total, proteomics identified and quantified 56 CI associated proteins in WT and *TAZ*$^{\Delta 45}$ cells, and 45/56 had reduced abundance in *TAZ*$^{\Delta 45}$ cells (FC range=0.608-0.998) (Table S3). Together, the functional annotation analysis highlights a decreased abundance of proteins associated with complex I, further delineating a previously described pathway in BTHS.

When we analyzed the top five proteins with significantly increased abundance, we identified PARL as a candidate for further study due to its role in regulating mitochondrial

responses to stress, such as membrane depolarization and increased reactive oxygen species [22-24]. Additionally, dysregulation of PARL substrates has been implicated in cardiomyopathy and cardiac development, further highlighting the potential role of PARL dysregulation in BTHS [25-27]. Upon further investigation of the 127 terms significantly enriched for proteins with a FC > 1.20, we observed that 20 terms reference the mitochondrion or mitochondrial dynamics, including: metabolic pathways ($p=3.1 \times 10^{-3}$), positive regulation of the apoptotic process ($p=4.2 \times 10^{-3}$), and mitochondrial inner membrane ($p=5.2 \times 10^{-3}$) (Table S2B). The functional annotation analysis revealed other genes of interest due to their potential roles in apoptosis, lipid trafficking, and/or mitochondrial quality control (MQC), such as; *PRELID1*, *PRELID3B*, *CASP2*, *CASP7*, *CASP8*, and *CASP9* [28-30]. Together with the proteomics findings, the functional annotation analysis suggests an increased abundance of proteins involved in MQC, a pathway not previously described in BTHS.

Reduced complex I holoenzyme and activity in HEK293 TAZ$^{\Delta 45}$ cells and BTHS patient derived lymphoblastoid cells

To assess the biological significance of reduced CI associated proteins identified via proteomics, we further investigated CI subunit/holoenzyme mRNA expression, protein abundance, and function. We measured the relative mRNA expression of *NDUFAF1*, the most significantly reduced protein identified by proteomics (FC=0.797, p=0.004), in both HEK293 and BTHS patient derived lymphoblastoid cells (LCLs). In *TAZ*$^{\Delta 45}$ cells, *NDUFAF1* had reduced mRNA expression (0.80, $p=6.4 \times 10^{-4}$), whereas in BTHS LCLs there was no significant difference in mRNA expression (Fig. 2B).

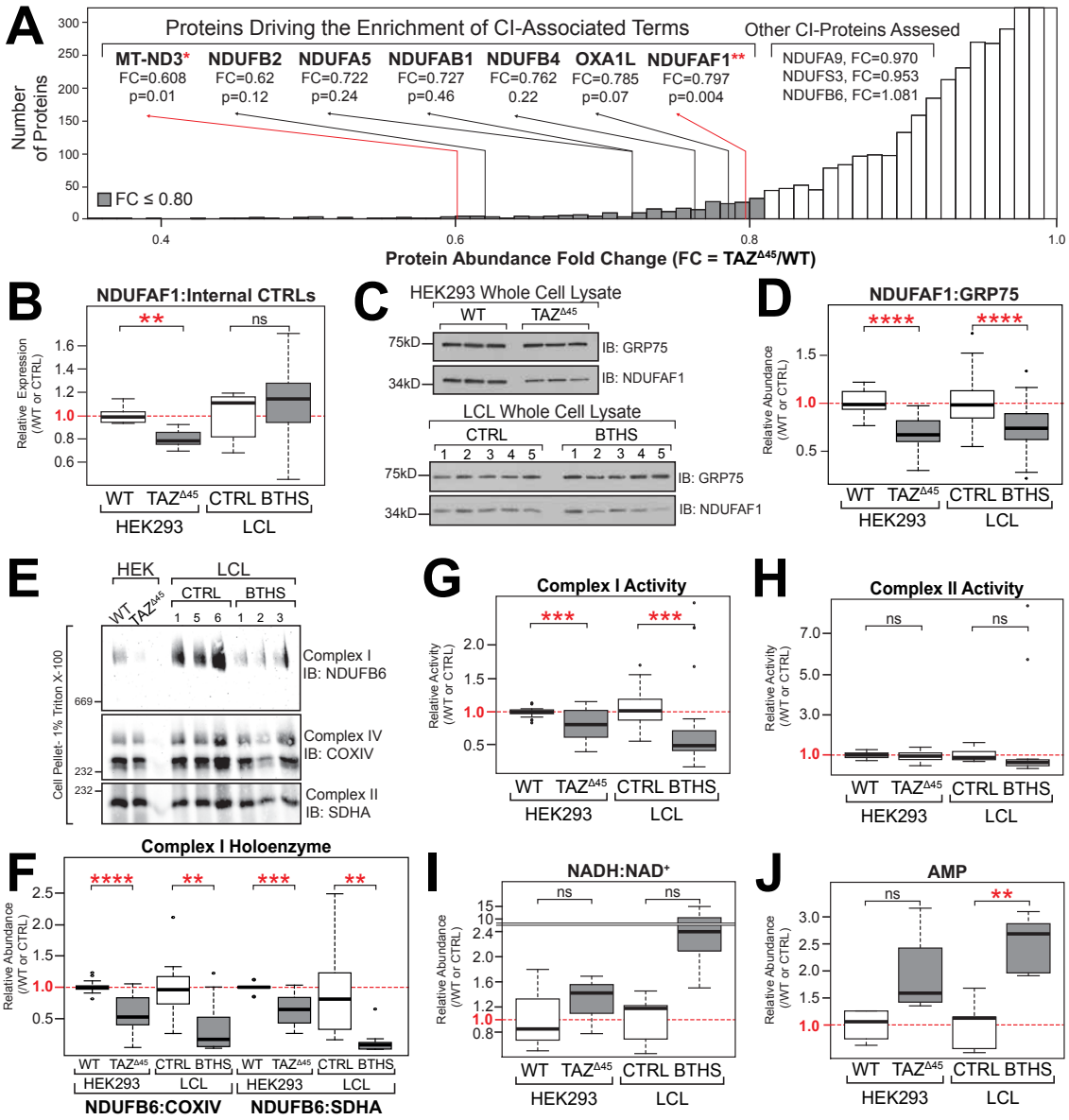

Figure 2. Reduced complex I (CI) holoenzyme abundance and activity in HEK293 *TAZ*$^{\Delta 45}$ cells and BTHS patient-derived lymphoblastoid cells. (A) The enrichment of the CI-associated terms is driven by 7 genes; *MT-ND3*, *NDUFAF1*, *NDUFA5*, *NDUFAB1*, *NDUFB2*, *NDUFB4*, *OXA1L*. **(B)** Relative mRNA expression of *NUDFAF1*, determined by qRT-PCR and $\Delta\Delta C_T$ quantification. Data plotted relative to WT/CTRL expression; WT n=6, *TAZ*$^{\Delta 45}$ n=6, CTRL n=10, BTHS n=15. **(C)** Whole cell lysate (45 ug) of the indicated lines were immunoblotted for the indicated proteins. **(D)** Band intensities, relative to the loading control GRP75, were quantified and plotted relative to WT/CTRL abundance; WT n=27, *TAZ*$^{\Delta 45}$ n=26, CTRL n=49, BTHS n=48. **(E)** BN-PAGE of HEK293 WT and *TAZ*$^{\Delta 45}$ or CTRL and BTHS LCL cells (100-250K cells) solubilized in 1% Triton X-100 immunoblotted for the indicated proteins. **(F)** Band intensities were quantified, and CI abundance was represented as the ratio of CI band intensity to CIV (COXIV) or CII (SDHA). Abundance was plotted relative to WT/CTRL abundance; CI:CIV (WT n=13,

TAZ$^{\Delta 45}$ n=16, CTRL n=12, BTHS n=12), CI:CII (WT n=10, *TAZ*$^{\Delta 45}$ n=13, CTRL n=9, BTHS n=9). **(G)** CI activity measured in HEK293 WT and *TAZ*$^{\Delta 45}$ or CTRL and BTHS LCLs mitochondria (200 ug total protein) on a microplate reader (450nm) by following the oxidation of NADH to oxidized nicotinamide adenine dinucleotide (NAD+). Activity plotted relative to WT/CTRL abundance; WT n=25, *TAZ*$^{\Delta 45}$ n=26, CTRL n=36, BTHS n=42. **(H)** CII activity measured in HEK293 WT and *TAZ*$^{\Delta 45}$ or CTRL and BTHS LCLs mitochondria (200 ug total protein) on a microplate reader by following the production of ubiquinol by CII coupled to the reduction of the dye diclorophenolindophenol (DCPIP, 600nm). Activity plotted relative to WT/CTRL abundance; WT n=12, *TAZ*$^{\Delta 45}$ n=12, CTRL n=10, BTHS n=12. Targeted metabolomics was used to measured **(I)** NADH, NAD+, and **(J)** cellular AMP via mass spectrometry in HEK293 WT (n=3), HEK293 *TAZ*$^{\Delta 45}$ (n=3), CTRL LCL (n=5) and BTHS LCL (n=5) cells. Significant differences are indicated; * ≤ 0.05, ** ≤ 0.005, *** ≤ 0.0005, **** ≤ 0.00005

We also measured the relative mRNA expression the 5 other CI associated proteins that had a FC ≤ 0.80 (MT-ND3, NDUFA5, NDUFB2, NDUFAB1, and NDUFB4), as well as 3 additional CI associated proteins (NDUFA9, NDUFS3, and NDUFB6), which did not have a FC ≤ 0.80 but had been previously shown to have reduced protein abundance in BTHS LCLs (Fig. S4) [17]. Of these 8 genes, 4 had significantly reduced mRNA expression in *TAZ*$^{\Delta 45}$ cells (*NDUFB2* p=0.04, *NDUFAB1* p=0.001, *NDUFB4* p=0.02, and *NDUFB6* p=0.01) (Fig. S4). *NDUFA5, NDUFA9,* and *NDUFS3* had reduced mRNA expression in *TAZ*$^{\Delta 45}$ cells but this reduction did not reach statistical significance (Fig. S4). There were no significant differences in the mRNA expression between control and BTHS LCLs, however there was significant variability in mRNA expression of all genes between the 5 individual BTHS LCL lines (Fig. S5). These individual differences could be due to the individual patient's genetic background or the EBV transformation of the LCLs and may obfuscate the biological significance of mRNA expression in patient-derived LCLs.

Immunoblotting of HEK293 and LCL whole cell lysate for NDUFAF1 confirmed reduced protein abundance in *TAZ*$^{\Delta 45}$ cells (FC=0.69, p=4.89 x 10^{-10}) and BTHS LCLs (FC=0.75, p=7.69 x 10^{-7}) (Fig. 2C-D). We also immunoblotted HEK293 and LCL

mitochondria for the 3 additional CI subunits that had been previously shown in a prior publication to have reduced protein abundance [17]. There was a subtle trend towards reduced NDUFA9, NDUFS3, and NDUFB6 abundance in *TAZ*$^{\Delta 45}$ cells (p=ns, p=0.04, p=0.05, respectively), and a strong reduction in BTHS LCLs ($p=7.6 \times 10^{-6}$, $p=1.8 \times 10^{-7}$, $p=5.1 \times 10^{-6}$, respectively) (Fig. S6). The abundance of NDUFA9, NDUFS3, and NDUFB6 in *TAZ*$^{\Delta 45}$ cells aligns with our proteomics findings, that found no significant difference in the abundance of these proteins between WT and *TAZ*$^{\Delta 45}$ cells (Fig. 2A, Fig. S6). In order to determine whether TAZ deficiency affected the protein abundance of subunits from other respiratory complexes, we also immunoblotted for UQCRC2, a subunit of respiratory complex III. We found no significant difference in UQCRC2 abundance between WT and *TAZ*$^{\Delta 45}$ cells, and a subtle but significantly reduced abundance of UQCRC2 in BTHS LCLs compared to controls (Fig. S6).

To determine the total abundance of CI holoenzyme, HEK293 and LCL cells were solubilized with Triton X-100 and resolved by BN-PAGE for the quantification of individual respiratory complexes. CI was the most significantly reduced complex, and the ratio of CI to CIV (CI:CIV) or CI:CII was significantly reduced in both *TAZ*$^{\Delta 45}$ vs. WT ($p=2.32 \times 10^{-5}$, $p=1.62 \times 10^{-4}$, respectively) and BTHS LCLs vs. controls (p=0.001, p=0.005, respectively) (Fig. 2E-F). Since NDUFB6 steady-state abundance was significantly reduced in BTHS LCLs (Fig. S6), it is difficult to interpret the LCL results, as the reduction could be due to reduced steady-state levels of NDUFB6 or an overall reduction of CI holoenzyme. By comparing starting material and the cellular pellet following solubilization via immunoblotting, we found no significant difference in the solubilization of *TAZ*$^{\Delta 45}$ and WT cells (87% and 88% solubilization efficiency,

respectively). There was a minimal though statistically significant difference in the solubilization of BTHS and control LCLs (84% and 79% solubilization efficiency, respectively, p=0.03). Therefore, the observed differences were not due to an effect of altered CL on Triton X-100 solubilization.

Using a colorimetric CI enzyme activity assay that detects the oxidation of NADH to NAD^+, we found a significant reduction in CI activity in both *TAZ*$^{\Delta 45}$ cells and BTHS LCLs ($p=9.4 \times 10^{-5}$ & $p=1.8 \times 10^{-4}$, respectively) (Fig. 2G). Using a colorimetric CII enzyme activity assay, we found no significant difference in CII activity between WT and *TAZ*$^{\Delta 45}$ cells or between control and BTHS LCLs, emphasizing the preeminent role of CI in BTHS-associated OXPHOS dysfunction (Fig. 2H). There was a wide range of CII function in LCLs derived from different individuals (Fig. S7). Overexpression of NDUFAF1, a CI assembly factor and the most significantly reduced CI associated protein in *TAZ*$^{\Delta 45}$ cells, did not normalize the CI functional deficiency in *TAZ*$^{\Delta 45}$ cells (Fig. S8A-B). The expression vector used was previously shown to produce a functional protein that is localized to the mitochondrion, which we confirmed with immunoblotting of isolated mitochondria for NDUFAF1 (Fig. S8C) [31]. This indicates that CI dysfunction is due to a combination of the reduced expression and abundance of CI subunits and assembly factors.

Measurement of intracellular NADH and NAD+ showed a trend towards an increase in the ratio of NADH to NAD^+ in both *TAZ*$^{\Delta 45}$ and BTHS LCLs compared to either WT or controls, though neither reached statistical significance (Fig. 2I). There was also an increase in intracellular AMP in both *TAZ*$^{\Delta 45}$ cells and BTHS LCLs compared to either WT or controls, with a significant increase in the BTHS LCLs (p=0.002) (Fig. 2J). This

moderate disturbance in energy homeostasis is consistent with the modest perturbations we observed in CI from mRNA expression, to protein expression, and ultimately activity in TAZ-deficient cells.

Increased PARL abundance correlates with increased cleavage of downstream target PGAM5

To confirm the proteomics finding of increased PARL abundance (FC=1.815, p=0.016) in TAZ-deficient HEK293 cells, we immunoblotted HEK293 and LCL whole cell lysate for PARL. Using a PARL-KO HEK293 cell line generously provided by the Langer Laboratory, we identified a single band at ~33kD present in both WT and *TAZ*$^{\Delta 45}$ cells and absent in the PARL-KO cells, consistent with the band representing the mature mitochondrial PARL (MAMP-PARL), referred to as PARL (Fig. S9) [24].

In *TAZ*$^{\Delta 45}$ cells there was a significant increase in the abundance of PARL (FC=1.51, p=1.81 x 10^{-10}) (Fig. 3A-B). There was a subtle but significant increase in the relative mRNA expression of *PARL* in *TAZ*$^{\Delta 45}$ cells (WT=0.97, *TAZ*$^{\Delta 45}$=1.09, p=0.02) (Fig. 3C). Immunoblotting of LCL whole cell lysate for PARL showed a significant reduction in PARL abundance, however, there was extreme variability in PARL abundance in the CTRL lines (CTRL 1-3 vs CTRL 4-5) (Fig. S10A). There was no significant difference in the mRNA expression of PARL between CTRL and BTHS LCLs or across the 5 different BTHS LCL lines (Fig. S10B-C). Thus, increased PARL in TAZ-deficient HEK293 cells may be regulated both at the transcriptional and protein expression levels, and lack of consistent findings in BTHS LCLs may be due to cell-type specific differences in PARL regulation or difficulty with detection in a small sample size due to high intra-subject

variability.

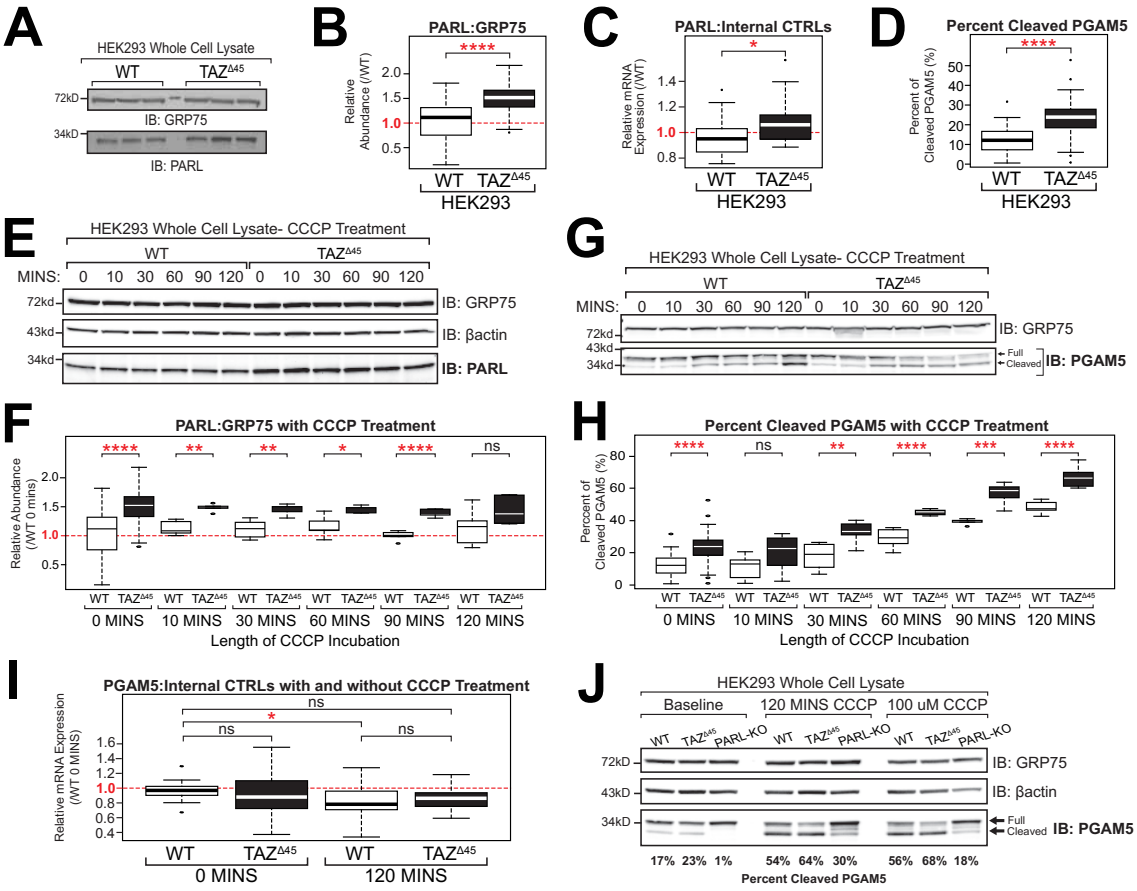

Figure 3. Increased cleavage of PGAM5 by PARL in HEK293*TAZ*$^{\Delta 45}$ cells. (A) Whole cell lysate (45 ug) of the indicated lines were immunoblotted for the indicated proteins. **(B)** Band intensities, relative to loading control GRP75, were quantified and plotted relative to WT abundance; WT n=54, *TAZ*$^{\Delta 45}$ n=48 **(C)** Relative mRNA expression of *PARL* determined by qRT-PCR and $\Delta\Delta C_T$ quantification; WT n=18, *TAZ*$^{\Delta 45}$ n=17. **(D)** Whole cell lysate (45 ug) of WT and *TAZ*$^{\Delta 45}$ cells were immunoblotted for PGAM5 and loading control GRP75. Band intensities, relative to the loading control GRP75, for both full-length and cleaved PGAM5 were individually quantified and plotted as the percent of cleaved PGAM5 (cleaved/full+cleaved); WT n=41, *TAZ*$^{\Delta 45}$ n=41. **(E)** HEK293 WT and *TAZ*$^{\Delta 45}$ cells were treated with 20uM CCCP for serial time points from 0 to 120 minutes. Whole cell lysate (45 ug) of the indicated lines and treatment times were immunoblotted for the indicated proteins. **(F)** Band intensities, relative to the loading control GRP75, were quantified and plotted relative to WT abundance; WT 0 mins n=54, WT 10 mins n=5, WT 30 mins n=6, WT 60 mins n=6, WT 90 mins n=5, WT 120 mins n=6, *TAZ*$^{\Delta 45}$ 0 mins n=48, *TAZ*$^{\Delta 45}$ 10 mins n=5, *TAZ*$^{\Delta 45}$ 30 mins n=5, *TAZ*$^{\Delta 45}$ 60 mins n=5, *TAZ*$^{\Delta 45}$ 90 mins n=5, *TAZ*$^{\Delta 45}$ 120 mins n=6. **(G)** HEK293 WT and *TAZ*$^{\Delta 45}$ cells were treated with 20uM CCCP for serial time points from 0 to 120 minutes. Whole cell lysate (45 ug) of the indicated lines and treatment times were immunoblotted for the indicated proteins. **(H)** Band intensities,

relative to the loading control GRP75, for both full-length and cleaved PGAM5 were individually quantified and plotted as the percent of cleaved PGAM5 (cleaved/full+cleaved); WT 0 mins n=41, WT 10 mins n=8, WT 30 mins n=8, WT 60 mins n=8, WT 90 mins n=5, WT 120 mins n=7, *TAZ*$^{\Delta 45}$ 0 mins n=41, *TAZ*$^{\Delta 45}$ 10 mins n=8, *TAZ*$^{\Delta 45}$ 30 mins n=7, *TAZ*$^{\Delta 45}$ 60 mins n=5, *TAZ*$^{\Delta 45}$ 90 mins n=7, *TAZ*$^{\Delta 45}$ 120 mins n=7. **(I)** Relative mRNA expression of *PGAM5* determined by qRT-PCR and $\Delta\Delta C_T$ quantification; WT 0 mins n=14, *TAZ*$^{\Delta 45}$ 0 mins n=16, WT 120 mins n=16, *TAZ*$^{\Delta 45}$ 120 mins n=16. **(J)** Whole cell lysate (45 ug) of the indicated lines were immunoblotted for the indicated proteins. Band intensities, relative to the loading control GRP75, for both full-length and cleaved PGAM5 were individually quantified, and the percent of cleaved PGAM5 (cleaved/full+cleaved) is indicated for each lane (n=1). Significant differences are indicated; * ≤ 0.05, ** ≤ 0.005, *** ≤ 0.0005, **** ≤ 0.00005.

To investigate the biological significance of increased PARL abundance in *TAZ*$^{\Delta 45}$ cells, we assessed a downstream proteolytic target of PARL, PGAM5. Previous evidence suggests that PGAM5 is cleaved by PARL and another stress-activated IMM protease, OMA1, in response to loss of mitochondrial membrane potential ($\Delta\Psi_m$) [32]. Cleaved PGAM5 is released into the cytoplasm to integrate multiple MQC pathways through reciprocal dephosphorylation of BCL-xL (to mediate apoptosis, in response to severe mitochondrial stress) and FUNDC1 (to mediate mitophagy, in response to moderate mitochondrial stress) [33-34]. Deficiency of PGAM5-mediated mitophagy results in the accumulation of damaged, abnormal mitochondria and increased reactive oxygen species (ROS) [33,35,36]. At baseline, we observed a significant increase in the percent of cleaved PGAM5 in *TAZ*$^{\Delta 45}$ cells ($p=1.5 \times 10^{-7}$) (Fig. 3D). There was no significant difference in the percent of cleaved PGAM5 between CTRL and BTHS LCLs (Fig. S10D)

Upon treatment with membrane depolarizer carbonyl cyanide m-chlorophenyl hydrazine (CCCP), with serial time point measurements, we observed that *TAZ*$^{\Delta 45}$ cells maintained a significantly greater abundance of PARL until the final timepoint of 120 mins (Fig. 3E-F, Table S4). This increase in PARL abundance with CCCP correlates with the increase in PGAM5 cleavage observed in both WT and *TAZ*$^{\Delta 45}$ cells (Fig. 3G-H, Table S5).

We observed an increase in the percentage of cleaved PGAM5 in WT cells and *TAZ*$^{\Delta 45}$ cells, where *TAZ*$^{\Delta 45}$ cells maintained a significantly greater percentage of cleaved PGAM5 at all time points tested (Fig. 3G-H, Table S5). The difference in the percentage of cleaved PGAM5 between WT and *TAZ*$^{\Delta 45}$ cells increased over time, from a 11% difference at 0 mins to a 18% difference at 120 mins (Fig. 3G-H, Table S5). Immunoblotting showed that the increased percent of cleaved PGAM5 in *TAZ*$^{\Delta 45}$ cells was largely due to reduction in full-length PGAM5 (Fig. 3G). We examined PGAM5 mRNA expression relative to WT and found no significant difference between WT and *TAZ*$^{\Delta 45}$ cells at 0 mins or 120 mins (Fig. 3I). There is a subtle but significant reduction in expression between WT at 0 mins and WT at 120 min (Fig. 3I). This suggests that the observed increase in the percent of cleaved PGAM5 in *TAZ*$^{\Delta 45}$ cells at baseline and with CCCP treatment may be due to the increased cleavage and degradation of PGAM5 rather than reduced biosynthesis of PGAM5.

We further demonstrated that PGAM5 cleavage was absent and reduced in PARL-KO cells at baseline or treated with CCCP, respectively, underscoring that PGAM5 is predominantly cleaved by PARL (Fig. 3J). In summary, we observed baseline abnormalities in PARL abundance and PGAM5 cleavage which is exacerbated upon mitochondrial depolarization in TAZ-deficient HEK293 cells.

Targeting CL with bromoenol lactone and SS-31 normalizes downstream cellular dysfunction

To determine if targeting CL and CL metabolism would affect the dysregulation observed in respiratory CI and/or MQC, *TAZ*$^{\Delta 45}$ and WT cells were treated with either bromoenol lactone (BEL) or SS-31. Previous studies have shown that treatment with BEL, an inhibitor

of calcium-independent PLA_2 ($iPLA_2$), partially remediates CL abnormalities by reducing MLCL accumulation and CL depletion [37-38]. SS-31, a cell permeable mitochondria-targeted tetrapeptide, selectively binds CL where it has been shown to stabilize cristae morphology and preserve mitochondrial bioenergetics [39-40].

The relative abundance of NDUFAF1 in *TAZ*$^{\Delta 45}$ cells increased following BEL treatment and significantly increased following SS-31 treatment ($p= 2.8 \times 10^{-5}$) (Fig. 4A, Table S6). *NDUFAF1* relative mRNA expression significantly increased in *TAZ*$^{\Delta 45}$ cells following both BEL and SS-31 treatment ($p= 0.05$ and $p= 0.01$, respectively) (Fig. 4B, Table S7). The relative mRNA expression was also measured for the other 4 CI associated genes that had significantly reduced levels in *TAZ*$^{\Delta 45}$ cells at baseline (*NDUFB2*, *NDUFAB1*, *NDUFB4*, and *NDUFB6*). Following BEL treatment, these significant differences in expression between *TAZ*$^{\Delta 45}$ vs. WT were no longer observed in any of the 4 genes tested, and following SS-31 treatment, the significant differences were no longer observed in 3 of the 4 genes tested (Fig. S11, Table S7).

Next, CI holoenzyme abundance was measured in BEL and SS-31 treated cells by BN-PAGE. CI remained the most significantly reduced complex in *TAZ*$^{\Delta 45}$ cells after BEL or SS-31 treatment (Fig. 4D). However, both treatments had a subtle effect on the ratio of both CI to CIV (CI:CIV) and CI to CII (CI:CII) (Fig. 4D-E, Table S8). The CI:CIV relative abundance increased from 0.59 in untreated *TAZ*$^{\Delta 45}$ cells to 0.77 in *TAZ*$^{\Delta 45}$-BEL cells and 0.80 in *TAZ*$^{\Delta 45}$-SS-31 cells (Fig. 4E, Table S8). The CI:CII relative abundance significantly increased from 0.66 in untreated *TAZ*$^{\Delta 45}$ cells to 0.89 in *TAZ*$^{\Delta 45}$-BEL cells ($p= 6.1 \times 10^{-3}$) and to 0.83 in *TAZ*$^{\Delta 45}$-SS-31 cells (Fig. 4E, Table S8). Overall, treatment with either BEL or SS-31 showed a subtle increase in CI holoenzyme abundance.

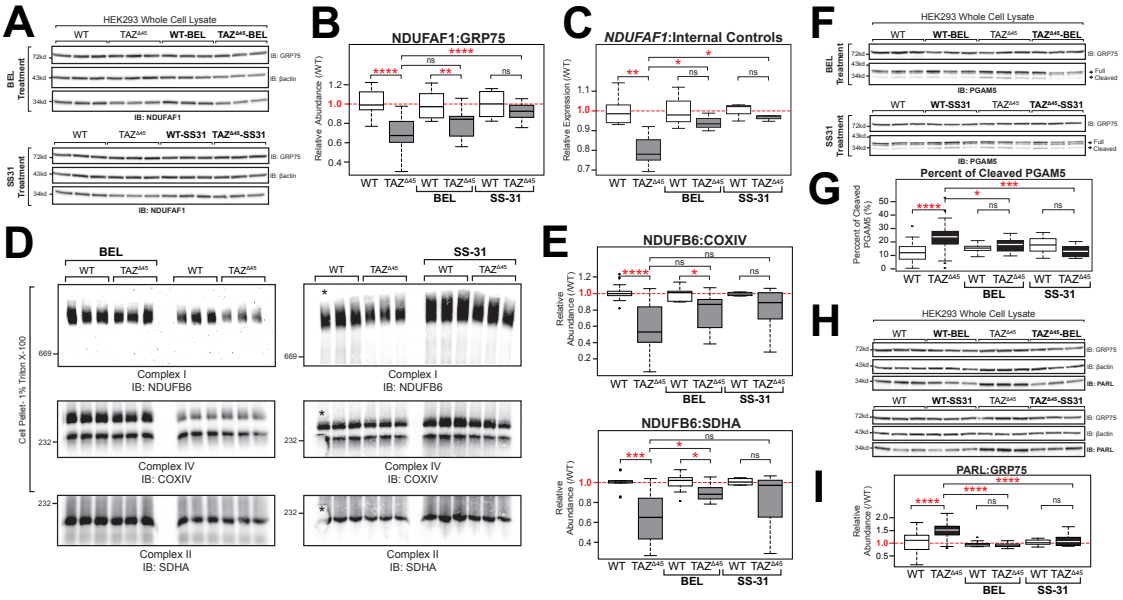

Figure 4. Targeting CL or CL metabolism with bromoenol lactone and SS-31 modifies mitochondrial dysfunction. (A) HEK293 WT and *TAZ*$^{\Delta 45}$ cells were treated for 48 hours with 2.5uM bromoenol lactone (BEL) and 7 days with 100nM SS-31. Whole cell lysate (40-45 ug) of the indicated lines were immunoblotted for the indicated proteins. **(B)** Band intensities, relative to the loading control GRP75, were quantified and plotted relative to WT abundance; WT n=27, *TAZ*$^{\Delta 45}$ n=26, WT-BEL n=9, *TAZ*$^{\Delta 45}$-BEL n=9, WT-SS-31 n=9, *TAZ*$^{\Delta 45}$-SS-31 n=9. **(C)** Relative mRNA expression of *NDUFAF1* determined by qRT-PCR and $\Delta\Delta C_T$ quantification using each respective control; WT n=6, *TAZ*$^{\Delta 45}$ n=6, WT-BEL n=3, *TAZ*$^{\Delta 45}$-BEL n=3, WT-SS-31 n=3, *TAZ*$^{\Delta 45}$-SS-31 n=3 per gene. **(D)** BN-PAGE of HEK293 WT and *TAZ*$^{\Delta 45}$ cells treated for 48 hrs with 2.5uM BEL (120 ug total protein) and 7 days with 100nM SS-31 solubilized in 1% Triton X-100 immunoblotted for the indicated proteins. All samples were resolved on a single gel and exposed for the same duration. The WT lane indicated with the asterisk was not used for quantification due to air bubbles. **(E)** Band intensities were quantified, and CI abundance was represented as the ratio of CI band intensity to CIV or CII. Abundance was plotted relative to respective control; CI:CIV(WT n=13, *TAZ*$^{\Delta 45}$ n=16, WT-BEL n=9, *TAZ*$^{\Delta 45}$-BEL n=11, WT-SS-31 n=4, *TAZ*$^{\Delta 45}$-SS-31 n=6), CI:CII (WT n=10, *TAZ*$^{\Delta 45}$ n=13, WT-BEL n=9, *TAZ*$^{\Delta 45}$-BEL n=10, WT-SS-31 n=4, *TAZ*$^{\Delta 45}$-SS-31 n=6). **(F)** Whole cell lysate (40-45 ug) of the indicated lines and treatment conditions were immunoblotted for the indicated proteins. **(G)** Band intensities, relative to the loading control GRP75, for both full-length and cleaved PGAM5 were individually quantified and plotted as the percent of cleaved PGAM5 (cleaved/full+cleaved); WT n=41, *TAZ*$^{\Delta 45}$ n=41, WT-BEL n=16, *TAZ*$^{\Delta 45}$-BEL n=16, WT-SS-31 n=9, *TAZ*$^{\Delta 45}$-SS-31 n=8. **(H)** Whole cell lysate (40-45 ug) of the indicated lines and treatment conditions were immunoblotted for the indicated proteins. **(I)** Band intensities, relative to the loading control GRP75, were quantified and plotted relative to WT abundance; WT n=54, *TAZ*$^{\Delta 45}$ n=48, WT-BEL n=11, *TAZ*$^{\Delta 45}$-BEL n=11, WT-SS-31 n=10, *TAZ*$^{\Delta 45}$-SS-31 n=12. Significant differences are indicated; * ≤ 0.05, ** ≤ 0.005, *** ≤ 0.0005, **** ≤ 0.00005.

Immunoblotting of BEL and SS-31 treated HEK293 whole cell lysate for PGAM5 showed a significant decrease in the percentage of cleaved PGAM5 in *TAZ*$^{\Delta 45}$-BEL (18%, p= 0.01) and *TAZ*$^{\Delta 45}$-SS-31 (13%, p= 2.6 x 10^{-4}) cells compared to TAZ$^{\Delta 45}$-untreated cells (23%) (Fig. 4F-G, Table S9). There was no significant difference in the percentage of cleaved PGAM5 in *TAZ*$^{\Delta 45}$-BEL versus WT-BEL cells or *TAZ*$^{\Delta 45}$-SS-31 versus WT-SS-31 cells (Fig. 4G, Table S9). Further, immunoblotting of BEL and SS-31 treated HEK293 whole cell lysate for PARL showed a significant decrease in the relative abundance of PARL in *TAZ*$^{\Delta 45}$-BEL (FC= 0.93, p= 7.1 x 10^{-15}) and *TAZ*$^{\Delta 45}$-SS-31 (FC= 1.11, p= 9.9 x 10^{-5}) cells compared to TAZ$^{\Delta 45}$-untreated cells (FC= 1.53) (Fig. 4H-I, Table S10), which was essentially restored to WT levels. Collectively, these results indicate that drugs that target CL partially rescue the defects in CI and MQC observed in TAZ-deficient cells.

3.5 Discussion

As a central phospholipid of the IMM, CL has been shown to have diverse roles in mitochondrial function [1]. Yet, these diverse roles are currently underappreciated in the pathophysiology of Barth syndrome, which is the only known Mendelian disorder of CL metabolism. In this study, we took an untargeted approach to identify dysregulated proteins in TAZ-deficient HEK293 cells and pursued two areas of dysregulation for further study: complex I (CI) of the respiratory chain and components of mitochondrial quality control (MQC).

Previous work has linked TAZ deficiency and mitochondrial respiratory chain dysfunction, with several studies pointing towards CI as the most impacted respiratory chain complex [15,17,41]. In this work we confirmed that CI abundance and function are abnormal in TAZ deficiency. We further showed that this dysfunction is potentially driven by the reduced abundance of 5 subunits of mitochondrial CI, *MT-ND3*, *NDUFA5*, *NDUFAB1*, *NDUFB2*, *NDUFB4,* and CI assembly factor, *NDUFAF1*. There are several possibilities for the mechanism by which these specific deficiencies could disrupt CI function, including disruption of the coordinated modular assembly of CI and further studies into CI modular assembly in BTHS could prove to be revealing [20,42]. Alternatively, abnormal CL itself may have a direct effect on disrupting CI assembly or function. Further studies may clarify the mechanism of reduced CI mRNA expression and ultimately function.

We further identified abnormal expression and regulation of MQC associated proteins including PARL and PGAM5. MQC, involving the processes of mitochondrial proteostasis, biogenesis, dynamics, and mitophagy, is emerging as a central theme for the pathogenesis of various diseases [43-45]. PARL participates in MQC via reciprocal proteolysis of PGAM5 and PINK1 [22,32]. Upon mitochondrial depolarization, PARL upregulation accelerates PGAM5 proteolysis which drives mitochondrial fragmentation [32]. Defective mitochondrial quality control, particularly as it affects cellular energy production and stress responsiveness, is increasingly recognized for its role in diverse forms of cardiac dysfunction and may be central to the cardiac pathogenesis of BTHS [46].

In order to determine if the abnormalities we identified are directly associated with abnormal CL, we tested the ability of a BEL, pharmacological inhibitor of PLA2γ, and SS-

31, a CL binding peptide, to ameliorate the two TAZ-deficient phenotypes we established. Indeed, we showed that targeting CL and CL metabolism with BEL and SS-31 is sufficient to modulate CI subunit gene expression and protein abundance, PARL abundance, and PGAM5 cleavage. Thus, targeting multiple aspects of CL metabolism may be a feasible therapeutic approach in BTHS.

It is notable that among the CI subunits that we identified as having altered expression in TAZ deficiency, NDUFAB1 has an essential role in fatty acid biosynthesis due to its dual role as the mitochondrial acyl carrier protein (mt-ACP) [47]. In fact, the GO term "protein lipoylation" was identified in the functional annotation of proteins with a FC ≤ 0.80 (Table S2A). In this role, abnormal expression of NDUFAB1/mt-ACP in TAZ deficiency may have further implications beyond affecting CI assembly and function, including affecting CL acyl chain content. Additionally, mt-ACP is involved in the assembly of the mitochondrial ribosome, and therefore mt-ACP expression and abundance may further influence changes in mitochondrial gene expression [48]. Further examining the essential role of NDUFAB1, outside of CI assembly and function, may provide a mechanistic link between altered CL metabolism and altered bioenergetic metabolism. Defects in MQC pathways, have been implicated in the pathogenesis of various cardiac pathologies relevant to BTHS. Additionally, enlarged mitochondria have been observed in BTHS patient and mouse model derived cardiac tissue, consistent with impaired mitophagy [49-52]. Thus, further examining these pathways in an appropriate cellular context could provide insight into potential therapeutic targets for BTHS and other conditions resulting from MQC dysfunction.

Finally, it is important to note that some of our results were cell-type specific. We identified a reduction in CI subunit protein abundance, holoenzyme abundance, and CI activity in both HEK293 TAZ-deficient cells and BTHS LCLs; however, in BTHS LCLs reduced mRNA expression of CI subunits was not observed. The differences in mRNA expression observed between the HEK293s and the LCLs could be due to epigenetic and transcriptomic differences observed in EBV transformed LCL lines, the genetic differences between the BTHS individuals, and/or cell type specific regulation of CI associated genes/proteins [53]. We also found that HEK293s and LCLs differed in PARL abundance, which is consistent with previous studies confirming cell-type specific expression and regulation of PARL, and introduces further questions about whether cell-type specific mechanisms of MQC contribute to the tissue distribution of disease in BTHS [54]. This hypothesis emphasizes the need for a clearer understanding of the cell-specific effects of abnormal CL content. To explore these questions, we are presently exploring respiratory chain and MQC dysfunction in diverse TAZ-deficient cell types in order to understand how these pathways are associated with the tissue specific expression of BTHS.

3.6 Conclusions

We identified and characterized two cellular pathways impacted by TAZ deficiency by employing a discovery-based approach in a new HEK293 TAZ-deficient cellular model: complex I (CI) of the mitochondrial respiratory chain and mitochondrial quality control (MQC). We, not only confirmed reduced CI protein and holoenzyme abundance, but expanded our current understanding of respiratory chain abnormalities by showing reduced

CI mRNA expression with evidence for distinct regulation in differing cell types. Additionally, we uncovered aberrant abundance of the MQC protein PARL, which was accompanied by altered cleavage of the downstream MQC mediator and PARL target, PGAM5. Finally, we found that modulating CL normalizes CI gene expression, protein, and holoenzyme abundance, as well as ameliorating PARL abundance and the aberrant ratio of cleaved to full length PGAM5. Thus, abnormal CL in TAZ deficiency has a direct role in dysregulating both CI of the mitochondrial respiratory chain and MQC.

3.7 Acknowledgements

We thank Ya-Wen Lu and Michelle Acoba of the Claypool Lab for their critical and fruitful technical guidance. We also want to thank Thomas Langer, and the Langer Laboratory for the generous gift of PARL antibody and PARL-KO HEK293 cells. Research reported in this publication was supported by the National Heart, Lung, And Blood Institute of the National Institutes of Health under Award Number F31HL147454 to A.F.A. The content is solely the responsibility of the authors and does not necessarily represent the official views of the National Institutes of Health. Proteomics analysis was supported by the Johns Hopkins University School of Medicine Core Coins Program to V.J.H.

3.8 Conflict of Interest

Hilary Vernon has received research support from Stealth BioTherapeutics.

3.9 References

1. A. F. Anzmann, S. M. Claypool, H. Vernon, “Mitochondrial Dysfunction and Barth Syndrome” in Handbook of Mitochondrial Dysfunction, S. I. Ahmad, Ed. (CRC Press/Taylor & Francis Group, 2019), pp. 61–77.
2. I. L. Gonzalez, Barth syndrome: TAZ gene mutations, mRNAs, and evolution. Am. J. Med. Genet. 134 A, 409–414 (2005).
3. Y. W. Lu, et al., Defining functional classes of Barth syndrome mutation in humans. Hum. Mol. Genet. 25, 1754–1770 (2016).
4. Y. Xu, A. Malhotra, M. Ren, M. Schlame, The enzymatic function of tafazzin. J. Biol. Chem. 281, 39217–39224 (2006).
5. P. Vreken, et al., Defective remodeling of cardiolipin and phosphatidylglycerol in Barth syndrome. Biochem. Biophys. Res. Commun. 279, 378–382 (2000).
6. W. Kulik, et al., Bloodspot Assay Using HPLC – Tandem Mass Spectrometry for Detection of Barth Syndrome. Clin. Chem. 54, 371–378 (2008).
7. P. G. Barth, et al., An X-linked mitochondrial disease affecting cardiac muscle, skeletal muscle and neutrophil leucocytes. J. Neurol. Sci. 62, 327–355 (1983).
8. C. Ferreira, R. Thompson, H. Vernon, “Barth Syndrome” in GeneReviews®[Internet], 1993rd–2018th Ed., M. P. Adam, H. H. Ardinger, R. A. Pagon, S. E. Wallace, Eds. (University of Washington, 2014) https:/doi.org/NBK247162 [bookaccession].
9. A. E. Roberts, et al., The Barth Syndrome Registry: Distinguishing disease characteristics and growth data from a longitudinal study. Am. J. Med. Genet. Part A 158 A, 2726–2732 (2012).
10. W. R. Thompson, et al., New targets for monitoring and therapy in Barth syndrome. Genet. Med. 18, 1001–1010 (2016).
11. E. J. Lesnefsky, Q. Chen, C. L. Hoppel, Mitochondrial Metabolism in Aging Heart. Circ. Res. 118, 1593–1611 (2016).
12. S. M. Claypool, C. M. Koehler, The complexity of cardiolipin in health and disease. Trends Biochem. Sci. 37, 32–41 (2012).
13. L. K. Cole, et al., Impaired cardiolipin biosynthesis prevents hepatic steatosis and diet-induced obesity. Diabetes 65, 3289–3300 (2016).
14. Z. Younossi, et al., Global burden of NAFLD and NASH: Trends, predictions, risk factors and prevention. Nat. Rev. Gastroenterol. Hepatol. 15, 11–20 (2018).
15. K. Pfeiffer, et al., Cardiolipin Stabilizes Respiratory Chain Supercomplexes. J. Biol. Chem. 278, 52873–52880 (2003).
16. M. Zhang, E. Mileykovskaya, W. Dowhan, Gluing the respiratory chain together: Cardiolipin is required for supercomplex formation in the inner mitochondrial membrane. J. Biol. Chem. 277, 43553–43556 (2002).
17. M. McKenzie, M. Lazarou, D. R. Thorburn, M. T. Ryan, Mitochondrial Respiratory Chain Supercomplexes Are Destabilized in Barth Syndrome Patients. J. Mol. Biol. 361, 462–469 (2006).
18. D. W. Huang, B. T. Sherman, R. A. Lempicki, Systematic and integrative analysis of large gene lists using DAVID bioinformatics resources. Nat. Protoc. 4, 44–57 (2009).
19. D. W. Huang, B. T. Sherman, R. A. Lempicki, Bioinformatics enrichment tools: Paths toward the comprehensive functional analysis of large gene lists. Nucleic Acids Res. 37, 1–13 (2009).
20. S. Guerrero-Castillo, et al., The Assembly Pathway of Mitochondrial Respiratory Chain Complex I. Cell Metab. 25, 128–139 (2017).
21. L. Stiburek, et al., Knockdown of Human Oxa1l Impairs the Biogenesis of F1Fo-ATP Synthase and NADH:Ubiquinone Oxidoreductase. J. Mol. Biol. 374, 506–516 (2007).
22. M. Spinazzi, B. De Strooper, PARL: The mitochondrial rhomboid protease. Semin. Cell Dev. Biol. 60, 19–28 (2016).
23. G. Shi, G. A. McQuibban, The Mitochondrial Rhomboid Protease PARL Is Regulated by PDK2 to Integrate Mitochondrial Quality Control and Metabolism. Cell Rep. 18, 1458–1472 (2017).
24. S. Saita, et al., PARL mediates Smac proteolytic maturation in mitochondria to promote apoptosis. Nat. Cell Biol. 19, 318–328 (2017).

25. C. Yang, et al., Mitochondrial phosphatase PGAM5 regulates Keap1-mediated Bcl-xL degradation and controls cardiomyocyte apoptosis driven by myocardial ischemia/reperfusion injury. Vitr. Cell. Dev. Biol. - Anim. 53, 248–257 (2017).
26. B. Wang, et al., AMPKa2 protects against the development of heart failure by enhancing mitophagy via PINK1 phosphorylation. Circ. Res. 122, 712–729 (2018).
27. S. Shires, Å. B. Gustafsson, Regulating Renewable Energy: Connecting AMPKα2 to PINK1/ Parkin-Mediated Mitophagy in the Heart. Circ. Res. 122, 649–651 (2018).
28. C. Potting, et al., TRIAP1/PRELI complexes prevent apoptosis by mediating intramitochondrial transport of phosphatidic acid. Cell Metab. 18, 287–295 (2013).
29. X. Miliara, et al., Structural determinants of lipid specificity within Ups/PRELI lipid transfer proteins. Nat. Commun. 10, 1130 (2019).
30. L. Galluzzi, A. López-Soto, S. Kumar, G. Kroemer, Caspases Connect Cell-Death Signaling to Organismal Homeostasis. Immunity 44, 221–231 (2016).
31. R. O. Vogel, et al., Human mitochondrial complex I assembly is mediated by NDUFAF1. FEBS J. 272, 5317–5326 (2005).
32. S. Sekine, et al., Rhomboid protease PARL mediates the mitochondrial membrane potential loss-induced cleavage of PGAM5. J. Biol. Chem. 287, 34635–34645 (2012).
33. K. Ma, et al., Dynamic PGAM5 multimers dephosphorylate BCL-xL or FUNDC1 to regulate mitochondrial and cellular fate. Cell Death Differ. 27, 1036–1051 (2020).
34. J. Wang, P. Zhu, R. Li, J. Ren, H. Zhou, Fundc1-dependent mitophagy is obligatory to ischemic preconditioning-conferred renoprotection in ischemic AKI via suppression of Drp1-mediated mitochondrial fission. Redox Biol. 30, 101415 (2020).
35. W. Lu, et al., Mitochondrial protein PGAM5 regulates mitophagic protection against cell necroptosis. PLoS One 11, e0147792 (2016).
36. A. Yamaguchi, et al., Cleaved PGAM5 is released from mitochondria depending on proteasome-mediated rupture of the outer mitochondrial membrane during mitophagy. J. Biochem. 165, 19–25 (2019).
37. Y. W. Lu, S. M. Claypool, Disorders of phospholipid metabolism: An emerging class of mitochondrial disease due to defects in nuclear genes. Front. Genet. 6 (2015).
38. A. Malhotra, et al., Role of calcium-independent phospholipase A2 in the pathogenesis of Barth syndrome. Proc. Natl. Acad. Sci. 106, 2337–2341 (2009).
39. H. H. Szeto, First-in-class cardiolipin-protective compound as a therapeutic agent to restore mitochondrial bioenergetics. Br. J. Pharmacol. 171, 2029–50 (2014).
40. A. V. Birk, W. M. Chao, C. Bracken, J. D. Warren, H. H. Szeto, Targeting mitochondrial cardiolipin and the cytochrome c/cardiolipin complex to promote electron transport and optimize mitochondrial ATP synthesis. Br. J. Pharmacol. 171, 2017–2028 (2014).
41. M. Zhang, E. Mileykovskaya, W. Dowhan, Cardiolipin is essential for organization of complexes III and IV into a supercomplex in intact yeast mitochondria. J. Biol. Chem. 280, 29403–29408 (2005).
42. L. E. Formosa, M. G. Dibley, D. A. Stroud, M. T. Ryan, Building a complex complex: Assembly of mitochondrial respiratory chain complex I. Semin. Cell Dev. Biol. 76, 154–162 (2018).
43. A. Picca, et al., Mitochondrial quality control mechanisms as molecular targets in cardiac ageing. Nat. Rev. Cardiol. 15, 543–554 (2018).
44. F. Fischer, A. Hamann, H. D. Osiewacz, Mitochondrial quality control: An integrated network of pathways. Trends Biochem. Sci. 37, 284–292 (2012).
45. H. B. Suliman, C. A. Piantadosi, Mitochondrial quality control as a therapeutic target. Pharmacol. Rev. 68, 20–48 (2016).
46. G. W. Dorn, Mitochondrial dynamism and heart disease: changing shape and shaping change. EMBO Mol. Med. 7, 865–77 (2015).
47. D. A. Stroud, et al., Accessory subunits are integral for assembly and function of human mitochondrial complex i. Nature 538, 123–126 (2016).
48. A. Brown, et al., Structures of the human mitochondrial ribosome in native states of assembly. Nat. Struct. Mol. Biol. 24, 866–869 (2017).
49. S. L. N. Clarke, et al., Barth Syndrome. Orphanet J. Rare Dis. 8 (2013).
50. S. Lavandero, M. Chiong, B. A. Rothermel, J. A. Hill, Autophagy in cardiovascular biology. J. Clin. Invest. 125, 55–64 (2015).

51. E. Lee, et al., Autophagy is essential for cardiac morphogenesis during vertebrate development. Autophagy 10, 572–87 (2014).
52. A. Saric, K. Andreau, A. S. Armand, I. M. Møller, P. X. Petit, Barth syndrome: From mitochondrial dysfunctions associated with aberrant production of reactive oxygen species to pluripotent stem cell studies. Front. Genet. 6, 359 (2016).
53. L. Ozgyin, A. Horvath, Z. Hevessy, B. L. Balint, Extensive epigenetic and transcriptomic variability between genetically identical human B-lymphoblastoid cells with implications in pharmacogenomics research. Sci. Rep. 9, 4889 (2019).
54. D. V. Jeyaraju, H. M. McBride, R. B. Hill, L. Pellegrini, Structural and mechanistic basis of Parl activity and regulation. Cell Death Differ. 18, 1531–1539 (2011).
55. F. A. Ran, et al., Genome engineering using the CRISPR-Cas9 system. Nat. Protoc. (2013) https:/doi.org/10.1038/nprot.2013.143.
56. P. D. Hsu, et al., DNA targeting specificity of RNA-guided Cas9 nucleases. Nat. Biotechnol. 31, 827–832 (2013).
57. F. M. Vaz, et al., Mutations in PCYT2 disrupt etherlipid biosynthesis and cause a complex hereditary spastic paraplegia. Brain 142, 3382–3397 (2019).
58. S. M. Claypool, Y. Oktay, P. Boontheung, J. A. Loo, C. M. Koehler, Cardiolipin defines the interactome of the major ADP/ATP carrier protein of the mitochondrial inner membrane. J. Cell Biol. 182, 937–950 (2008).
59. A. Elgogary, et al., Combination therapy with BPTES nanoparticles and metformin targets the metabolic heterogeneity of pancreatic cancer. Proc. Natl. Acad. Sci. U. S. A. 113, E5328–E5336 (2016).
60. T. Nguyen, et al., Uncovering the Role of N-Acetyl-Aspartyl-Glutamate as a Glutamate Reservoir in Cancer. Cell Rep. 27, 491–501 (2019).
61. R Core Team, R: A language and environment for statistical computing.No Title (2016).

3.10 Supplementary Information

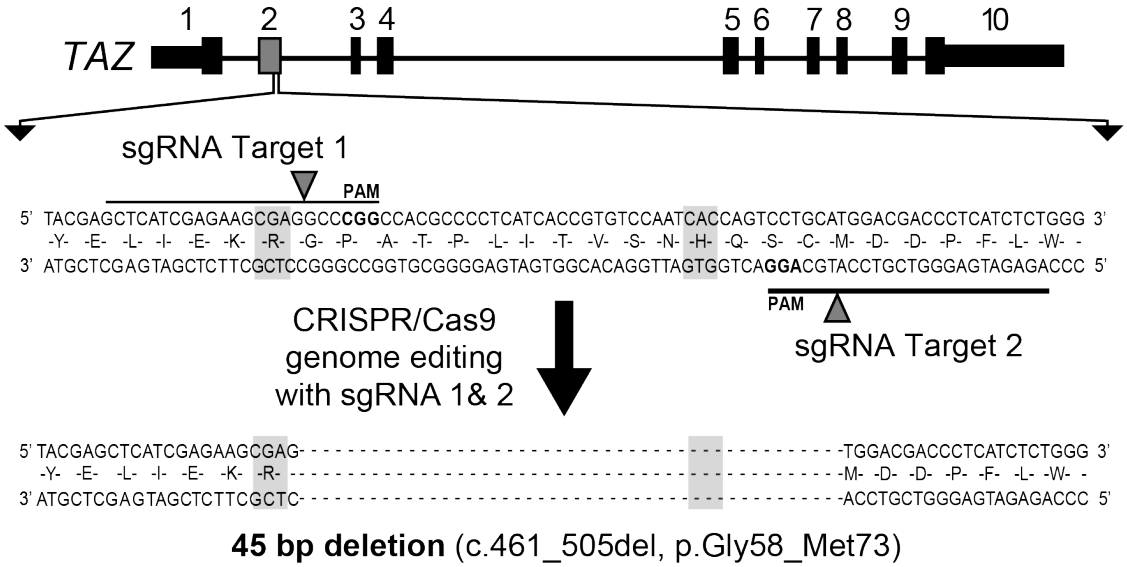

Figure S1. CRISPR/Cas9 genome editing with two single guide RNAs (sgRNAs) targeting exon 2 of *TAZ* results in a 45 bp deletion. The 45 bp deletion, noted by dashes, encompasses a predicted acyltransferase domain and covers an area of *TAZ* where multiple pathological variants have been described, such as p.R57L (c.170G>T) and p.H69Q (c.207C>G), highlighted in grey.

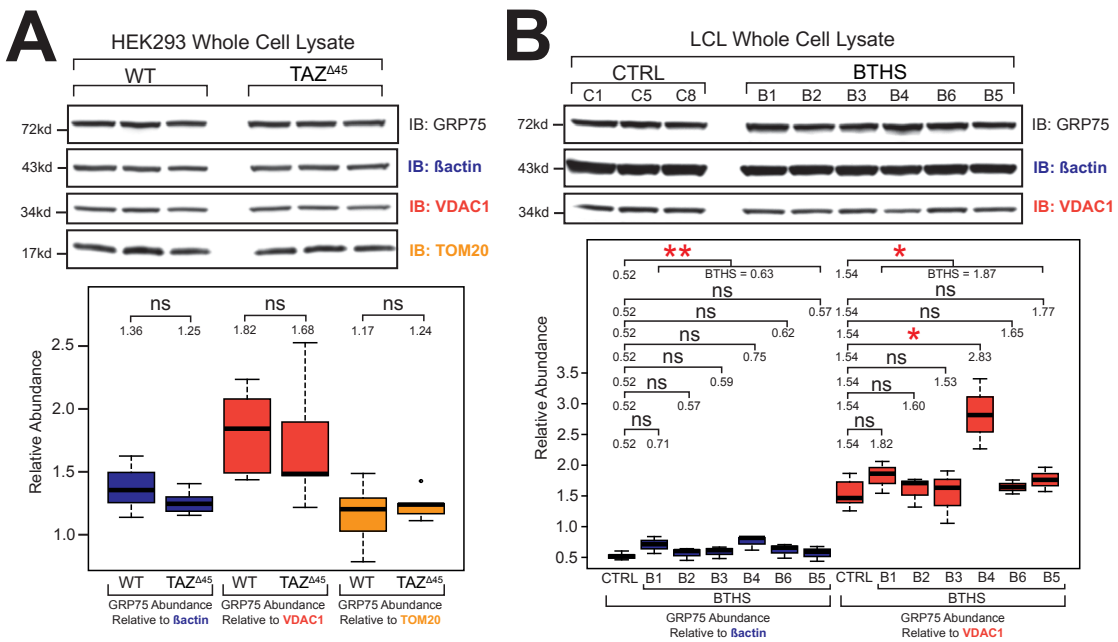

Figure S2. Comparable abundance of cytosolic and mitochondrial proteins in the absence of TAZ. Whole cell lysate (40 ug) of the indicated lines **(A)** HEK293 and **(B)** LCL lines were immunoblotted for the indicated proteins. Band intensities were quantified and plotted relative to ß-actin (blue), VDAC1 (red), and TOM20 (yellow); WT n=9, *TAZ*$^{\Delta 45}$ n=9, CTRL n=9 (C1 n=3, C5 n=3, C8 n=3), BTHS n=18 (B1 n=3, B2 n=3, B3 n=3, B4 n=3, B6 n=3, B5 n=3). Significant differences are indicated; * ≤ 0.05, ** ≤ 0.005, *** ≤ 0.0005, **** ≤ 0.00005.

Table S1. CRISPR/Cas9 sgRNA guide sequences and predicted off-target sites.

sgRNA	Guide Sequence (5' to 3')	Off-Targets (5' to 3')	Score[1]	MMs[2]	Hg38 Location	Sequenced?
Target 1	GCTCATCGAGAAGCGAGGCC**CGG**[3]	GCCCGTCAAGAAGCGAGGCCCAG	2.4	3	chr9:-136416984	Y
		GCTCATTGTTAAGCGAGGCCTAG	0.9	3	chr5:-164071618	Y
		CTTCAGCCAGAAGCGAGGCCAAG	0.8	4	chr13:+111688858	Y
		CCCCATCGAGAAGCGCGGCCAAG	0.6	3	chr4:-132956077	N
		GCCCATCGGGAAGCCAGGCCGAG	0.5	3	chr18:-8629183	N
Target 2	GAGATGAGGGTCGTCCATGC**AGG**[3]	GAGATGTAGCTCGTCCATGCTGG	1.5	3	chr3:+173436340	Y
		GTTCAGAGGGTCGTCCATGCAAG	1.3	3	chr7:-70923313	Y
		GATATGAGGGGAGTCCATGCAGG	0.7	3	chrX:-12667869	N
		GACAAGAGGTTGGTCCATGCCAG	0.6	4	chr7:+65692780	N
		CTGGTGAGGGTCTTCCATGCCAG	0.6	4	chr8:-125971306	N

[1] Off-target score calculated at cripsr.mit.edu based on scoring algorithm from Hsu et al. 2013 (2)
[2] The number of mismatches between the guide sequence and the "off-target" sequence
[3] PAM site is bolded

Table S2A. Significant KEGG & GO terms determined by functional annotation analysis of the proteins with a FC ≤ 0.80 (n=215).

	# OF GENES[1]	%[2]	P-VALUE[3]	FOLD ENRICHMENT
KEGG PATHWAYS				
Parkinson's disease	13	6.1	6.80E-08	7.8
Oxidative phosphorylation*	11	5.1	2.70E-06	7
Huntington's disease	11	5.1	6.80E-05	4.9
Alzheimer's disease	10	4.7	1.30E-04	5.1
Non-alcoholic fatty liver disease (NAFLD)	9	4.2	3.40E-04	5.1
Cardiac muscle contraction	6	2.8	1.70E-03	6.8
Bile secretion	5	2.3	8.30E-03	6.2
Dilated cardiomyopathy	5	2.3	1.60E-02	5.1
Metabolic pathways*	23	10.7	1.90E-02	1.6
Ribosome	6	2.8	2.10E-02	3.7
GO TERMS: BIOLOGICAL PROCESSES				
platelet degranulation	10	4.7	2.60E-06	8.5
mitochondrial respiratory chain complex I assembly*#	7	3.3	7.90E-05	9.7
mitochondrial electron transport, NADH to ubiquinone*#	6	2.8	2.30E-04	10.7
actin filament organization	6	2.8	1.40E-03	7.3
response to oxidative stress	7	3.3	1.60E-03	5.6
protein lipoylation	3	1.4	2.60E-03	37.5
negative regulation of endothelial cell proliferation	4	1.9	4.30E-03	12.1
negative regulation of ATPase activity*	3	1.4	5.50E-03	26.2
aerobic respiration*	4	1.9	6.10E-03	10.6
protein targeting to mitochondrion*	4	1.9	6.70E-03	10.3
muscle contraction	6	2.8	7.50E-03	4.9
muscle filament sliding	4	1.9	9.10E-03	9.2
retina homeostasis	4	1.9	1.10E-02	8.7
rRNA processing	8	3.7	1.10E-02	3.3
wound healing	5	2.3	1.30E-02	5.5
Ossification	5	2.3	1.30E-02	5.5
cellular response to interferon-beta	3	1.4	1.40E-02	16.4
ribosomal small subunit biogenesis	3	1.4	1.40E-02	16.4
mitochondrial electron transport, cytochrome c to oxygen*	3	1.4	2.10E-02	13.1
SRP-dependent cotranslational protein targeting to membrane	5	2.3	2.20E-02	4.7
Translation	8	3.7	2.60E-02	2.8

cellular response to vascular endothelial growth factor stimulus	3	1.4	2.80E-02	11.4
response to calcium ion	4	1.9	2.80E-02	6
response to electrical stimulus	3	1.4	3.00E-02	10.9
positive regulation of osteoblast differentiation	4	1.9	3.10E-02	5.8
cytoplasmic translation	3	1.4	3.30E-02	10.5
ribosomal large subunit biogenesis	3	1.4	3.30E-02	10.5
viral transcription	5	2.3	3.90E-02	3.9
positive regulation of phagocytosis	3	1.4	4.30E-02	9
sarcomere organization	3	1.4	4.30E-02	9
one-carbon metabolic process*	3	1.4	4.50E-02	8.7
nuclear-transcribed mRNA catabolic process, nonsense-mediated decay	5	2.3	4.70E-02	3.7
vascular endothelial growth factor receptor signaling pathway	4	1.9	4.90E-02	4.9
GO TERMS: CELLULAR COMPARTMENTS				
mitochondrion*	42	19.6	2.30E-09	2.8
mitochondrial inner membrane*	20	9.3	5.80E-07	4
extracellular exosome	55	25.7	3.10E-05	1.7
prefoldin complex	4	1.9	4.70E-05	50.8
mitochondrial respiratory chain complex I*[#]	6	2.8	2.10E-04	10.9
platelet alpha granule lumen	6	2.8	3.70E-04	9.7
Cytosol	57	26.6	6.90E-04	1.5
Cytoskeleton	13	6.1	1.00E-03	3.1
cell surface	16	7.5	1.20E-03	2.6
focal adhesion	13	6.1	1.60E-03	3
mitochondrial proton-transporting ATP synthase complex*	4	1.9	1.60E-03	16.9
mitochondrial membrane*	6	2.8	4.10E-03	5.7
actin filament	5	2.3	6.10E-03	6.8
cytosolic large ribosomal subunit	5	2.3	7.10E-03	6.5
basement membrane	5	2.3	1.20E-02	5.6
Costamere	3	1.4	1.90E-02	14
integral component of mitochondrial inner membrane*	3	1.4	2.10E-02	13.3
respiratory chain*	3	1.4	2.10E-02	13.3
stress fiber	4	1.9	2.30E-02	6.6
Microvillus	4	1.9	2.60E-02	6.2
M band	3	1.4	2.70E-02	11.6
blood microparticle	6	2.8	2.80E-02	3.5
myelin sheath	6	2.8	2.80E-02	3.5
Cytoplasm	72	33.6	3.20E-02	1.2
Microspike	2	0.9	3.30E-02	59.3

granular component	2	0.9	4.40E-02	44.4
muscle thin filament tropomyosin	2	0.9	4.40E-02	44.4
apical plasma membrane	8	3.7	4.60E-02	2.4
filamentous actin	3	1.4	4.70E-02	8.6
extracellular matrix	8	3.7	4.90E-02	2.4
GO TERMS: MOLECULAR FUNCTIONS				
structural constituent of muscle	6	2.8	1.10E-04	12.6
protein binding	125	58.4	2.00E-04	1.3
actin filament binding	8	3.7	7.60E-04	5.3
unfolded protein binding	7	3.3	1.60E-03	5.6
NADH dehydrogenase (ubiquinone) activity *#	5	2.3	2.10E-03	9.2
poly(A) RNA binding	25	11.7	2.10E-03	1.9
structural constituent of ribosome	9	4.2	3.80E-03	3.6
endopeptidase inhibitor activity	4	1.9	1.00E-02	8.8
identical protein binding	17	7.9	1.10E-02	2
structural molecule activity conferring elasticity	2	0.9	2.30E-02	87.9
structural constituent of cytoskeleton	5	2.3	3.60E-02	4
ubiquitin conjugating enzyme activity	3	1.4	4.20E-02	9.1
cytochrome-c oxidase activity *	3	1.4	4.50E-02	8.8

* References mitochondrion and/or metabolic pathways (n=18)
# References complex I of the oxidative phosphorylation pathways (n=4)

[1] The number of input proteins involved in the term
[2] The number of input proteins involved in the term divided by the total proteins/genes represented by the term
[3] Modified Fisher Exact p-value, EASE Score

Table S2B. Significant KEGG & GO terms determined by functional annotation analysis of the proteins with a FC ≥ 1.20 (n=621).

	# OF GENES[1]	%[2]	P-VALUE[3]	FOLD ENRICHMENT
KEGG PATHWAYS				
Chronic myeloid leukemia	9	1.4	2.50E-03	3.8
Metabolic pathways*	58	9.3	3.10E-03	1.4
Pancreatic cancer	8	1.3	5.40E-03	3.7
AMPK signaling pathway	11	1.8	7.50E-03	2.7
Alzheimer's disease	13	2.1	9.70E-03	2.3
Butanoate metabolism*	5	0.8	1.10E-02	5.6
Carbohydrate digestion and absorption	6	1	1.20E-02	4.3
Endocytosis	16	2.6	1.40E-02	2
Insulin signaling pathway	11	1.8	1.60E-02	2.4
Colorectal cancer	7	1.1	1.60E-02	3.4
Fatty acid metabolism*	6	1	2.10E-02	3.8
Notch signaling pathway	6	1	2.10E-02	3.8
Amino sugar and nucleotide sugar metabolism*	6	1	2.10E-02	3.8
p53 signaling pathway	7	1.1	2.30E-02	3.1
Biosynthesis of antibiotics	14	2.3	2.30E-02	2
Phagosome	11	1.8	2.70E-02	2.2
Adipocytokine signaling pathway	7	1.1	2.80E-02	3
Inositol phosphate metabolism*	7	1.1	3.00E-02	3
Proteoglycans in cancer	13	2.1	3.30E-02	2
Biosynthesis of unsaturated fatty acids	4	0.6	3.90E-02	5.2
Viral myocarditis	6	1	4.00E-02	3.2
Synthesis and degradation of ketone bodies	3	0.5	4.10E-02	9
Phosphatidylinositol signaling system	8	1.3	4.30E-02	2.5
Glucagon signaling pathway	8	1.3	4.60E-02	2.4
Cell adhesion molecules (CAMs)	10	1.6	4.60E-02	2.1
Fatty acid elongation	4	0.6	4.80E-02	4.8
Epstein-Barr virus infection	9	1.4	4.90E-02	2.2
GO TERMS: BIOLOGICAL PROCESSES				
covalent chromatin modification	14	2.3	7.30E-05	3.8
viral genome replication	5	0.8	8.40E-04	11
protein targeting to plasma membrane	6	1	1.30E-03	7.1
antigen processing and presentation of endogenous peptide antigen via MHC class I via ER pathway, TAP-independent	3	0.5	3.10E-03	30.9
positive regulation of apoptotic process*	20	3.2	4.20E-03	2.1

carbohydrate phosphorylation	5	0.8	5.90E-03	6.7
cell cycle arrest	12	1.9	6.10E-03	2.6
response to oxidative stress*	10	1.6	9.30E-03	2.8
cell migration	13	2.1	1.00E-02	2.3
phosphatidylinositol biosynthetic process	7	1.1	1.10E-02	3.7
long-chain fatty-acyl-CoA biosynthetic process	6	1	1.10E-02	4.4
macroautophagy*	8	1.3	1.10E-02	3.2
unsaturated fatty acid biosynthetic process	4	0.6	1.10E-02	8.2
muscle cell differentiation	4	0.6	1.10E-02	8.2
IRE1-mediated unfolded protein response	7	1.1	1.20E-02	3.7
positive regulation of DNA binding	5	0.8	1.20E-02	5.5
tRNA pseudouridine synthesis	3	0.5	1.40E-02	15.4
magnesium ion homeostasis	3	0.5	1.40E-02	15.4
antigen processing and presentation of peptide antigen via MHC class I	5	0.8	1.50E-02	5.1
neuron projection development	9	1.4	1.60E-02	2.8
positive regulation of substrate adhesion-dependent cell spreading	5	0.8	1.90E-02	4.8
membrane protein intracellular domain proteolysis	4	0.6	1.90E-02	6.9
cilium assembly	10	1.6	1.90E-02	2.5
regulation of apoptotic process*	14	2.3	2.10E-02	2
inner ear receptor stereocilium organization	4	0.6	2.20E-02	6.5
regulation of autophagy*	6	1	2.20E-02	3.7
amyloid precursor protein catabolic process	3	0.5	2.60E-02	11.6
response to cholesterol	3	0.5	2.60E-02	11.6
interferon-gamma-mediated signaling pathway	7	1.1	2.70E-02	3
protein maturation by protein folding	3	0.5	3.20E-02	10.3
pyrimidine nucleotide metabolic process*	3	0.5	3.20E-02	10.3
DNA topological change	3	0.5	3.20E-02	10.3
antigen processing and presentation of exogenous peptide antigen via MHC class I, TAP-independent	3	0.5	3.20E-02	10.3
cilium morphogenesis	10	1.6	3.30E-02	2.3
cell growth	6	1	3.40E-02	3.3
viral process	17	2.7	3.40E-02	1.8
purine nucleotide metabolic process*	3	0.5	4.00E-02	9.3
regulation of synaptic vesicle exocytosis	3	0.5	4.00E-02	9.3
cell volume homeostasis	3	0.5	4.00E-02	9.3
nucleocytoplasmic transport	4	0.6	4.60E-02	4.9
positive regulation of stress fiber assembly*	5	0.8	4.60E-02	3.7
UDP-N-acetylglucosamine biosynthetic process	3	0.5	4.70E-02	8.4
positive regulation of histone deacetylation	3	0.5	4.70E-02	8.4

chromatin organization	5	0.8	4.90E-02	3.6
histone H3 acetylation	5	0.8	4.90E-02	3.6
glycosaminoglycan catabolic process	4	0.6	5.00E-02	4.7
GO TERMS: CELLULAR COMPARTMENTS				
extracellular exosome	135	21.7	1.70E-06	1.5
membrane	110	17.7	3.70E-06	1.5
endoplasmic reticulum	51	8.2	1.90E-05	1.9
mitochondrion*	68	11	2.20E-04	1.6
cytosol	142	22.9	2.80E-04	1.3
cytoplasm	206	33.2	7.60E-04	1.2
nucleoplasm	120	19.3	8.10E-04	1.3
integral component of endoplasmic reticulum membrane	11	1.8	2.00E-03	3.3
integral component of luminal side of endoplasmic reticulum membrane	6	1	2.20E-03	6.4
phagocytic vesicle membrane	8	1.3	2.90E-03	4.2
endoplasmic reticulum membrane	44	7.1	3.60E-03	1.6
intermediate filament	11	1.8	3.80E-03	3
ruffle membrane	9	1.4	5.10E-03	3.4
mitochondrial inner membrane*	26	4.2	5.20E-03	1.8
ER to Golgi transport vesicle membrane	7	1.1	6.60E-03	4.1
mitochondrial intermembrane space*	8	1.3	1.00E-02	3.3
myelin sheath	12	1.9	1.10E-02	2.4
nucleus	202	32.5	1.30E-02	1.1
melanosome	9	1.4	1.70E-02	2.7
early endosome	15	2.4	1.80E-02	2
Golgi membrane	30	4.8	1.80E-02	1.6
centrosome	23	3.7	2.20E-02	1.7
costamere	4	0.6	2.20E-02	6.5
endoplasmic reticulum-Golgi intermediate compartment	7	1.1	2.30E-02	3.2
endoplasmic reticulum lumen	13	2.1	2.30E-02	2.1
cilium	11	1.8	2.60E-02	2.2
autolysosome	3	0.5	2.60E-02	11.5
ER-mitochondrion membrane contact site*	3	0.5	2.60E-02	11.5
integral component of mitochondrial outer membrane*	4	0.6	2.90E-02	5.9
stress fiber*	6	1	3.00E-02	3.4
F-actin capping protein complex	3	0.5	3.30E-02	10.2
nuclear heterochromatin	4	0.6	3.30E-02	5.6
lysosomal membrane	16	2.6	3.50E-02	1.8
early endosome membrane	9	1.4	3.50E-02	2.4

Golgi apparatus	39	6.3	3.60E-02	1.4
oligosaccharyltransferase complex	3	0.5	4.00E-02	9.2
dendrite	18	2.9	4.70E-02	1.7
MHC class I protein complex	3	0.5	4.80E-02	8.4
GO TERMS: MOLECULAR FUNCTIONS				
protein binding	335	53.9	2.90E-05	1.2
poly(A) RNA binding	55	8.9	3.10E-03	1.5
AP-3 adaptor complex binding	3	0.5	3.10E-03	30.5
TAP binding	3	0.5	3.10E-03	30.5
nucleosomal DNA binding	7	1.1	3.70E-03	4.6
cysteine-type endopeptidase activity involved in apoptotic process*	4	0.6	7.80E-03	9.4
chromatin binding	23	3.7	9.80E-03	1.8
1-phosphatidylinositol-3-phosphate 4-kinase activity	3	0.5	1.00E-02	18.3
GTPase activity	16	2.6	1.00E-02	2.1
peptide antigen binding	5	0.8	1.20E-02	5.5
GTP binding	22	3.5	1.50E-02	1.7
histone binding	10	1.6	1.90E-02	2.5
scaffold protein binding	6	1	2.00E-02	3.8
1-phosphatidylinositol-4-phosphate 5-kinase activity	3	0.5	2.00E-02	13.1
chromatin DNA binding	6	1	4.10E-02	3.2
cysteine-type endopeptidase activity	6	1	4.90E-02	3
* References mitochondrion and/or mitochondrial dynamics (n=20)				

[1] The number of input proteins involved in the term
[2] The number of input proteins involved in the term divided by the total proteins/genes represented by the term
[3] Modified Fisher Exact p-value, EASE Score

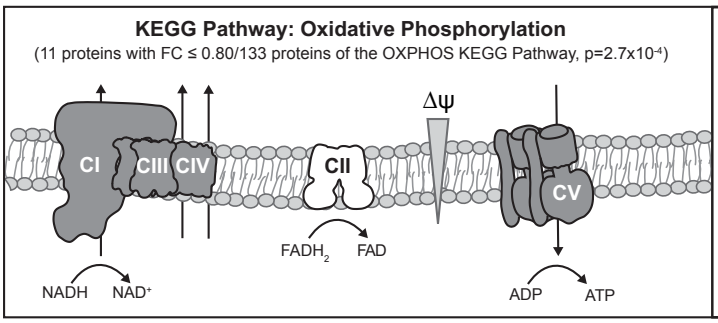

Oxidative Phosphorylation Complexes		
I	MT-ND3 NDUFA5 NDUFAB1	NDUFB2 NDUFB4
III	UQCRB	
IV	COX1 COX6C COX7C	
V	ATP8 ATP5G3	

Figure S3. The oxidative phosphorylation (OXPHOS) KEGG pathway is the most significant KEGG pathway enriched for proteins with a FC ≤ 0.80 that references mitochondria and or OXPHOS. Of the 133 genes in the OXPHOS KEGG pathway 11 encode proteins with a FC ≤ 0.80 in *TAZ*$^{\Delta 45}$ cells; half (n=5) are subunits of complex I (CI) and the remaining (n=6) are subunits of complex III, IV, and V.

Table S3. Proteomics quantification of all complex I (CI) associated proteins.

UniProt Entry	Gene Name	Module	Protein	#PSMs*	Unique Peptides	FC	P-Value
Complex I Subunits							
Q9UI09	*NDUFA12*	N	NADH dehydrogenase [ubiquinone] 1 alpha subcomplex subunit 12	46	8	0.973	0.93
P28331	*NDUFS1*	N	NADH-ubiquinone oxidoreductase 75 kDa subunit, mitochondrial	173	39	0.864	0.28
O75380	*NDUFS6*	N	NADH dehydrogenase [ubiquinone] iron-sulfur protein 6, mitochondrial	23	9	0.955	0.49
P49821	*NDUFV1*	N	NADH dehydrogenase [ubiquinone] flavoprotein 1, mitochondrial	105	21	0.872	0.21
P19404	*NDUFV2*	N	NADH dehydrogenase [ubiquinone] flavoprotein 2, mitochondrial	73	15	0.872	0.18
P56181	*NDUFV3*	N	NADH dehydrogenase [ubiquinone] flavoprotein 3, mitochondrial	5	3	1.037	0.69
O43678	*NDUFA2*	N/Q	NADH dehydrogenase [ubiquinone] 1 alpha subcomplex subunit 2	19	4	0.862	0.15
O43181	*NDUFS4*	N/Q	NADH dehydrogenase [ubiquinone] iron-sulfur protein 4, mitochondrial	21	7	0.890	0.22
Q16718	***NDUFA5***	**Q**	**NADH dehydrogenase [ubiquinone] 1 alpha subcomplex subunit 5**	**33**	**7**	**0.722**	**0.24**
P56556	*NDUFA6*	Q	NADH dehydrogenase [ubiquinone] 1 alpha subcomplex subunit 6	27	7	0.902	0.89
O95182	*NDUFA7*	Q	NADH dehydrogenase [ubiquinone] 1 alpha subcomplex subunit 7	33	9	0.834	0.21
Q16795	*NDUFA9*	Q	NADH dehydrogenase [ubiquinone] 1 alpha subcomplex subunit 9, mitochondrial	54	18	0.970	0.99
O75306	*NDUFS2*	Q	NADH dehydrogenase [ubiquinone] iron-sulfur protein 2, mitochondrial	130	22	1.018	0.95
O75489	*NDUFS3*	Q	NADH dehydrogenase [ubiquinone] iron-sulfur protein 3, mitochondrial	142	18	0.953	0.53
O75251	*NDUFS7*	Q	NADH dehydrogenase [ubiquinone] iron-sulfur protein 7, mitochondrial	27	6	0.873	0.94
O00217	*NDUFS8*	Q	NADH dehydrogenase [ubiquinone] iron-sulfur protein 8, mitochondrial	66	9	0.959	0.46
P03886	*MTND1*	P_P	NADH-ubiquinone oxidoreductase chain 1	4	2	1.236	0.43
P03891	*MTND2*	P_P	NADH-ubiquinone oxidoreductase chain 2	3	2	1.358	0.24
P03897	***MTND3****	**P_P**	**NADH-ubiquinone oxidoreductase chain 3**	**2**	**1**	**0.608**	**0.01**
P03923	*MTND6*	P_P	NADH-ubiquinone oxidoreductase chain 6	2	1	1.391	0.45
O95299	*NDUFA10*	P_P	NADH dehydrogenase [ubiquinone] 1 alpha subcomplex subunit 10, mitochondrial	56	17	0.957	0.82
Q86Y39	*NDUFA11*	P_P	NADH dehydrogenase [ubiquinone] 1 alpha subcomplex subunit 11	14	3	0.84	0.20
Q9P0J0	*NDUFA13*	P_P	NADH dehydrogenase [ubiquinone] 1 alpha subcomplex subunit 13	20	8	0.986	0.90
O95167	*NDUFA3*	P_P	NADH dehydrogenase [ubiquinone] 1 alpha subcomplex subunit 3	17	4	0.96	0.97
P51970	*NDUFA8*	P_P	NADH dehydrogenase [ubiquinone] 1 alpha subcomplex subunit 8	31	7	0.937	0.43
O95298	*NDUFC2*	P_P	NADH dehydrogenase [ubiquinone] 1 subunit C2	19	6	0.808	0.10
O43920	*NDUFS5*	P_P	NADH dehydrogenase [ubiquinone] iron-sulfur protein 5	29	7	0.935	0.22
P03905	*MTND4*	P_D	NADH-ubiquinone oxidoreductase chain 4	3	2	1.036	0.57
P03915	*MTND5*	P_D	NADH-ubiquinone oxidoreductase chain 5	11	3	0.977	1.00
O14561	***NDUFAB1***	**P_D**	**Acyl carrier protein, mitochondrial**	**6**	**2**	**0.727**	**0.46**
O75438	*NDUFB1*	P_D	NADH dehydrogenase [ubiquinone] 1 beta subcomplex subunit 1	3	2	0.995	0.98
O96000	*NDUFB10*	P_D	NADH dehydrogenase [ubiquinone] 1 beta subcomplex subunit 10	40	8	0.904	0.47
Q9NX14	*NDUFB11*	P_D	NADH dehydrogenase [ubiquinone] 1 beta subcomplex subunit 11, mitochondrial	20	3	0.863	0.10

O95178	***NDUFB2***	**P_D**	**NADH dehydrogenase [ubiquinone] 1 beta subcomplex subunit 2**	**6**	**1**	**0.62**	**0.12**
O43676	*NDUFB3***	P_D	NADH dehydrogenase [ubiquinone] 1 beta subcomplex subunit 3	11	3	0.864	0.05
O95168	***NDUFB4***	**P_D**	**NADH dehydrogenase [ubiquinone] 1 beta subcomplex subunit 4**	**30**	**4**	**0.762**	**0.22**
O43674	*NDUFB5*	P_D	NADH dehydrogenase [ubiquinone] 1 beta subcomplex subunit 5, mitochondrial	28	6	0.918	1.00
O95139	*NDUFB6*	P_D	NADH dehydrogenase [ubiquinone] 1 beta subcomplex subunit 6	18	7	1.081	0.99
P17568	*NDUFB7*	P_D	NADH dehydrogenase [ubiquinone] 1 beta subcomplex subunit 7	11	4	0.814	0.30
O95169	*NDUFB8*	P_D	NADH dehydrogenase [ubiquinone] 1 beta subcomplex subunit 8, mitochondrial	13	4	0.911	0.25
Q9Y6M9	*NDUFB9*	P_D	NADH dehydrogenase [ubiquinone] 1 beta subcomplex subunit 9	38	8	0.92	0.17
Complex I Assembly Factors							
Q9H845	*ACAD9*		Acyl-CoA dehydrogenase family member 9, mitochondrial	80	30	1.107	0.15
Q9GZY4	*COA1*		Cytochrome c oxidase assembly factor 1 homolog	6	4	1.119	0.78
Q9BQ95	*ECSIT*		Evolutionarily conserved signaling intermediate in Toll pathway, mitochondrial	12	9	0.918	0.47
Q96CU9	*FOXRED1*		FAD-dependent oxidoreductase domain-containing protein 1	13	6	0.96	0.97
Q9Y375	***NDUFAF1****		**Complex I intermediate-associated protein 30, mitochondrial**	**11**	**8**	**0.797**	**0.004**
Q8N183	*NDUFAF2*		NADH dehydrogenase [ubiquinone] 1 alpha subcomplex assembly factor 2	49	13	0.855	0.35
Q9BU61	*NDUFAF3*		NADH dehydrogenase [ubiquinone] 1 alpha subcomplex assembly factor 3	32	7	0.942	0.88
Q9P032	*NDUFAF4*		NADH dehydrogenase [ubiquinone] 1 alpha subcomplex assembly factor 4	30	10	0.952	0.30
Q5TEU4	*NDUFAF5*		Arginine-hydroxylase NDUFAF5, mitochondrial	1	1	0.98	0.73
Q330K2	*NDUFAF6*		NADH dehydrogenase (ubiquinone) complex I, assembly factor 6	1	1	0.998	0.86
Q7L592	*NDUFAF7*		Protein arginine methyltransferase NDUFAF7, mitochondrial	16	10	0.95	0.99
Q8TB37	*NUBPL*		Iron-sulfur protein NUBPL	7	5	0.952	1.00
Q9NPL8	*TIMMDC1*		Complex I assembly factor TIMMDC1, mitochondrial	23	8	1.118	0.02
Q8IUX1	*TMEM126B*		Complex I assembly factor TMEM126B, mitochondrial	1	1	0.984	0.96
Q9BUB7	*TMEM70*		Transmembrane protein 70, mitochondrial	5	3	1.063	0.84

* Peptide spectral matches
Bold Font Subunits or assembly factors with FC ≤ 0.80 (n=6)
** Significantly reduced subunits or assembly factors (n=2)

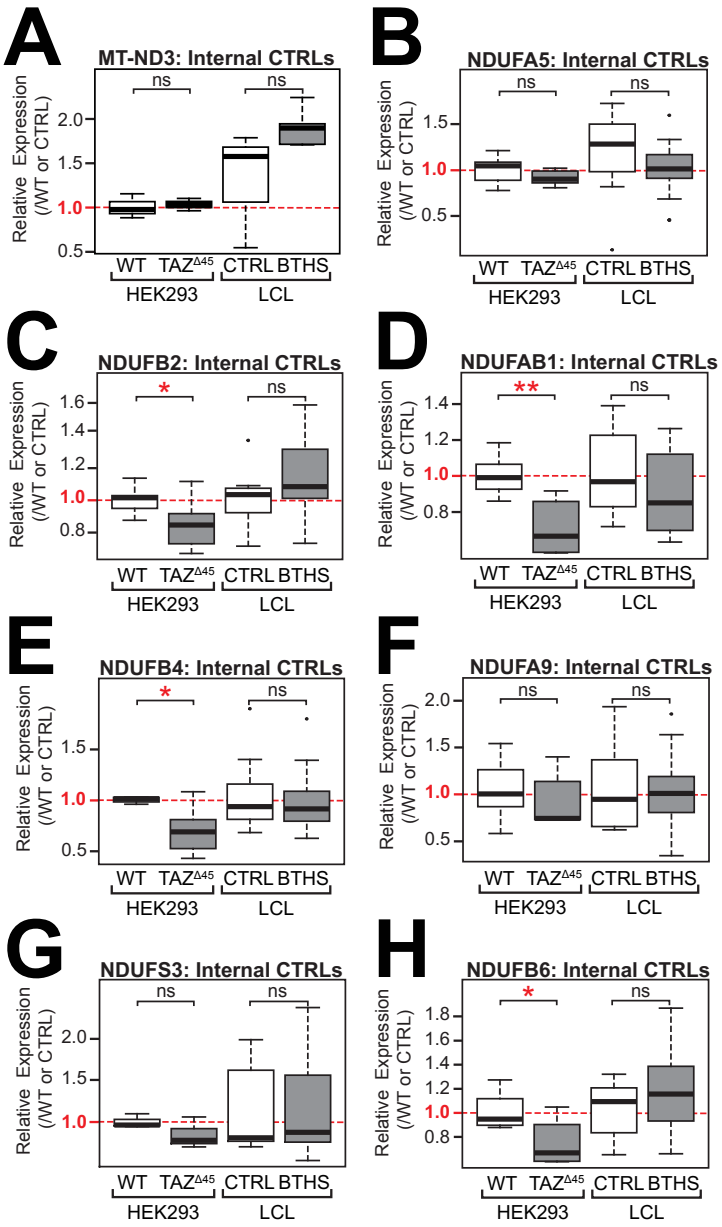

Figure S4. Relative mRNA expression of complex I (CI) subunits; (A) *MT-ND3* **(B)** *NDUFA5* **(C)** *NDUFB2* **(D)** *NDUFAB1* **(E)** *NDUFB4* **(F)** *NDUFA9* **(G)** *NDUFS3* **(H)** *NDUFB6* determined by qRT-PCR and $\Delta\Delta C_T$ quantification; WT n=6 (except *MT-ND3* and *NDUFS3*, n=3), *TAZ*$^{\Delta 45}$ n=6 (except *MT-ND3* and *NDUFS3*, n=3), CTRL n=10 (except *MT-ND3* n=5), BTHS n=15 (except *MT-ND3* n=3). Significant differences are indicated; * ≤ 0.05, ** ≤ 0.005, *** ≤ 0.0005, **** ≤ 0.00005.

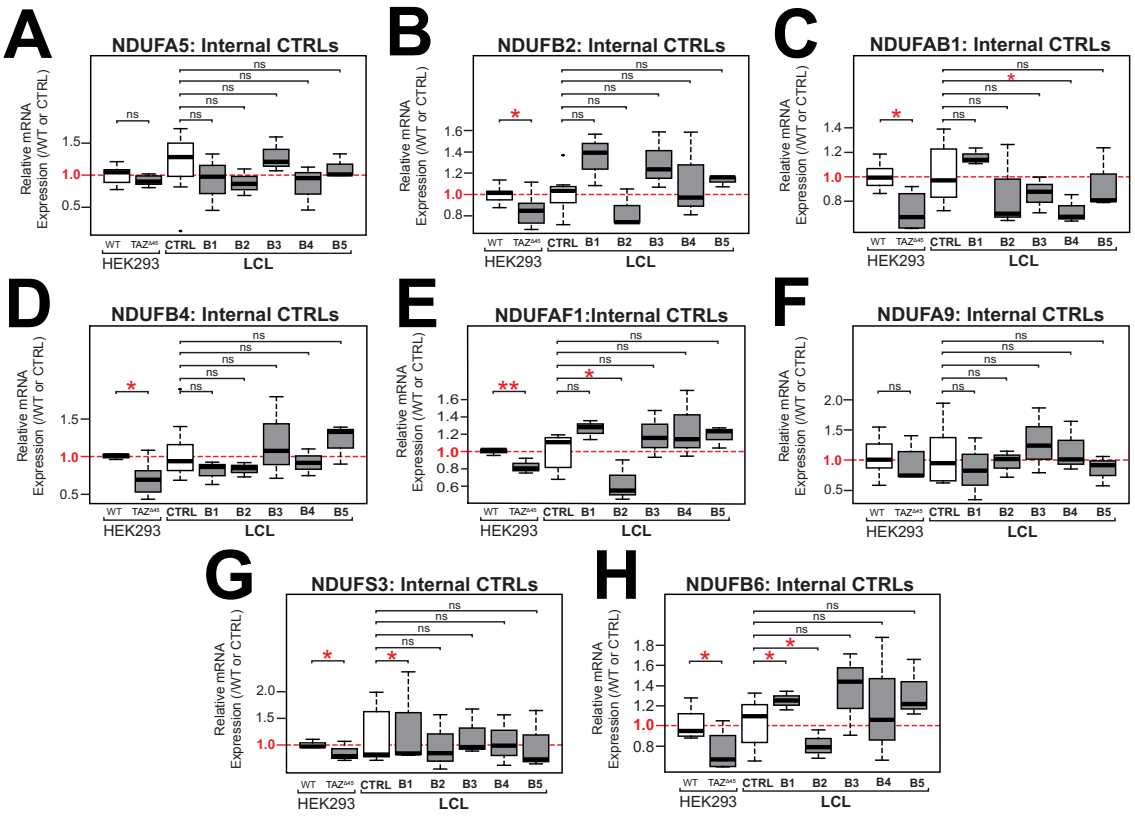

Figure S5. Relative mRNA expression of complex I (CI) subunits varies across different LCL lines. Relative mRNA expression of **(A)** *NDUFA5* **(B)** *NDUFB2* **(C)** *NDUFAB1* **(D)** *NDUFB4* **(E)** *NDUFAF1* **(F)** *NDUFA9* **(G)** *NDUFS3* **(H)** *NDUFB6* determined by qRT-PCR and $\Delta\Delta C_T$ quantification; WT n=6 (except *MT-ND3* and *NDUFS3*, n=3), *TAZ*$^{\Delta 45}$ n=6 (except *MT-ND3* and *NDUFS3*, n=3), CTRL n=10, B1 n=3, B2 n=3, B3 n=3, B4 n=3, B5 n=3. Significant differences are indicated; * ≤ 0.05, ** ≤ 0.005, *** ≤ 0.0005, **** ≤ 0.00005.

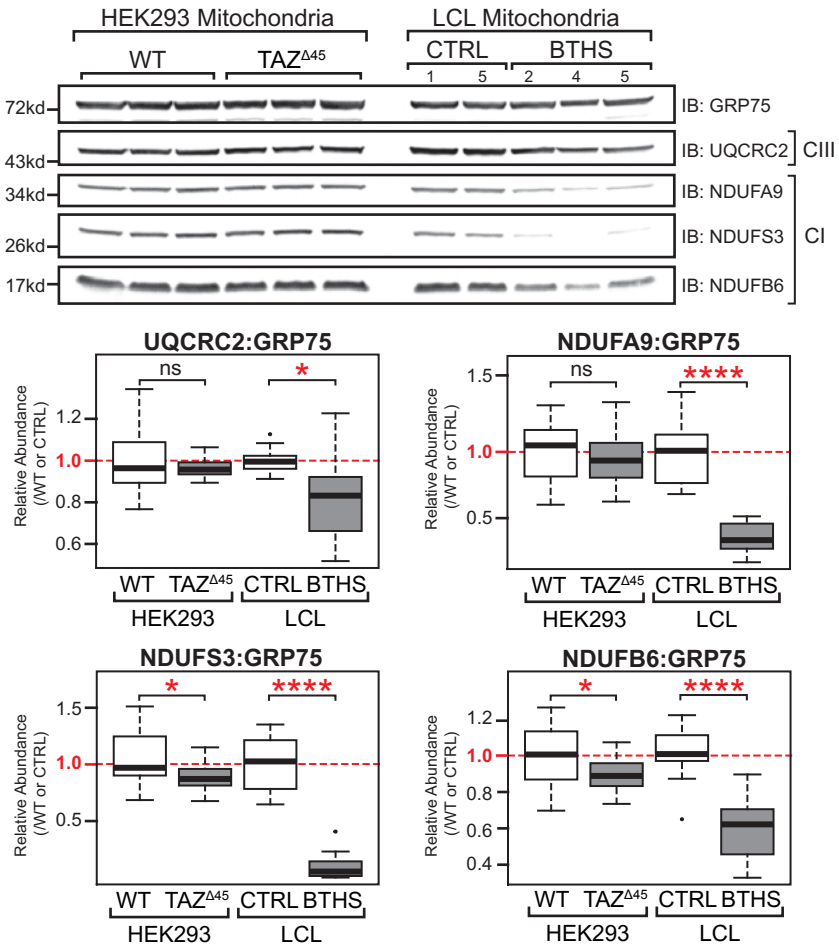

Figure S6. Immunoblotting of isolated mitochondria for CI and CIII subunits. Mitochondria (40 ug) isolated from the indicated lines were immunoblotted for the indicated proteins. Band intensities, relative to loading control GRP75, were quantified and plotted relative to WT/CTRL abundance; WT n=15, *TAZ*$^{\Delta 45}$ n=15, CTRL n=10, BTHS n=15. Significant differences are indicated; * ≤ 0.05, ** ≤ 0.005, *** ≤ 0.0005, **** ≤ 0.00005.

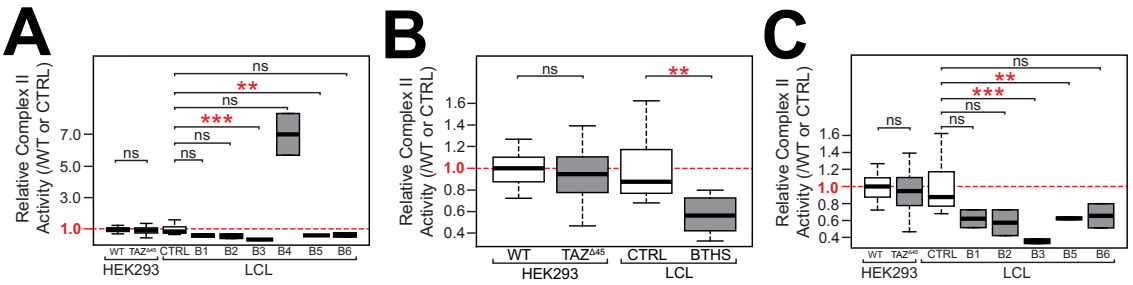

Figure S7. Difference in complex II (CII) activity between and within cell types. CII activity measured in HEK293 WT and *TAZ*$^{\Delta 45}$ or CTRL and BTHS LCLs mitochondria (200 ug total protein) on a microplate reader by following the production of ubiquinol by CII coupled to the reduction of the dye diclorophenolindophenol (DCPIP, 600nm). **(A)** Analysis of CII activity in LCLs showed that a single BTHS line, BTHS LCL #4, had significantly increased CII activity compared to the other BTHS lines; WT n=12, *TAZ*$^{\Delta 45}$ n=12, CTRL n=10, B1 n=2, B2 n=2, B3 n=2, B4 n=2, B5 n=2, B6 n=2. **(B)** Activity plotted without outlier BTHS LCL #4; WT n=12, *TAZ*$^{\Delta 45}$ n=12, CTRL n=10, BTHS n=10. **(C)** WT n=12, *TAZ*$^{\Delta 45}$ n=12, CTRL n=10, B1 n=2, B2 n=2, B3 n=2, B5 n=2, B6 n=2. Significant differences are indicated; * ≤ 0.05, ** ≤ 0.005, *** ≤ 0.0005, **** ≤ 0.00005.

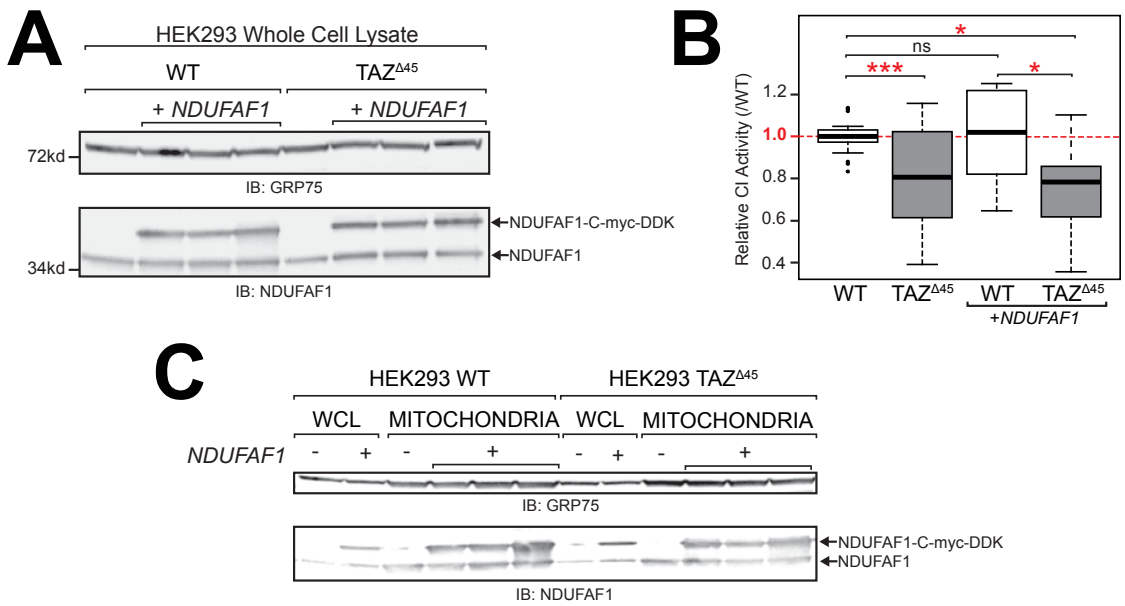

Figure S8. Overexpression of CI assembly factor NDUFAF1 does not normalize CI activity. (A) HEK293 WT and *TAZ*$^{\Delta 45}$ cells were transiently transfected with tagged *NDUFAF1* with Lipofectamine 3000 according to manufacturer's instructions. Whole cell extracts (45 ug) of the indicated lines and treatment concentrations were immunoblotted for the indicated proteins. **(B)** CI activity measured in mitochondria (200 ug total protein). Activity was measured on a microplate reader (450nm) by following the oxidation of NADH to oxidized nicotinamide adenine dinucleotide (NAD+). Activity plotted relative to WT abundance; WT n=25, *TAZ*$^{\Delta 45}$ n=26, WT-transfected n=9, *TAZ*$^{\Delta 45}$ n=8. (**C**) HEK293 WT and *TAZ*$^{\Delta 45}$ cells were transiently transfected with tagged *NDUFAF1* with Lipofectamine 3000 according to manufacturer's instructions. Whole cell extracts and isolated mitochondria (45 ug) of the indicated lines and treatment concentrations were immunoblotted for the indicated proteins. Significant differences are indicated; * ≤ 0.05, ** ≤ 0.005, *** ≤ 0.0005, **** ≤ 0.00005.

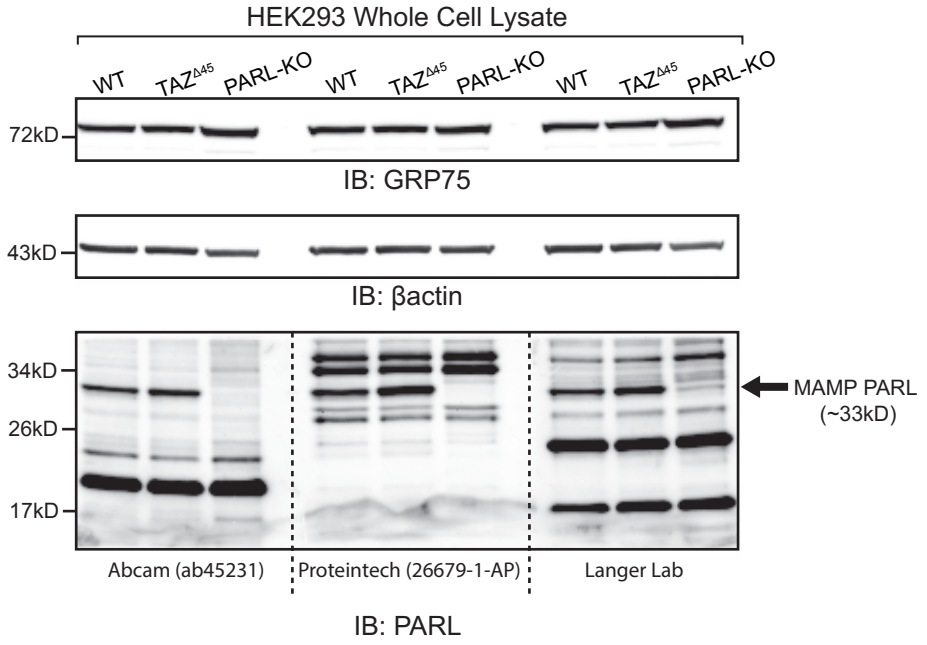

Figure S9. Validation and classification of PARL antibodies. Whole cell lysate (40 ug) of the indicated lines were immunoblotted for the indicated proteins. A single band at ~33kD is present in both WT and *TAZ*$^{\Delta 45}$ cells and absent in the PARL-KO cells, we classified this band as PARL.

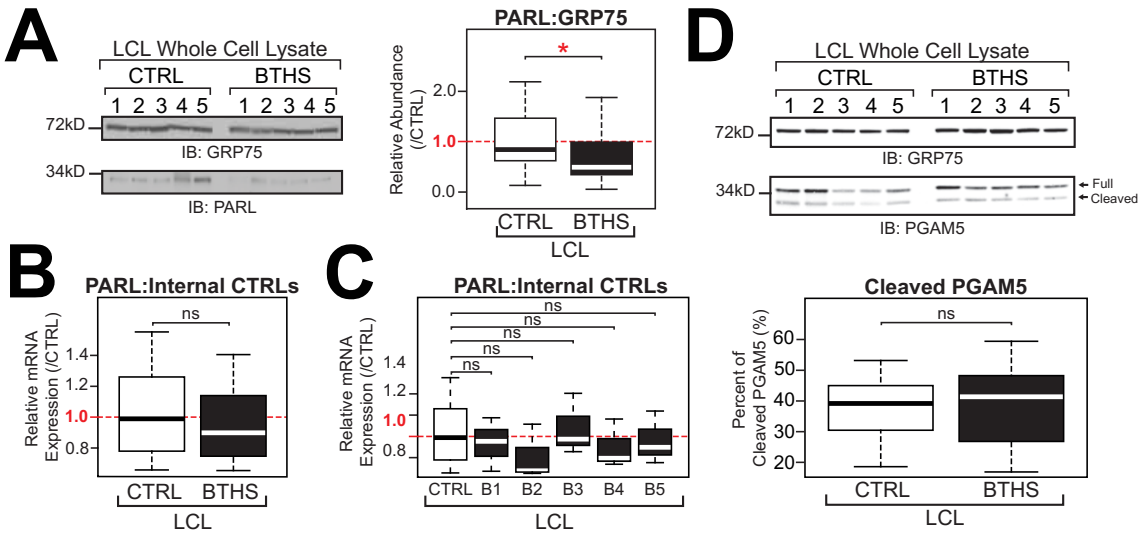

Figure S10. PARL abundance and activity in control and BTHS LCL lines. (A) Whole cell lysate (45 ug) of the indicated lines were immunoblotted for the indicated proteins. Band intensities, relative to loading control GRP75, were quantified and plotted relative to WT/CTRL abundance; CTRL n=26, BTHS n=35. **(B)** Relative mRNA expression of *PARL* determined by qRT-PCR and $\Delta\Delta C_T$ quantification; CTRL n=10, BTHS n=15. **(C)** Relative mRNA expression of *PARL* varies across different LCL lines; WT n=3, $TAZ^{\Delta 45}$ n=3, CTRL n=10, B1 n=3, B2 n=3, B3 n=3, B4 n=3, B5 n=3. **(D)** Whole cell lysate (45 ug) of the indicated lines were immunoblotted for the indicated proteins. Band intensities, relative to the loading control GRP75, for both full-length and cleaved PGAM5 were individually quantified and plotted as the percent of cleaved PGAM5 (cleaved/full+cleaved); CTRL n=20, BTHS n=18. Significant differences are indicated; * ≤ 0.05, ** ≤ 0.005, *** ≤ 0.0005, **** ≤ 0.00005.

Table S4. Abundance of PARL with CCCP treatment (20uM) at serial time points (Figure 3E).

Cell Line	Time Point	n#	Relative Abundance (/WT 0 mins)	WT vs. *TAZ*$^{\Delta 45}$ For each time point
WT	0 MIN	54	1.00	$p= 1.8 \times 10^{-10}$
TAZ$^{\Delta 45}$		48	1.51	
WT	10 MIN	5	1.13	$p= 1.3 \times 10^{-3}$
TAZ$^{\Delta 45}$		5	1.48	
WT	30 MIN	6	1.11	$p= 2.5 \times 10^{-3}$
TAZ$^{\Delta 45}$		5	1.44	
WT	60 MIN	6	1.14	$p= 6.4 \times 10^{-3}$
TAZ$^{\Delta 45}$		5	1.44	
WT	90 MIN	5	0.99	$p= 5.7 \times 10^{-5}$
TAZ$^{\Delta 45}$		5	1.38	
WT	120 MIN	6	1.14	ns
TAZ$^{\Delta 45}$		6	1.42	

Table S5. Percent of PGAM5 cleavage with CCCP treatment (20uM) at serial time points (Figure 3D).

Cell Line	Time Point	n#	Percent (%) Cleaved PGAM5	WT vs. *TAZ*$^{\Delta 45}$ For each time point	Difference (%) in Percent Cleaved
WT	0 MIN	41	12	$p= 1.5 \times 10^{-7}$	11
TAZ$^{\Delta 45}$		41	23		
WT	10 MIN	8	11	ns	9
TAZ$^{\Delta 45}$		8	20		
WT	30 MIN	8	18	p= 0.001	15
TAZ$^{\Delta 45}$		7	33		
WT	60 MIN	8	29	$p= 3.0 \times 10^{-5}$	16
TAZ$^{\Delta 45}$		5	45		
WT	90 MIN	5	39	$p= 2.4 \times 10^{-4}$	18
TAZ$^{\Delta 45}$		7	57		
WT	120 MIN	7	49	$p= 7.5 \times 10^{-5}$	18
TAZ$^{\Delta 45}$		7	67		

Table S6. Relative abundance of NDUFAF1 and relevant statistics of HEK293 WT and *TAZ*$^{\Delta 45}$ cells treated with BEL and SS-31 (Figure 4A)

Line & Treatment	n	Relative Abundance (/WT)	WT vs. *TAZ*$^{\Delta 45}$ For each treatment	*TAZ*$^{\Delta 45}$ vs. *TAZ*$^{\Delta 45}$-BEL	*TAZ*$^{\Delta 45}$ vs. *TAZ*$^{\Delta 45}$-SS-31
WT	27	1	$p= 4.9 \times 10^{-10}$	ns	$p= 2.8 \times 10^{-5}$
TAZ$^{\Delta 45}$	26	0.69			
WT-BEL	9	1	$p= 4.5 \times 10^{-3}$		
TAZ$^{\Delta 45}$-BEL	9	0.78			
WT-SS-31	9	1	ns		
TAZ$^{\Delta 45}$-SS-31	9	0.92			

Table S7. Relative mRNA expression and relevant statistics of HEK293 WT and *TAZ*$^{\Delta 45}$ cells treated with BEL and SS-31

Line & Treatment	n	Average Relative Expression to WT ($2^{-\Delta\Delta CT}$)	p-Value		
			WT vs. *TAZ*$^{\Delta 45}$ For each treatment	*TAZ*$^{\Delta 45}$ vs. *TAZ*$^{\Delta 45}$-BEL	*TAZ*$^{\Delta 45}$ vs. *TAZ*$^{\Delta 45}$-SS-31
NDUFB2 (Figure S11A)					
WT	6	1	p= 0.04	ns	ns
TAZ$^{\Delta 45}$	6	0.85			
WT-BEL	3	1	ns		
TAZ$^{\Delta 45}$-BEL	3	1.03			
WT-SS-31	3	1	ns		
TAZ$^{\Delta 45}$-SS-31	3	0.94			
NDUFAB1 (Figure S11B)					
WT	6	1	p=0.001	p= 0.02	ns
TAZ$^{\Delta 45}$	6	0.71			
WT-BEL	3	1	ns		
TAZ$^{\Delta 45}$-BEL	3	0.98			
WT-SS-31	3	1	p=0.01		
TAZ$^{\Delta 45}$-SS-31	3	0.88			
NDUFB4 (Figure S11C)					
WT	4	1	p= 0.02	ns	p= 0.03
TAZ$^{\Delta 45}$	6	0.71			
WT-BEL	3	1	ns		
TAZ$^{\Delta 45}$-BEL	3	0.97			
WT-SS-31	3	1	ns		
TAZ$^{\Delta 45}$-SS-31	3	1.09			
NDUFAF1 (Figure 4B)					
WT	6	1	p= 6.4 x 10^{-4}	p= 0.05	p= 0.01
TAZ$^{\Delta 45}$	6	0.80			
WT-BEL	3	1	ns		
TAZ$^{\Delta 45}$-BEL	3	0.94			
WT-SS-31	3	1	ns		
TAZ$^{\Delta 45}$-SS-31	3	0.97			
NDUFB6 (Figure S11D)					
WT	6	1	p= 0.01	p= 0.05	ns
TAZ$^{\Delta 45}$	6	0.75			
WT-BEL	3	1	ns		
TAZ$^{\Delta 45}$-BEL	3	1.04			
WT-SS-31	3	1	p= 0.001		
TAZ$^{\Delta 45}$-SS-31	3	0.82			

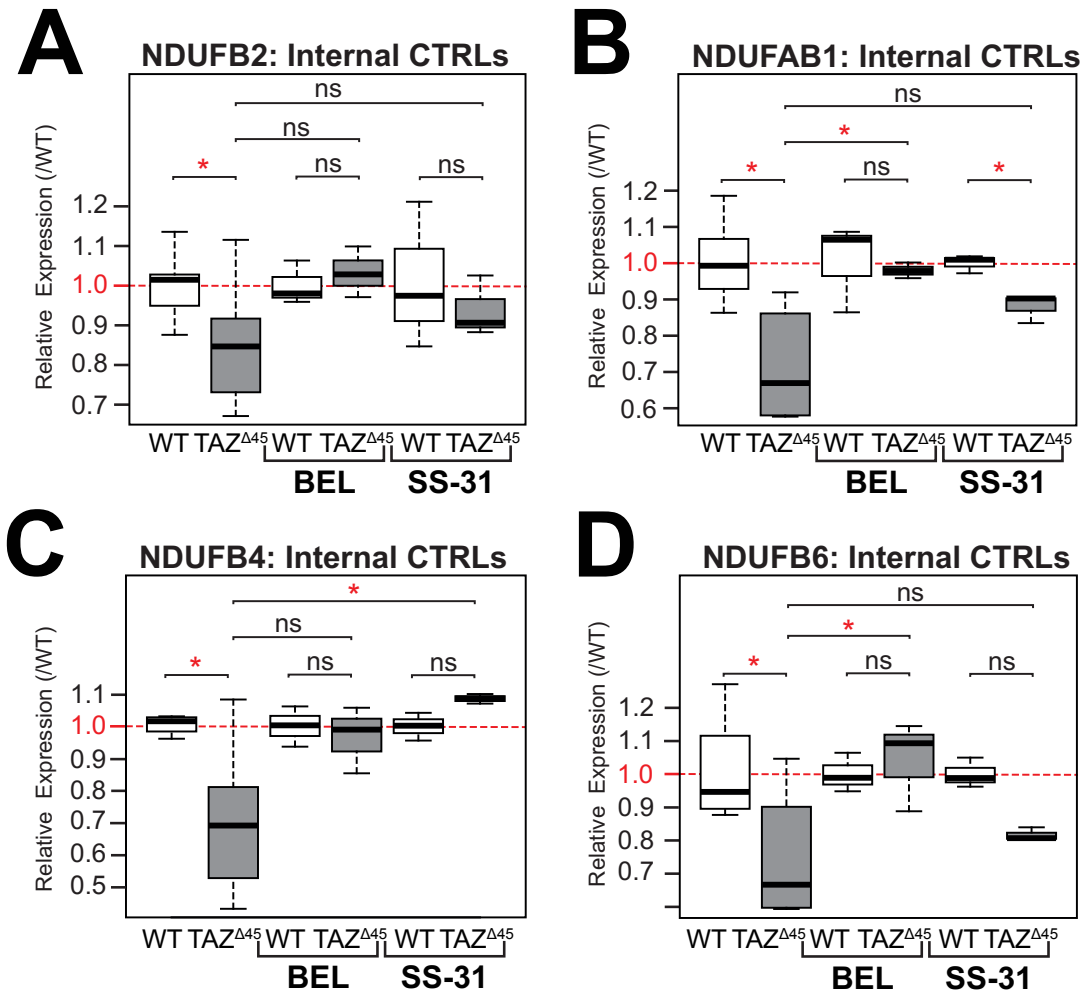

Figure S11. Relative mRNA expression of (A) *NDUFB2* (B) *NDUFAB1* (C) *NDUFB4* and (D) *NDUFB6* after treatment with BEL and SS-31. Expression determined by qRT-PCR and $\Delta\Delta C_T$ quantification using each respective control; WT n=6, *TAZ*$^{\Delta 45}$ n=3, WT-BEL n=3, *TAZ*$^{\Delta 45}$-BEL n=3, WT-SS-31 n=3, *TAZ*$^{\Delta 45}$-SS-31 n=3 per gene. Significant differences are indicated; * ≤ 0.05, ** ≤ 0.005, *** ≤ 0.0005, **** ≤ 0.00005.

Table S8. CI holoenzyme abundance and relevant statistics of HEK293 WT and *TAZ*$^{\Delta 45}$ cells treated with BEL and SS-31

Line & Treatment	n	Relative Abundance (/WT)	WT vs. *TAZ*$^{\Delta 45}$ For each treatment	*TAZ*$^{\Delta 45}$ vs. *TAZ*$^{\Delta 45}$-BEL	*TAZ*$^{\Delta 45}$ vs. *TAZ*$^{\Delta 45}$-SS-31
CI:CIV (Figure 4C)					
WT	11	1	p= 2.3 x 10^{-5}	ns	ns
TAZ$^{\Delta 45}$	11	0.59			
WT-BEL	8	1	p= 5.2 x 10^{-3}		
TAZ$^{\Delta 45}$-BEL	8	0.77			
WT-SS-31	3	1	ns		
TAZ$^{\Delta 45}$-SS-31	3	0.80			
CI:CII (Figure 4C)					
WT	10	1	p= 1.6 x 10^{-4}	p= 6.1 x 10^{-3}	ns
TAZ$^{\Delta 45}$	13	0.66			
WT-BEL	9	1	p= 0.02		
TAZ$^{\Delta 45}$-BEL	10	0.89			
WT-SS-31	4	1	ns		
TAZ$^{\Delta 45}$-SS-31	6	0.83			

Table S9. Percentage of cleaved PGAM5 and relevant statistics of HEK293 WT and *TAZ*$^{\Delta 45}$ cells treated with BEL and SS-31 (Figure 4D)

Line & Treatment	n	Percentage of Cleaved PGAM5 (%)	WT vs. *TAZ*$^{\Delta 45}$ For each treatment	*TAZ*$^{\Delta 45}$ vs. *TAZ*$^{\Delta 45}$-BEL	*TAZ*$^{\Delta 45}$ vs. *TAZ*$^{\Delta 45}$-SS-31
WT	41	12	$p= 1.5 \times 10^{-7}$	p= 0.01	$p= 2.6 \times 10^{-4}$
TAZ$^{\Delta 45}$	41	23			
WT-BEL	16	15	ns		
TAZ$^{\Delta 45}$-BEL	16	18			
WT-SS-31	9	18	ns		
TAZ$^{\Delta 45}$-SS-31	8	13			

Table S10. Relative abundance of cleaved PARL and relevant statistics of HEK293 WT and TAZ 45 cells treated with BEL and SS-31 (Figure 4E)

Line & Treatment	n	Relative Abundance of PARL (/WT)	WT vs. *TAZ*$^{\Delta 45}$ For each treatment	*TAZ*$^{\Delta 45}$ vs. *TAZ*$^{\Delta 45}$-BEL	*TAZ*$^{\Delta 45}$ vs. *TAZ*$^{\Delta 45}$-SS-31
WT	54	1.00	$p= 1.8 \times 10^{-10}$	$p= 7.1 \times 10^{-15}$	$p= 9.9 \times 10^{-5}$
TAZ$^{\Delta 45}$	48	1.51			
WT-BEL	11	0.96	ns		
TAZ$^{\Delta 45}$-BEL	10	0.93			
WT-SS-31	11	1.03	ns		
TAZ$^{\Delta 45}$-SS-31	12	1.11			

Table S11. Cell lines.

Line ID in Figures	Line ID	*TAZ* Genotype
C1	E1	WT *TAZ*
C2	CD09	WT *TAZ*
C3	MF17	WT *TAZ*
C4	CL114	WT *TAZ*
C5	CL156	WT *TAZ*
C6	C1-ND11043	WT *TAZ*
C7	C2-ND24284	WT *TAZ*
C8	C3-ND0438	WT *TAZ*
C9	C5-ND23427	WT *TAZ*
B1	JHUHV16_007	c.53_54delCC
B2	JHUHV16_018	c.207C>G
B3	JHUHV16_022	c.238G>A
B4	JHUHV15_033	c.82_84_delGTG
B5	JHUHV16_104	c.171delA
B6	JHUHV16_060	c.124delC

Table S12. Primers used for qRT-PCR.

Gene	Sequence (5' – 3')	
TBP	Forward	GAGCTGTGATGTGAAGTTTCC
	Reverse	TCTGGGTTTGATCATTCTGTAG
HPRT1	Forward	TGAGGATTTGGAAAGGGTGT
	Reverse	GAGCACACAGAGGGCTACAA
NDUFA9	Forward	CGCATGGGGTCACAGGTAAT
	Reverse	CTCGCGTCCCATTCCAGAAA
NDUFS3	Forward	TACACAGATGAGCTGACGCC
	Reverse	TCCAAACATGTCCCAGATCTCC
MT-ND3	Forward	ACTACCACAACTCAACGGCT
	Reverse	GCGGGGGATATAGGGTCGAA
NDUFB4	Forward	CATGGGAGCTCTGTGTGGAT
	Reverse	TTCTTTCCTATCCCTCTCAGTTTT
NDUFAB1	Forward	GCCGCCAGTATAGCGACAT
	Reverse	CCAAACTGTCTAAGCCCAGGT
NDUFA5	Forward	GCGGGTGTGCTGAAGAAGA
	Reverse	TTCCGCTTTAACCATAGCCAG
NDUFB2	Forward	GAACTCGCTCTGGAACACCT
	Reverse	ACTGCTGAAGATGGTGGAGT
NDUFB6	Forward	TCCATGGGGTATACAAAAAGAG
	Reverse	GGAAATTCTTTCATTGGTGGA
NDUFAF1	Forward	GGCAGGAGGTCAAGATTCCTT
	Reverse	AGCCAAGGTGAATCCTATAGAAGAG
PARL	Forward	CGCCATGGATACAGCAGGA
	Reverse	CACTAGCGGCTCCCTGTTCTT
MT-RNR1	Forward	TAGAGGAGCCTGTTCTGTAATCGAT
	Reverse	CGACCCTTAAGTTTCATAAGGGCTA
MT-CO1	Forward	GACGTAGACACACGAGCATATTTCA
	Reverse	AGGACATAGTGGAAGTGAGCTACAAC
MT-ATP6	Forward	TAGCCATACACAACACTAAAGGACGA
	Reverse	GGGCATTTTTAATCTTAGAGCGAAA

Chapter 4

Conclusions

Employing hypothesis-generating untargeted proteomics and metabolomics in cellular models of methylmalonic acidemia (MMA), propionic acidemia (PA), Barth syndrome (BTHS), we identified and functionally confirmed novel mechanisms of cellular pathogenicity.

Using patient and CRISPR/Cas9-edited cellular modeling of MMA and PA, we identified serine metabolism as a novel target of cellular pathogenesis in MMA and PA. Glucose labeled flux metabolomics found that both *MUT*-null and *PCCA*-null cells have increased *de novo* serine synthesis from extracellular glucose, suggesting that provision of glucose is particularly important for the *de novo* biosynthesis of serine in MMA and PA. We also found that *MUT*-null had an increased abundance of unlabeled serine compared to both WT and *PCCA*-null cells, indicating indicate either increased transport of serine from the periphery in the *MUT*-null cells, or increased serine biosynthesis from other intracellular sources. Abnormally low plasma serine has been reported in a number of individuals with various primary mitochondrial disorders and has also been reported in an individual with MMA after liver/kidney transplant. [1, 2] Therefore, correction of serine deficits is potentially highly clinically relevant, and our evidence suggests that serine supplementation could represent an avenue for therapy. However, serine supplementation may be more beneficial in treating MMA, where transport of extracellular serine (as

opposed to *de novo* synthesis) appears to be the dominant mechanism. As we continue this project, we aim to explore the therapeutic potential of manipulating serine metabolism in MMA and PA, by investigating the downstream fate of *de novo* and imported serine, alterations in serine synthesis and utilization during cellular and mitochondrial stress, and how the manipulation of serine-metabolite-pools and serine products affects overall mitochondrial stress.

Using patient and CRISPR/Cas9-edited cellular modeling of BTHS, we identified two areas of mitochondrial dysfunction for further study: mitochondrial respiratory complex I (CI), and the PARL-mediated mitochondrial stress response pathway. Mitochondrial respiratory chain dysfunction and supercomplex destabilization have been shown in several cellular models of BTHS, though a specific decrease of CI has only been described in a limited number of studies in patient-derived lymphoblasts. [3–5] We show, for the first time, decreased gene and protein expression of specific subunits of CI. Further, we show that expression of NDUFAF1, a CI assembly factor, is strikingly abnormal in the setting of TAZ-deficiency. We also demonstrated that CI gene expression abnormalities, including subunits and assembly factors, are partially rescued with cardiolipin modulation. In demonstrating that cardiolipin modulation can rescue CI defects, we propose that CI assembly, assembly factor expression (NDUFAF1) and subunit expression (MT-ND3, NDUFA5, NDUFAB1, NDUFB2, NDUFB4) are potential cellular markers for treatment effect in BTHS.

PARL, which has roles in the mitochondrial response to stress via regulation of apoptosis and mitophagy, and its cleavage of PGAM5, are of particular interest in BTHS, where enlarged mitochondria have been observed in BTHS patient and TAZ-deficient

mouse cardiac tissue, consistent with impaired mitophagy. [6–9] Similar to CI defects, we showed that targeting CL with BEL and SS-31 partially remediates abnormalities in PARL abundance and PGAM5 cleavage. The PARL proteolytic and signaling cascade has diverse downstream targets in addition to PGAM5, including PINK1, BCL-xL, FUNDC1 and others, with numerous effects on mitochondrial and cellular metabolism and survival, and thus represents a wide area for future study in TAZ-deficiency. [10, 11]

As respiratory chain assembly and subunit gene and protein expression are tightly linked, it is not possible at this time to know which is the primary vs. secondary in the setting of TAZ-deficiency (i.e., whether CL abnormalities affect one or all of these CI-associated abnormalities), and this warrants further investigation. [12] It is also not clear at this time if the abnormalities in PARL expression and CI expression/function are interdependent or are each independently initiated by inner mitochondrial membrane disturbances caused by CL abnormalities. One way to test this would be to correct the CI dysfunction in isolation and examine for remediation of PARL defects. Because overexpression of *NDUFAF1* in the TAZ-deficient cells was not sufficient to correct CI defects and test this hypothesis, other approaches such as downregulating PARL and assaying CI function/assembly could be considered.

Together, CI dysfunction and dysregulation of apoptosis/mitophagy via PARL represent attractive areas for study in the tissue-specific aspects of BTHS. Defective mitochondrial quality control, particularly as it affects stress responsiveness, is increasingly recognized for its role in several forms of cardiac dysfunction [13], and both primary and secondary CI defects are well documented in many forms of cardiac dysfunction. [14, 15] Furthermore, understanding the diverse and tissue-specific

mitochondrial effects caused by TAZ-deficiency have important implications for development of therapeutics. For example, CI targeting agents may not be sufficient to remediate cardiac or skeletal muscle abnormalities in BTHS, where an underlying defect in mitophagy and apoptosis are prominent TAZ-deficient associated abnormalities.

4.1 Future Directions

Whereas TAZ is ubiquitously expressed, the CL acyl chain composition is tissue specific; for example, brain CL is characterized by a diversified array of acyl chains including polyunsaturated chains, and in cardiac and skeletal muscle CL is predominantly characterized by the tetralinoleoyl form. [16, 17] We hypothesize that due to the tissue-specific nature of CL composition, dysfunctional TAZ has cell type-specific effects; i.e. neurons, with their diversified array of mature CL, are spared from severe bioenergetic and cellular effects of TAZ deficiency, whereas cardiomyocytes, with a narrow CL composition, will have severe cellular effects as a result of TAZ deficiency. In order to investigate the tissue-specific aspects of BTHS we developed a TAZ-deficient induced pluripotent stem cell (iPSC) line using CRISPR/Cas9 genome editing. We differentiated these cells into cell types clinically affected in BTHS (cardiomyocytes), and cell types clinically unaffected (neurons), and plan to evaluate and compare both CI dysfunction and dysregulation of apoptosis/mitophagy via PARL. We will further attempt to remediate these cellular defects by manipulating the CL composition of the different cell types, and evaluate for normalization or exacerbation of CI and PARL abnormalities.

We conclude that untargeted studies harnessing the power of -omics has the ability to uncover novel pathways of investigation in IEMs beyond primary biochemical defects, providing alternative targets for therapeutic interventions.

4.2 References

1. C. R. Ferreira, et al., Deoxysphingolipid precursors indicate abnormal sphingolipid metabolism in individuals with primary and secondary disturbances of serine availability. Mol. Genet. Metab. 124, 204–209 (2018).
2. H. J. Vernon, et al., A detailed analysis of methylmalonic acid kinetics during hemodialysis and after combined liver/kidney transplantation in a patient with mut(0) methylmalonic acidemia. J. Inherit. Metab. Dis. 37, 899–907 (2014).
3. I. A. Chatzispyrou, et al., Barth syndrome cells display widespread remodeling of mitochondrial complexes without affecting metabolic flux distribution. Biochim. Biophys. Acta - Mol. Basis Dis. 1864, 3650–3658 (2018).
4. F. Gonzalvez, et al., Barth syndrome: Cellular compensation of mitochondrial dysfunction and apoptosis inhibition due to changes in cardiolipin remodeling linked to tafazzin (TAZ) gene mutation. Biochim. Biophys. Acta - Mol. Basis Dis. 1832, 1194–1206 (2013).
5. M. McKenzie, M. Lazarou, D. R. Thorburn, M. T. Ryan, Mitochondrial Respiratory Chain Supercomplexes Are Destabilized in Barth Syndrome Patients. J. Mol. Biol. 361, 462–469 (2006).
6. S. L. N. Clarke, et al., Barth Syndrome. Orphanet J. Rare Dis. 8 (2013).
7. S. Lavandero, M. Chiong, B. A. Rothermel, J. A. Hill, Autophagy in cardiovascular biology. J. Clin. Invest. 125, 55–64 (2015).
8. E. Lee, et al., Autophagy is essential for cardiac morphogenesis during vertebrate development. Autophagy 10, 572–87 (2014).
9. A. Saric, K. Andreau, A. S. Armand, I. M. Møller, P. X. Petit, Barth syndrome: From mitochondrial dysfunctions associated with aberrant production of reactive oxygen species to pluripotent stem cell studies. Front. Genet. 6, 359 (2016).
10. K. Ma, et al., Dynamic PGAM5 multimers dephosphorylate BCL-xL or FUNDC1 to regulate mitochondrial and cellular fate. Cell Death Differ. 27, 1036–1051 (2020).
11. W. Wu, et al., FUNDC 1 regulates mitochondrial dynamics at the ER –mitochondrial contact site under hypoxic conditions. EMBO J. 35, 1368–1384 (2016).
12. J. X. Tang, K. Thompson, R. W. Taylor, M. Oláhová, Mitochondrial OXPHOS biogenesis: Co-regulation of protein synthesis, import, and assembly pathways. Int. J. Mol. Sci. 21 (2020).
13. G. W. Dorn, Mitochondrial dynamism and heart disease: changing shape and shaping change. EMBO Mol. Med. 7, 865–77 (2015).
14. R. J. Scheubel, et al., Dysfunction of mitochondrial respiratory chain complex I in human failing myocardium is not due to disturbed mitochondrial gene expression. J. Am. Coll. Cardiol. 40, 2174–2181 (2002).
15. E. Fassone, et al., Mutations in the mitochondrial complex I assembly factor NDUFAF1 cause fatal infantile hypertrophic cardiomyopathy. J. Med. Genet. 48, 691–697 (2011).
16. H. Cheng, et al., Shotgun lipidomics reveals the temporally dependent, highly diversified cardiolipin profile in the mammalian brain: Temporally coordinated postnatal diversification of cardiolipin molecular species with neuronal remodeling. Biochemistry 47, 5869–5880 (2008).
17. M. Schlame, M. Ren, Y. Xu, M. L. Greenberg, I. Haller, Molecular symmetry in mitochondrial cardiolipins. Chem. Phys. Lipids 138, 38–49 (2005).

Chapter 5

Curriculum Vitae

Arianna Franca Anzmann, PhD

Baltimore, MD 21205 • Phone: (410) 925-7515 • Email: afranca1@jhmi.edu

EXECUTIVE SUMMARY

- Molecular geneticist with extensive experience in the investigation, analysis and interpretation of genetic data and information.
- Doctorate education includes an in-depth understanding of next-generation sequencing techniques and the various tools and resources used in variant analysis.
- Excellent oral and written science communicator: awarded speaking and presentation prizes, as well as an NIH F31 Fellowship.
- Experience independently leading research projects and working collaboratively on cross functional teams.

EDUCATION

PhD in Human Genetics and Molecular Biology *2015 - 2021*
Johns Hopkins University School of Medicine, Department of Genetic Medicine, Baltimore, MD

MS in Biotechnology *2012 – 2015*
Johns Hopkins Zanvyl Krieger School of Arts & Sciences Baltimore, MD

BA in Biology *2008 – 2012*
Franklin and Marshall College, Lancaster, PA

RESEARCH EXPERIENCE

Graduate Researcher Mentor: Hilary Vernon, MD, PhD *2015 – Present*
Department of Genetic Medicine, Johns Hopkins University School of Medicine, Baltimore, MD

- Independently developed a novel HEK293 cellular model of TAZ deficiency using CRISPR/Cas9 genome editing technology to study Barth syndrome, a rare inborn error of mitochondrial phospholipid metabolism.
- Led a project that employed untargeted proteomics, shotgun lipidomics, gene expression analysis, and targeted metabolomics in our novel HEK293 model to identify novel areas of mitochondrial dysfunction in Barth syndrome.

- In a collaborative project, validated and tested two novel HEK293 cellular models to study methylmalonic acidemia (MMA) and propionic acidemia (PA).
- Supervised one undergraduate and three junior graduate students, including training them in molecular biology techniques as well as reviewing experimental data and directing future directions.
- Regularly summarize research progress for weekly internal lab presentations and yearly departmental presentations.
- Educate and tutor fellow graduate students as a Teacher Assistant in various graduate courses including, Principles of Genetics, Pathology for Graduate Students, and Concept of the Gene.

Laboratory Manager Mentor: Garry Cutting, MD *2012 – 2015*

Department of Genetic Medicine, Johns Hopkins University School of Medicine, Baltimore, MD

- In an independent project, analyzed promoter variants in *SLC26A9*, a modifier gene of cystic fibrosis related diabetes (CFRD), using various techniques such as cloning, mutagenesis, cell culture, and luciferase assays, to determine their effect on *SLC26A9* and CFRD.
- Established the CFTR2 Cell Center (C3), designed to systematically test CFTR variants for CFTR function and response to drugs, which included, the creation of a designated laboratory space and the implementation of standard laboratory protocols to ensure consistency and quality of results.
- Maintained and organized an inventory of lab supplies and reagents.

Undergraduate Researcher Mentor: Clara Moore, PhD *2010 – 2012*

Biology Department, Franklin and Marshall College, Lancaster, PA

- In an independent project, designed and performed proteomics-based experiments to identify genes with altered expression during heart development in the Ts65Dn mouse model for Down syndrome.

Summer Intern Mentor: Roger Reeves, PhD *2010*

Physiology Department, Johns Hopkins University School of Medicine, Baltimore, MD

- Established and analyzed a mouse pedigree with data from Franklin and Marshall and Johns Hopkins University School of Medicine to assess male fertility in the Ts65Dn mouse model for Down syndrome.

TEACHING EXPERIENCE

2018 Teaching Assistant, Principles of Genetics

2016 Teaching Assistant, Pathology for Graduate Students: Basic Mechanisms

2016 Teaching Assistant, Concept of the Gene

HONORS AND AWARDS

2020 The American Society of Human Genetics Annual Meeting Reviewer's Choice Abstract

2019 MD-GEM Wolfe Street Competition Research Grant. $10,000.

2019 The American Society of Human Genetics Annual Meeting Reviewer's Choice Abstract

2019 The American Society of Human Genetics, Charles J. Epstein Trainee Award for Excellence in Human Genetics Research, Semifinalist

2019 The United Mitochondrial Disease Foundation, Best Poster Lighting Round Presentation

2019 National Heart, Lung, and Blood Institute of the National Institutes of Health Fellowship Award (F31HL147454)

2019 The Society for Inherited Metabolic Disorders Founders Award, Best Oral Presentation by a Trainee

2018 The Society for Inherited Metabolic Disorders Travel Award. $1,000.

2018 The Barth Syndrome Foundation Travel Award. $326.

2012 Graduated from Franklin and Marshall College *cum laude*

2011 Biology Departmental Honors. "Proteomic Identification of Protein Misexpression During Cardiogenesis in the Ts65Dn Down Syndrome Mouse Model"

2011 Howard Hughes Medical Institute Summer Scholar. Proteomic identification of protein misexpression during cardiogenesis in the Ts65Dn Down syndrome mouse model. $3,750.

2011 Howard Hughes Medical Institute Summer Scholar Travel Grant, 2011 Mouse Genetics Conference, The Genetics Society of America. $1,162.28

PUBLICATIONS

Anzmann AF, Sniezek OL, Pado A, Busa V, Vaz FM, Kreimer SD, Cole RN, Le A, Kirsch BJ, Claypool SM, Vernon HJ **(2021**) Barth syndrome cellular models have dysregulated respiratory chain complex I and mitochondrial quality control due to abnormal cardiolipin. *bioRxiv* doi: https://doi.org/10.1101/2021.01.06.425502

Sniezek OL, **Anzmann AF**, Claypool SM, Vernon HJ **(2020)** Cardiolipin's Remodeling Rules Revealed: The Role of the Cellular Lipidome. *Cell Reports* 30(12):3949-3950.

Lam AN, Aksit MA, Vecchio-Pagan B, Shelton CA, Osorio DL, **Anzmann AF**, Goff LA, Whitcomb DC, Blackman SM, Cutting GR **(2019)** Increased expression of anion

transporter SLC26A9 delays diabetes onset in cystic fibrosis. *The Journal of Clinical Investigation* 130(1): 272-286.

Anzmann AF, Pinto S, Busa V, Carlson J, McRitchie S, Sumner S, Pandey A, Vernon HJ **(2019)** Multi-omics studies in cellular models of methylmalonic acidemia and propionic acidemia reveal dysregulation of serine metabolism. *Biochimica Biophysica Acta Molecular Basis of Disease* 1865(12):165538.

Anzmann AF, Claypool SM, Vernon H **(2019)** Mitochondrial dysfunction and Barth Syndrome. Handbook of *Mitochondrial Dysfunction*.

Sharma N, Evans TA, Pellicore MJ, Davis E, Aksit MA, McCague AF, Joynt AT, Lu Z, Han ST, **Anzmann AF**, Lam AN, Thaxton A, West N, Merlo C, Gottschalk LB, Raraigh KS, Sosnay PR, Cotton CU, Cutting GR. **(2018)** Capitalizing on the heterogeneous effects of CFTR nonsense and frameshift variants to inform therapeutic strategy for cystic fibrosis. *PLoS Genet* 14(11).

Vecchio-Pagán B, Blackman SM, Lee M, Atalar M, Pellicore MJ, Pace RG, **Franca AL**, Raraigh KS, Sharma N, Knowles MR, Cutting G.R. **(2016)** Deep resequencing of CFTR in 762 F508del homozygotes reveals clusters of non-coding variants associated with cystic fibrosis disease traits. *Human Genome Variation* 3:16038.

Lee M, Vecchio-Pagán B, Sharma N, Waheed A, Li X, Raraigh KS, Robbins S, Han ST, **Franca AL**, Pellicore MJ, Evans TA, Arcara KM, Nguyen H, Luan S, Belchis D, Hertecant J, Zabner J, Sly WS, Cutting GR **(2016)** Loss of carbonic anhydrase XII function in individuals with elevated sweat chloride concentration and pulmonary airway disease. *Human Molecular Genetics* 25(10): 1923-1933.

Gottschalk LB, Vecchio-Pagan B, Sharma N, Han ST, **Franca A**, Wohler ES, Batista DA, Goff LA, Cutting GR **(2015)** Creation and characterization of an airway epithelial cell line for stable expression of CFTR variants. *Journal of Cystic Fibrosis* 5(3):285-94.

Corvol H, Blackman SM, Boëlle PY, Gallins PJ, Pace RG, Stonebraker JR, Accurso FJ, Clement A, Collaco JM, Dang H, Dang AT, **Franca A**, Gong J, Guillot L, Keenan K, Li W, Lin F, Patrone MV, Raraigh KS, Sun L, Zhou YH, O'Neal WK, Sontag MK, Levy H, Durie PR, Rommens JM, Drumm ML, Wright FA, Strug LJ, Cutting GR, Knowles MR **(2015)** Genome-wide association meta-analysis identifies five modifier loci of lung disease severity in cystic fibrosis. *Nature Communications* 6:8382.

Sharma N, Sosnay PR, Ramalho AS, Douville C, **Franca A**, Gottschalk LB, Park J, Lee M, Vecchio-Pagan B, Raraigh KS, Amaral MD, Karchin R, Cutting GR **(2014)** Experimental assessment of splicing variants using expression minigenes and comparison with in silico predictions. *Human Mutation* 35(10):1249-1259.

Moore CS, Hawkins C, **Franca A**, Lawler A, Devenney B, Das I, Reeves RH **(2010)** Increased male reproductive success in Ts65Dn "Down syndrome" mice. *Mammalian Genome* 21:543-549.

NCBI Bibliography: https://www.ncbi.nlm.nih.gov/myncbi/arianna.anzmann.1/bibliography/public/

PRESENTATIONS

2020 **Anzmann AF**, Sniezek OL, Pado A, Busa V, Vaz FM, Kreimer SD, Cole RN, Le A, Kirsch BJ, Claypool SM, Vernon HJ. *Barth syndrome cellular models have dysregulated respiratory chain complex I and mitochondrial quality control due to abnormal cardiolipin*. American Society of Human Genetics Annual Meeting. **Virtual Poster Presentation.**

2019 **Anzmann AF,** Sniezek O, Claypool SM, Vernon HJ. *Multi-omics analysis of a new cellular model of Barth Syndrome uncovers mechanisms of mitochondrial dysfunction and highlights the importance of tissue-specific modeling.* American Society of Human Genetics Annual Meeting, Houston, TX. **Poster Presentation.**

2019 **Anzmann AF,** Claypool SM, Hilary HJ. *Multi-omics analysis of a new cellular model of Barth Syndrome uncovers mechanisms of mitochondrial dysfunction.* The United Mitochondrial Disease Foundation Symposium, Alexandria, VA. **Poster and Oral Presentation.**

2019 **Anzmann AF,** Busa V, Pinto S, McRitchie S, Sumner S, Pandey A, Vernon HJ. *Multi-omics studies in patient-derived and CRISPR-edited cellular models of methylmalonic acidemia and propionic acidemia reveal dysregulation of serine metabolism*. Society for Inherited Metabolic Disorders Annual Meeting, Seattle, WA. **Oral Presentation.**

2018 **Anzmann AF**, Claypool S, Vernon H. *Development of an iPSC derived cellular model of Barth Syndrome*. TEDCO Entrepreneur Expo & Stem Cell Symposium, College Park, MD. **Poster Presentation.**

2018 **Anzmann AF,** Cole R, Kirsch BJ, Le A, Vaz F, Claypool S, Vernon H. *Multi-omics analyses and functional studies in a new model of Barth Syndrome and in patient derived cells uncover novel mechanisms of pathogenesis and potential targets for therapeutic intervention.* American Society of Human Genetics Annual Meeting, San Diego, CA. **Poster Presentation**.

2018 **Anzmann AF,** Busa VF, Vernon HJ. *Understanding downstream cellular effects of TAZ deficiency in a novel CRISPR edited cellular model.* Barth Syndrome Foundation 9th International Scientific, Medical & Family Conference, Clearwater, FL. **Poster and Oral Presentation**.

2016 **Franca A** and Mathews DJ. (2016) *Review of Return of Results Policy, As Reflected in Clinical Trial Informed Consent Documents.* American Society of Human Genetics Annual Meeting, Vancouver, Canada. **Poster Presentation**.

2012 **Franca A**. *Proteomic identification of protein misexpression during cardiogenesis in the Ts65Dn Down syndrome mouse model.* Thesis Presentation for Departmental Honors, Franklin and Marshall College, Lancaster, PA. **Oral Presentation.**

2011 **Franca A.** *Proteomic identification of protein misexpression during cardiogenesis in the Ts65Dn Down syndrome mouse model.* Summer Seminar Series in Bioinformatics and Computational Biology, Franklin and Marshall College, Lancaster, PA. **Oral Presentation**.

2011 **Franca A**, Kelly EM, Moore CS. *Proteomic identification of protein misexpression during cardiogenesis in the Ts65Dn Down syndrome mouse model.* Mouse Genetics Conference, The Genetics Society of America, Washington D.C. **Poster Presentation.**